

# **Observations of Mercury's rotational state from combined MESSENGER laser altimeter and image data**

vorgelegt von

Alexander Stark, M.Sc.

geb. in Leninsk-Kusnezki (Russland)

Von der Fakultät VI - Planen Bauen Umwelt

der Technischen Universität Berlin

zur Erlangung des akademischen Grades

Doktor der Naturwissenschaften

- Dr. rer. nat. -

genehmigte Dissertation

Promotionsausschuss:

Vorsitzender: Prof. Dr. Dr. h.c. Harald Schuh

Gutachter: Prof. Dr. Jürgen Oberst

Gutachter: Prof. Dr. Steven A. Hauck, II

Gutachter: Prof. Dr. Nicolas Thomas

Tag der wissenschaftlichen Aussprache: 13.11.2015

Berlin 2015

D83



## PhD Thesis

# Observations of Mercury's rotational state from combined MESSENGER laser altimeter and image data



Supervised by:

Prof. Dr. phil. nat. Jürgen Oberst & Dr. rer. nat. Hauke Hussmann

Released by:

Alexander Stark, MSc.

## Acknowledgment

First of all I would like to thank Jürgen Oberst for the opportunity to write this thesis in his group at DLR. He spend much time listening to my problems and always helped me to find best solutions. Thank you for the possibility to make a stay at the Moscow State University for Geodesy and Cartography, which was a great experience and pushed my work forward. I want to thank you for your consistent support and for being such a great adviser. Special thanks to Hauke Hussmann, who always found time to discuss my results and who taught me a lot about planetary science. Furthermore, I want to thank Steve A. Hauck and Nicolas Thomas for reviewing my thesis as well as Harald Schuh for being the chair of the dissertation committee.

I had a great opportunity to work with colleagues from the MESSENGER science team. A big thank you to Sean C. Solomon and Jean-Luc Margot for discussing and proof-reading my results and to Gregory A. Neumann for his support with the MLA data.

I want to thank Frank Preusker for extensive discussions and advice in usage of stereo DTMs. I learned a lot from Klaus Gwinner, Bernd Giese and Frank Sohl. Gregor Steinbrügge, Andreas Pasewaldt, Stephan Elgner, Philipp Gläser and Sven Bauer a big thank you for fruitfull discussions. I also thank Thomas Roatsch and Marita Wählich for their support and Helena Ritter for proof-reading parts of the thesis.

I thank my parents Jakob and Tatjana Stark and my sister Olga Stark for their never-ending support. A huge thank you to my fiancée Katharina Busler for her endless love. She encouraged me and supported me in everything.

To Katharina

## Structure of the dissertation

This dissertation is structured as follows: First an introduction to Mercury and its observations is given. It provides an overview about the main characteristics of Mercury and describes in particular its unique rotational state. The introduction is followed by three scientific publications, which were published in peer-reviewed journals and included as postprints in this thesis. The three papers are:

### **Research Paper I**

A. Stark, J. Oberst, H. Hussmann.

#### **Mercury's resonant rotation from secular orbital elements.**

*Celestial Mechanics and Dynamical Astronomy*, 123(3), 263-277, 2015.

### **Research Paper II**

A. Stark, J. Oberst, F. Preusker, K. Gwinner, S. J. Peale, J.-L. Margot, R. J. Phillips, M. T. Zuber, S. C. Solomon.

#### **Mercury's rotational parameters from MESSENGER image and laser altimeter data: A feasibility study.**

*Planetary and Space Science*, 117, 64-72, 2015.

### **Research Paper III**

A. Stark, J. Oberst, F. Preusker, S. J. Peale, J.-L. Margot, R. J. Phillips, G. A. Neumann, D. E. Smith, M. T. Zuber, S. C. Solomon.

#### **First MESSENGER orbital observations of Mercury's librations.**

*Geophysical Research Letters*, 42, 7881-7889, 2015.

The results obtained in the papers are summarized in the Synthesis section. Finally, the dissertation includes a general discussion of all three papers and the scientific questions addressed by the thesis. This incorporates calculations of a simple interior-structure model for Mercury based on the obtained values for the rotational parameters. At the end an outlook for further investigations is given. The three papers are referenced in this thesis as Paper I-III hereinafter.

The author of this thesis, Alexander Stark, was the main contributor to the methods and results described in this thesis. The three papers were improved by comments of the reviewers and through discussions with the MESSENGER science team. The author received support from colleagues at German Aerospace Center (DLR) Berlin and the Technische Universität Berlin. The digital terrain models used in this study were processed from stereo images by Frank Preusker at DLR Berlin. The MESSENGER instrument teams contributed through processing of the raw MESSENGER data. The work presented in this dissertation was performed when the author was financed by DLR Berlin.



# Abstract

In this thesis observations of Mercury's rotational state were carried out, using orbital data from the MErcury Surface, Space ENvironment, GEochemistry, and Ranging (MESSENGER) spacecraft.

First, a reference rotation model of Mercury was derived. New Solar System ephemerides were used to obtain updated values for the mean orbital period and plane of Mercury as well as the instantaneous Laplace plane. With the help of the obtained values the resonant rotation model was constructed and used for interpretation of actual observations of the rotational state of the planet. For the measurement of the rotational parameters of Mercury a novel approach consisting of a combination of digital terrain models from stereo images and laser altimeter data from MESSENGER was elaborated. The method was extensively tested using simulated data and the uncertainty of the parameter estimation was assessed.

By applying this method to three years of MESSENGER orbital observations the rotational parameters, including the libration amplitude, the orientation of the rotation axis, and the mean rotation rate of Mercury, were measured. The libration amplitude was found to be  $38.9 \pm 1.3$  arc seconds or 460 m at the equator. The obliquity of the rotation axis was observed to be  $2.029 \pm 0.085$  arc minutes, which is very close to the orbital plane normal. The rotation period was measured as 58.6460768 days with an accuracy on the level of one second. This is lower than the resonant rotation value by 9.2 seconds, which is interpreted as the expression of a long-term librational motion.

The measured rotational parameters define Mercury's body-fixed frame and are critical for the coordinate system of the planet as well as the planning of future spacecraft missions. Additionally, the new rotational parameters combined with the gravity field information allow to draw conclusions about Mercury's interior structure. The existence of Mercury's large molten outer core could be confirmed and further constraints on the depth of the core-mantle boundary as well as the densities of mantle and core were derived.

## Zusammenfassung

Im Rahmen dieser Doktorarbeit wurde der Rotationszustand des Planeten Merkur mit Hilfe der Daten der Raumsonde MESSENGER (MErcury Surface, Space ENvironment, GEochemistry, and Ranging) bestimmt.

Zunächst wurde ein Referenzmodell für Merkurs Rotation ermittelt. Neue Ephemeriden des Sonnensystems wurden verwendet um aktuelle Werte für die mittlere Orbitdauer und -ebene, sowie die instantane Laplace-Ebene von Merkur zu berechnen. Mit Hilfe der erhaltenen Werte wurde das resonante Rotationsmodell konstruiert, welches für die Interpretation des wahren Rotationszustandes des Planeten verwendet wurde. Für die Bestimmung der Rotationsparameter wurde eine neue Methode entwickelt, die aus einer Kombination von digitalen Geländemodellen aus Stereobildern und Laseraltimeterprofilen besteht. Die Methode wurde unter Verwendung von simulierten Daten intensiv getestet und die Unsicherheiten der Parameterbestimmung ermittelt.

Unter der Anwendung der entwickelten Methode auf drei Jahre von orbitalen Beobachtungen durch MESSENGER wurden Merkurs Rotationsparameter bestimmt. Dazu gehören die Librationsamplitude, die Orientierung der Rotationsachse und die mittlere Drehrate. Die Librationsamplitude wurde zu  $38.9 \pm 1.3$  Bogensekunden oder 460 m am Äquator bestimmt. Die Neigung der Rotationsachse weicht mit  $2.029 \pm 0.085$  Bogenminuten nur geringfügig von der Orbitnormalen ab. Die Rotationsperiode wurde mit einer Genauigkeit von etwa einer Sekunde zu 58.6460768 Tagen gemessen. Dies ist um 9.2 Sekunden geringer als die resonante Rotation, was als Auswirkung einer langperiodischen Libration interpretiert wurde.

Die Bestimmung von Rotationsparametern erlaubt die Definition des mitrotierenden Bezugssystems und ist von grundlegender Bedeutung für Merkurs Koordinatensystem sowie die Planung von zukünftigen Raummissionen zu dem Planeten. Zusätzlich erlauben die ermittelten Rotationsparameter, unter Berücksichtigung der Eigenschaften des Gravitationsfeldes, Rückschlüsse über den inneren Aufbau Merkurs. Die Existenz eines großen geschmolzenen äußeren Kerns konnte bestätigt werden und weitere Randbedingungen für die Lage der Kern-Mantel-Grenze sowie die Dichten von Kern und Mantel gesetzt werden.

# Contents

<b>1</b>	<b>Motivation</b>	<b>1</b>
<b>2</b>	<b>Introduction</b>	<b>2</b>
2.1	Mercury – The planet . . . . .	2
2.2	Mercury rotation and dynamics . . . . .	4
2.2.1	Longitudinal libration . . . . .	6
2.2.2	Orientation of the rotation axis . . . . .	8
2.3	The MESSENGER mission . . . . .	8
2.3.1	The Mercury Laser Altimeter (MLA) . . . . .	10
2.3.2	The Mercury Dual Imaging System (MDIS) . . . . .	10
2.4	Mercury’s rotation from MESSENGER data . . . . .	14
2.5	References . . . . .	14
<b>3</b>	<b>Research Paper I – Mercury’s resonant rotation</b>	<b>18</b>
3.1	Introduction . . . . .	19
3.2	Secular orbital elements of Mercury . . . . .	19
3.2.1	Mean orbital period . . . . .	22
3.2.2	Mean orbital plane . . . . .	23
3.2.3	Laplace plane . . . . .	23
3.3	Mercury’s rotation . . . . .	26
3.3.1	Rotation model . . . . .	26
3.3.2	Resonant rotation . . . . .	27
3.3.3	Physical libration in longitude . . . . .	28
3.3.4	Cassini state . . . . .	29
3.4	Discussion and conclusion . . . . .	30
3.5	Appendix . . . . .	30
3.6	References . . . . .	35
<b>4</b>	<b>Research Paper II – Co-registration method</b>	<b>37</b>
4.1	Introduction . . . . .	38
4.2	MESSENGER data . . . . .	39
4.2.1	Laser altimeter . . . . .	39
4.2.2	Stereo photogrammetry . . . . .	41
4.3	Rotational model of Mercury . . . . .	42
4.4	Simulation of topographic observations . . . . .	43
4.4.1	Errors in spacecraft position and attitude . . . . .	44
4.4.2	High-resolution topography . . . . .	45
4.4.3	Stereo model . . . . .	45

4.5	Determination of rotational parameters . . . . .	47
4.6	Data weighting and error estimation . . . . .	49
4.7	Results . . . . .	50
4.8	Discussion and conclusion . . . . .	54
4.9	References . . . . .	55
<b>5</b>	<b>Research Paper III – Measurement of Mercury’s rotation</b>	<b>58</b>
5.1	Introduction . . . . .	59
5.2	Data Preparation . . . . .	61
5.3	Method . . . . .	62
5.4	Results . . . . .	65
5.5	Implications and Discussion . . . . .	68
5.6	Conclusion . . . . .	71
5.7	Supplementary Material . . . . .	71
5.8	References . . . . .	76
<b>6</b>	<b>Discussion and Outlook</b>	<b>78</b>
6.1	Resonant rotation model of Mercury . . . . .	78
6.2	Method for measurement of rotational parameters . . . . .	79
6.3	Rotational parameters of Mercury . . . . .	80
6.4	Implications on Mercury’s interior . . . . .	81
6.5	Implications for cartography and base maps . . . . .	83
6.6	Future exploration of Mercury: BepiColombo mission . . . . .	84
6.7	References . . . . .	84
<b>7</b>	<b>Synthesis</b>	<b>86</b>
<b>8</b>	<b>Appendix</b>	<b>87</b>
8.1	Mercury’s libration model . . . . .	87
8.2	Prime meridian constant of Mercury . . . . .	88
8.3	References . . . . .	91

## List of Figures

1	Mosaic of images from Mercury obtained by MESSENGER . . . . .	3
2	Rotation and orbit of Mercury . . . . .	5
3	Libration angle and rate of Mercury . . . . .	7
4	Scheme of the MESSENGER spacecraft . . . . .	9
5	Laser profiles obtained by MLA . . . . .	11
6	Monochrome and color mosaics of Mercury from MDIS images . .	12
7	Visualization of Mercury's orbital plane within the ICRF . . . . .	20
8	Orientation of the orbit and Laplace plane normal . . . . .	25
9	Scheme of the simulation and co-registration steps . . . . .	40
10	MLA profiles and stereo DTM used in the feasibility study . . . . .	42
11	Power spectrum of height residuals and simulated laser profile . .	46
12	Histogram and map of height residuals . . . . .	52
13	t-statistic of rotational parameters as a function of observation time	53
14	Data used for the measurement of rotational parameters . . . . .	60
15	Orientation of the rotation axis . . . . .	66
16	Mercury's polar moment of inertia . . . . .	70
17	Spin-rate difference cause by long-period librations . . . . .	72
18	Deviation of the rotation rate from the resonant rotation value . . .	74
19	Spherical two-layer model of Mercury . . . . .	82
20	Measured longitude and latitude of the Hun Kal crater . . . . .	89
21	MDIS image of the crater Hun Kal . . . . .	90

## List of Tables

1	Secular Keplerian orbital elements of Mercury from DE432 . . . . .	22
2	Secular Keplerian orbital elements of Mercury from INPOP13c . . .	31
3	Ten leading terms of the Fourier decomposition of orbital elements	33
4	Simulated and estimated values for rotational parameters . . . . .	51
5	Rotational and interior structure parameters of Mercury . . . . .	65
6	MDIS images used for measurement of the prime meridian value .	90

# 1 Motivation

The planet Mercury is the first planet of the Solar System. Although it is known since ancient times it is the least explored among the telluric planets. The study of the physical properties and evolution of rocky planets neighboring Earth is fundamental to answer the question about the formation of planets around stars and the availability of habitable environments. Important clues can be obtained through determination of the interior structure of the planet and its present state of matter. Mercury, with its unique spin-orbit resonance, allows the inference of such information through measuring its geodetic parameters by an orbiting spacecraft. This measurement procedure is known as the Peale experiment and was devised almost a half-century ago by Stanton J. Peale. The experiment consists of the measurement of the gravity field asymmetry and the rotation state of Mercury. The motivation of this thesis is therefore to provide information on the rotational state of Mercury by measuring its obliquity and libration amplitude. From these measurements it can be inferred whether the mantle is decoupled from the deep interior. The liquid state of the outer core can be confirmed and estimates for the core size can be gained. Both are important constraints for thermal models of Mercury.

For correct interpretation of the rotational state of Mercury prerequisites for measurements have to be defined. Description of Mercury's expected rotation in the 3:2 resonance has been re-assessed in Paper I of this thesis. The dynamical environment and the resulting rotational state are described in that paper and have been improved compared to previous models. The method for the measurement of rotational parameters is described in Paper II. It involves the analysis of digital terrain models from stereo images (stereo DTMs) and laser altimeter data. It is shown how the libration amplitude and other rotational parameters can be obtained from orbital observations by spacecraft. Co-registration of stereo DTMs with laser altimeter profiles enabled the measurement of parameters of the rotation model, as described in Paper III. Thereby the topography derived from stereo images served as reference for the laser altimeter profiles, which were acquired at various observation times. Through co-registration of these complementary data sets one obtains topographic information, referenced to the center of mass, and a rotation model of the planet. A discussion and implications of the three papers are given at the end of the thesis. The rotational state is also of great importance for referencing spacecraft observations to body-fixed coordinates. This includes not only image acquisition and laser altimeter measurements but also magnetic field, gravity, and spectroscopic observations.

## 2 Introduction

### 2.1 Mercury – The planet

Mercury is smallest and closest planet to the Sun. The planet moves on an elliptical orbit about the Sun with an average speed of 47 km/s. The pericenter distance is 46 million km, the largest distance is reached at apocenter being 70 million km, and the average distance is 56.7 million km. Due to the proximity to the Sun the orbit of Mercury is sensitive to effects related to general relativity, as the anomalous advance of the longitude of pericenter ([Einstein, 1915](#)). One orbital revolution lasts about 88 days and the rotation period is approximately 59 days ([Colombo, 1965](#)). Due to the strong tidal torque of the Sun the rotation of Mercury is coupled to the orbital motion in a 3:2 spin-orbit resonance. This means that it rotates three times around its axis, while it revolves twice about the Sun. Further, the strong tidal force of the Sun leads to solid body tides with expected amplitude of around 1 m ([Van Hoolst and Jacobs, 2003](#); [Padovan et al., 2014](#)).

The planet is relatively small, only little larger than Earth’s moon, and smaller than the Jovian moon Ganymede. Mercury’s mean radius is  $2439.36 \pm 0.02$  km ([Perry et al., 2015](#)) and its global shape is best represented by an ellipsoid ([Elgner et al., 2014](#)). Although the planet is quite small its mass is about  $3.301 \times 10^{23}$  kg ([Mazarico et al., 2014](#)), i.e. 4.5 times more than the mass of Earth’s moon. The ratio of mass and volume is the bulk density of the planet, which is with  $5425.2 \pm 6.7$  kg/m<sup>3</sup> the highest among the planets in our Solar System. The high uncompressed density of Mercury can be explained by a large fraction of iron in the chemical composition of the planet. Gravity field ([Anderson et al., 1987](#); [Mazarico et al., 2014](#)) and rotation state ([Margot et al., 2007, 2012](#), Paper III) measurements revealed that Mercury has a large iron core of about 2000 km radius ([Hauck et al., 2013](#); [Rivoldini and Van Hoolst, 2013](#)). This core is dominated by iron, but thermal evolution models ([Grott et al., 2011](#); [Peplowski et al., 2011](#); [Michel et al., 2013](#); [Tosi et al., 2013](#)) suggest that alloys of sulfur are necessary to prevent solidification of Mercury’s core until present days.

Mercury has a dipole magnetic field with a pronounced north-south asymmetry ([Anderson et al., 2011](#)), which is generated by the fluid iron core. This magnetic dipole field operated early in Mercury’s history as was shown by remanent magnetization in the crust of Mercury ([Johnson et al., 2015](#)). Unlike to its interior, the surface of Mercury is almost completely free of iron ([Nittler et al., 2011](#)). The planet has no atmosphere, but a tenuous exosphere constituted by hydrogen, helium, and varying concentrations of sodium, oxygen, and potassium ([McClintock et al., 2009](#)). The surface temperature can reach up to 700 K and is dropping to about 100 K within the day-night cycle. Due to its rotation locked to the orbital motion some regions on Mercury receive significantly more solar insolation



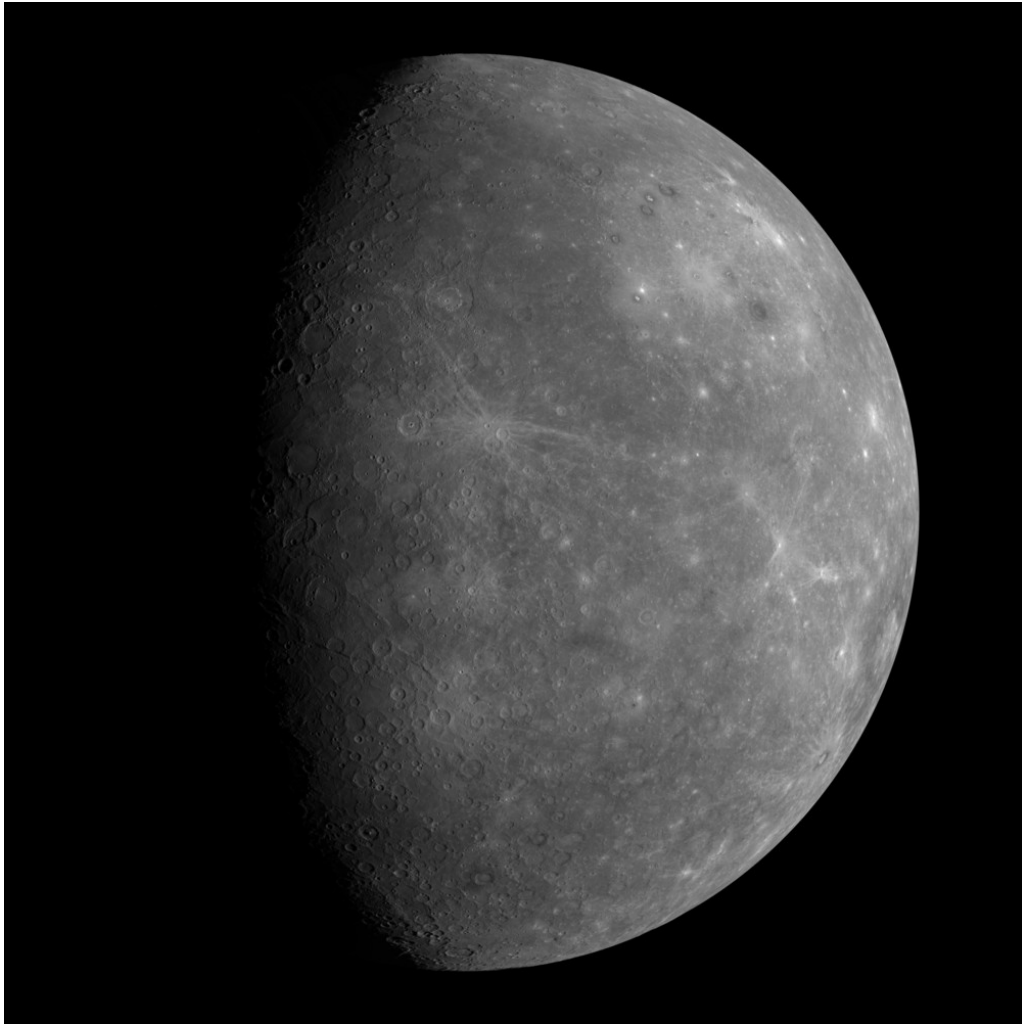


Figure 1: Mosaic of images from Mercury obtained by MESSENGER at its first flyby in 2008 (Image Credit: *NASA/Johns Hopkins University Applied Physics Laboratory/Carnegie Institution of Washington*).

than others and form "hot poles" located at  $0^\circ$  and  $180^\circ$  longitude. The surface of Mercury is heavily cratered and shows evidence of recent volcanism ([Head et al., 2011](#)). Lobate scarps and wrinkle ridges suggest a contraction of Mercury's radius by as much as 7 km ([Byrne et al., 2014](#)). The Caloris basin ([Oberst et al., 2010](#); [Zuber et al., 2012](#); [Ernst et al., 2015](#)) has a diameter of approx. 1550 km and is the largest basin on Mercury ([Fassett et al., 2012](#)). The northern regions are dominated by smooth, volcanic, contiguous plains ([Head et al., 2011](#); [Kreslavsky et al., 2014](#)). Near the north pole craters with permanent shadow contain a huge amount of water ice ([Neumann et al., 2013](#); [Paige et al., 2013](#)). Other small scale features known on Mercury are shallow, rimless depressions, so called "hollows". They are found within impact craters and are believed to be formed by loss of volatiles, triggered by space weathering and other processes ([Blewett et al., 2011](#); [Thomas et al., 2014](#)).

Earth-based observations of Mercury are complicated because of its vicinity to the Sun. Consequently, optical observations of Mercury are limited to dusk or dawn and make reliable detection of surface features challenging. New developments in optics and image processing, however, show promising results of reliable Earth-based optical observations ([Cremonese et al., 2010](#); [Ksanfomality, 2011](#)). Radar observations ([Harmon et al., 1994](#)) are more easily to perform and have accomplished since the 1960s. Radar bright features were found at the North and South poles and the rotation of Mercury was precisely measured ([Margot et al., 2007, 2012](#)) by a radar-speckle correlation technique ([Kholin, 1988](#)).

Until present days Mercury was explored by two spacecraft. The Mariner 10 spacecraft performed three flybys about Mercury in 1974 and 1975. At that time approximately 50% of the surface was imaged and a dipole magnetic field was observed ([Anderson et al., 1987](#)). In 2011 the MESSENGER spacecraft ([Solomon et al., 2001](#)) was the first to get in orbit about Mercury and performed more than four years of orbital observations. Further investigations of Mercury are planned to be carried out by the two-spacecraft mission BepiColombo arriving at Mercury in 2024 ([Benkhoff et al., 2010](#)).

## 2.2 Mercury rotation and dynamics

Due to the lack of reliable Earth-based observations the rotation of Mercury was for a long time assumed to be locked in a 1:1 spin-orbit resonance ([Schiaparelli, 1890](#)) likewise to Earth’s moon. Radar measurements by [Pettengill and Dyce \(1965\)](#) demonstrated that Mercury is trapped in 3:2 resonance ([Colombo, 1965](#); [Peale and Gold, 1965](#)), which is unique in our Solar System. The origin of this specific resonance is still under study ([Goldreich and Peale, 1966](#); [Wieczorek et al., 2012](#); [Noyelles et al., 2014](#)), but is strongly connected to the evolution of Mercury and its orbit. Figure 2 illustrates the rotation of Mercury along its orbit about the Sun.

Shortly after the discovery of the 3:2 spin-orbit resonance it was suggested that Mercury performs physical longitudinal librations on its orbital period ([Peale, 1972](#)). Through measurements of the libration amplitude, as well as the obliquity of the rotation axis and the low degree gravity field of Mercury, one can determine whether Mercury has a molten outer core and place constraints on its size and the densities of the core and mantle. This procedure is known as Peale’s experiment, named after Stanton J. Peale, who were the first to propose and discuss the feasibility such kind of measurements ([Peale, 1972, 1976, 1981](#)). The crucial advantage of Peale’s experiment compared to, e.g. seismic sounding, is that all measurements can be performed from an orbiting spacecraft. Until present days Peale’s experiment was performed twice: First, using gravity field information from Mariner 10 and Earth-based radar measurements ([Margot et al., 2007](#)), and a

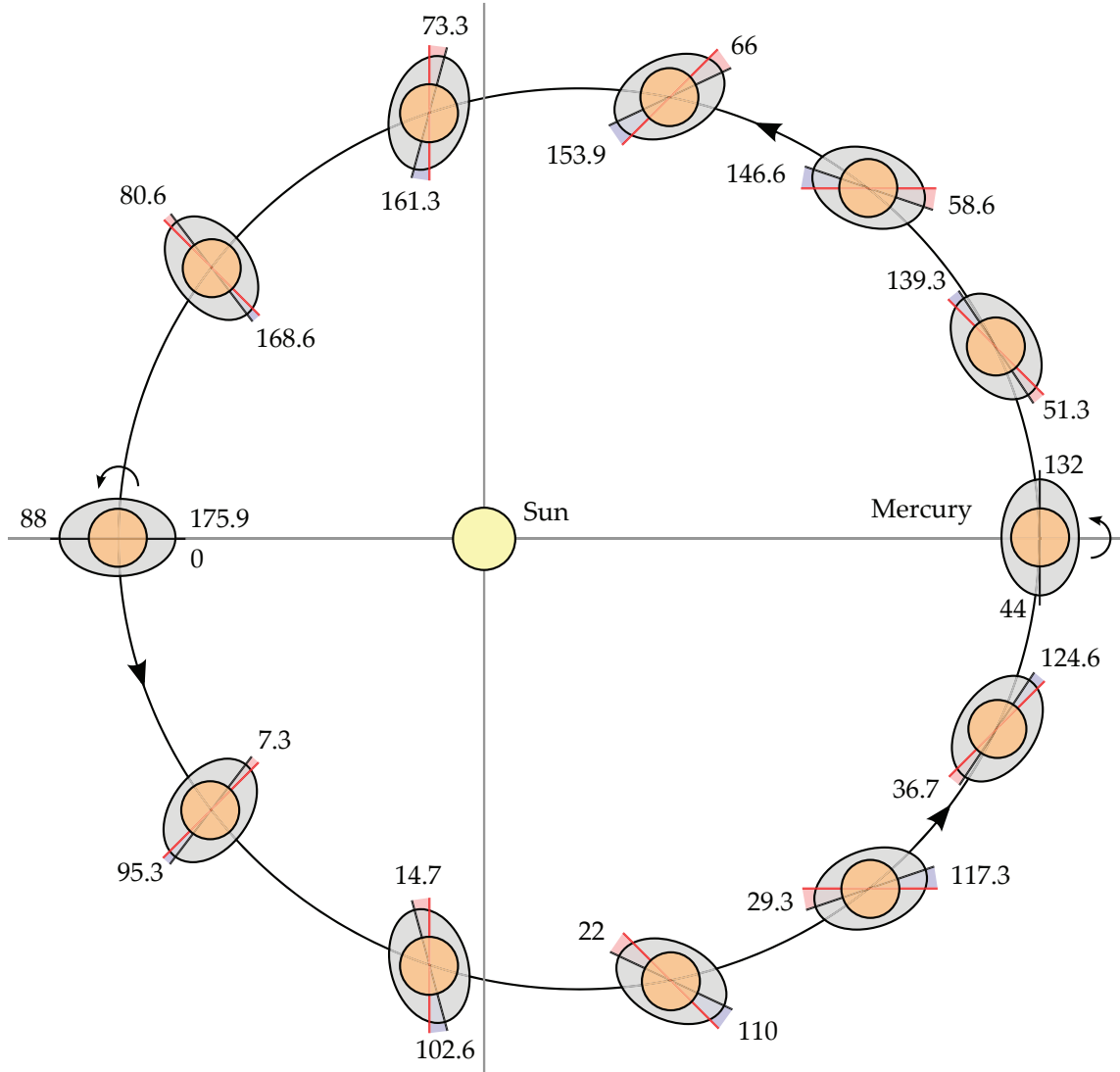


Figure 2: Rotation of Mercury within two revolutions about the Sun. The red line indicates the uniform rotation of Mercury's core and the black line shows the orientation of Mercury's mantle with longitudinal librations. The libration angle in the first and second orbit is indicated by the red and blue shaded areas, respectively. For better visualization the libration amplitude was scaled by a factor of 1800. The spacing between the rotation states represents Mercury at equal time intervals (7.33 days). The numbers nearby to Mercury indicate the time in days since the start of the first orbit at perihelion.

second time with MESSENGER data (Paper III). In particular Peale’s experiment provides estimates for the moments of inertia of the core and the enclosing layer formed by the mantle and crust. In combination with the mass and shape of Mercury these quantities form first order constraints on the interior structure of the planet (e.g. [Hauck et al., 2013](#)). In order to ensure correct interpretation of the rotation state measurements, precise knowledge of the dynamics of Mercury’s orbit, e.g. the orientation and precession of the orbital plane (Paper II), are mandatory. In the following the rotational motion of Mercury will be described in more detail.

### 2.2.1 Longitudinal librations

In general, librations describe a periodic variation of the rotation rate compared to a uniformly rotating body. Thereby, it is important to distinguish between optical and physical librations. Optical librations are only apparent rotation rate changes. They are caused by an eccentric orbit of a satellite when it is observed from the central body. As the body moves on its orbit its velocity changes according to Kepler’s second law. A body locked in a 1:1 spin-orbit resonance will then be observable from the central body to more than 50%, depending on the eccentricity. This phenomenon is well known in connection to our Moon. In contrast, physical or forced librations are actual rotation rate changes in the rotation of the satellite. The amplitude of these physical librations is dependent on the equatorial mass distribution within the satellite. Thus, by measuring this amplitude one can infer information about the interior structure of the planet. When a satellite is in a 1:1 spin-orbit resonance the libration amplitude is dependent on the eccentricity of the orbit and vanishes for a circular orbit. In the case of Mercury with its 3:2 spin-orbit resonance the librations are largest for a circular orbit and are modulated due to the eccentric orbit with higher harmonics of the orbital frequency (see Appendix 1 of this thesis for more details about forced longitudinal librations).

Through the measurement of the libration amplitude of Mercury it is possible to obtain the moment of inertia ratio  $(B - A)/C_m$ , where  $A < B$  are the equatorial moment of inertia of the planet and  $C_m$  is the polar moment of inertia of the mantle and crust. Thereby it is assumed that Mercury’s core is decoupled from the mantle and does not participate in the librational motion of the mantle and crust. In Figure 3 the longitudinal libration angle and rate over one Mercury orbit are visualized for  $(B - A)/C_m = 2.206 \times 10^{-4}$  (Paper III). Note that the possible contribution from the inner core was neglected here, but it can be important in the case of a large inner core (e.g. [Dumberry et al., 2013](#)). The libration rate, i.e. the rotation rate change due to the librations, is at maximum near pericenter where the long-axis of Mercury is aligned to the Sun-Mercury line. The maximal longitudinal displacement in the orientation of Mercury due to the librations occurs

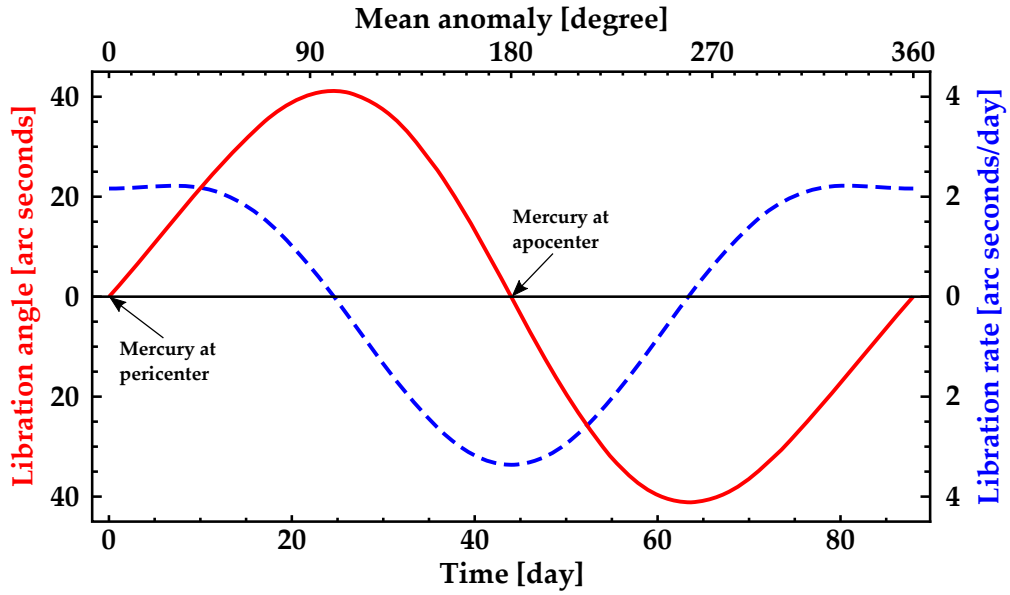


Figure 3: Libration angle (red solid line) and libration rate (blue dashed line) of Mercury as a function of time from the pericenter passage and the mean anomaly of Mercury. The amplitude of the 88 days libration is 38.9 arc seconds (Paper III).

at mean anomaly values of about  $100^\circ$  and  $260^\circ$ , and vanishes at pericenter and apocenter (see Figure 2).

As Mercury's orbit experiences perturbations by other planets the tidal torque from the Sun varies accordingly to the variations in Mercury's distance to the Sun and its motion on its orbit (Peale *et al.*, 2007; Dufey *et al.*, 2008; Peale *et al.*, 2009; Yseboodt *et al.*, 2010). Although these perturbations are small compared to the variations of the tidal torque during one Mercury orbit, they are of great importance when their frequency is close to the free libration frequency of Mercury. The free libration can have arbitrary amplitude and phase, while the frequency depends strongly on the interior structure (Dumberry *et al.*, 2013; Yseboodt *et al.*, 2013). An exogenous trigger, like an impact of a large asteroid or comet for instance can excite free librations. As the free librations do not have a periodic forcing they are damped through dissipation processes. However, a forcing close to the free libration frequency can lead to a resonant enhancement of the response of Mercury. Then additional librations with amplitudes comparable to the one of the annual librations can occur. As the period of the free libration in longitude is about 12 years, this effect on short timescales may only manifests as an apparent increase or decrease in the mean rotation rate (Paper III).

### 2.2.2 Orientation of the rotation axis

Due to the strong tidal torque of the Sun Mercury's rotation axis is locked in a Cassini state ([Margot et al., 2007, 2012](#), Paper III). The Cassini laws, formulated for Earth's moon by Cassini ([Cassini, 1693](#)), were generalized to the rotation of other celestial bodies ([Colombo, 1966](#); [Peale, 1969](#); [Beletskii, 1972](#)). A Cassini state is characterized by the condition that the vector of the rotation axis lies in the plane spanned by the orbital plane normal and the Laplace plane normal. Thereby, the Laplace plane is a fictitious plane to which the orbital plane has a constant inclination. The normal of the orbital plane precesses about the Laplace plane normal and if the body is in a Cassini state the rotation axis follows the precession of the orbital plane. Such a stable configuration corresponds to an extreme of the Hamiltonian describing Mercury's rotation in the gravity field of the Sun.

The angular distance between the rotation axis and the orbit plane normal is the obliquity. For a body in a Cassini state the obliquity depends on its moments of inertia as well as the characteristics of the Laplace plane. The latter can be inferred by an analysis of the ephemeris of Mercury ([Yseboodt and Margot, 2006](#), Paper I). By considering the information on the moments of inertia from the equatorial and polar asymmetry of the gravity field one can infer from the measurement of the obliquity the polar moment of inertia of Mercury ([Peale, 1974, 1981](#); [Noyelles and Lhotka, 2013](#)).

## 2.3 The MESSENGER mission

The National Aeronautics and Space Administration (NASA) spacecraft MESSENGER was launched in August 2004. After four years of journey with one Earth and two Venus flybys the spacecraft had its first encounter with Mercury in 2008. Two flybys about Mercury with closest distance of 200 km were performed in January and October 2008. These were the first spacecraft observations of Mercury since Mariner 10, which collected data from Mercury in 1975. A third Mercury flyby was performed in September 2009 and in March 2011 MESSENGER became the first spacecraft in orbit about Mercury. The MESSENGER mission ended with a controlled impact on Mercury's surface after four years of orbital observations. Prior to that the spacecraft obtained unique data from very low-altitude orbits.

The orbit of MESSENGER during the nominal mission phase was very eccentric and had a period of 12 hours. The closest distance of 200 km was reached near the North pole and the largest distance of about 15,200 km was over the southern hemisphere. In the extended mission phase the orbital period was reduced to 8 hours and the largest distance reduced to 10,300 km. Due to the gravity field of Mercury and the Sun MESSENGER's near-polar orbit was prone to changes and



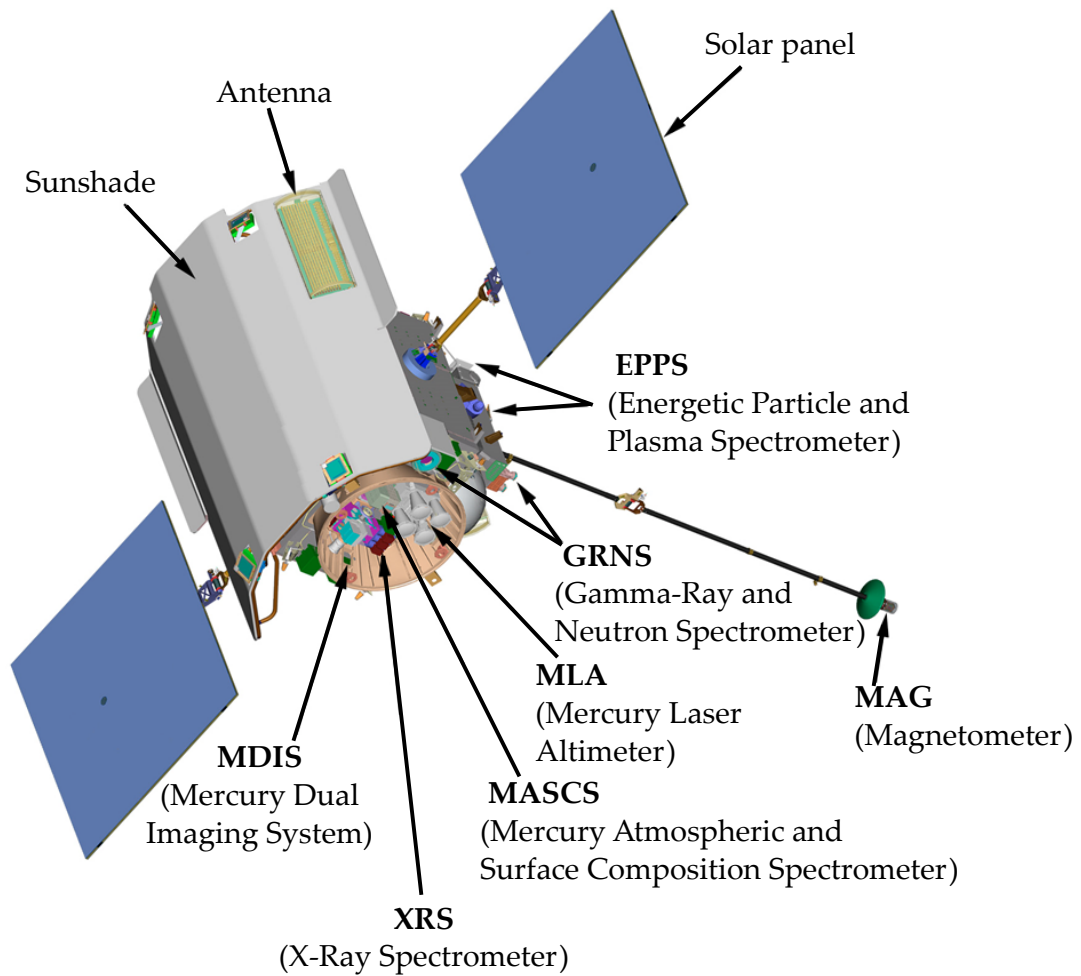


Figure 4: Scheme of the MESSENGER spacecraft with its instruments (Image Credit: NASA/Johns Hopkins University Applied Physics Laboratory/Carnegie Institution of Washington).

12 orbit-correction maneuvers were performed during the orbital phase in order to keep the desired trajectory of the spacecraft.

To cope with the harsh thermal environment in orbit about Mercury the spacecraft was equipped with a heat shield (see Figure 4), which was always orientated in the direction of the Sun and by that constrained the attitude changing performance of the spacecraft. Additionally, in every Mercury orbit about the Sun, the spacecraft had only limited operation capabilities during approximately two weeks. At those times the perapsis of MESSENGER's orbit was over the illuminated hemisphere of Mercury and the thermal flux from the surface prohibited full operation of many scientific instruments.

MESSENGER was equipped with 7 scientific instruments (Figure 4). In the following the Mercury Laser Altimeter (MLA) and the Mercury Dual Imaging System (MDIS) as well as their data products are described in more detail.

### 2.3.1 The Mercury Laser Altimeter (MLA)

The MLA instrument performed laser altimeter measurements to Mercury’s surface at a pulse repetition rate of 8 Hz. Thereby, the laser transmitter emitted 6-ns (FWHM) pulses with 20 mJ of energy at a wavelength of 1,064 nm ([Cavanaugh et al., 2007](#)). The emitted pulse started a counter with a time resolution of 2 GHz. The pulse was reflected at the surface and a small portion of the reflected light was collected by the receiver optics of the instrument. The light was then focused to an avalanche photodiode and was detected through matched electronic filters. At the detection of the return pulse the high-resolution counter was read and the time of flight of the laser pulse was determined with a precision better than 5 ns ([Sun and Neumann, 2015](#)). Per shot up to 15 return-pulse candidates were transmitted to Earth for further processing. The pulse divergence of the emitted laser pulse was 80  $\mu$ rad (full angle at  $e^{-2}$ ), which resulted in a footprint diameter of 16 m at 200 km range. The minimal distance between subsequent footprints was 170 m and increased with the velocity of the spacecraft to about 440 m. The ranging distance of the instrument was dependent on the off-nadir angle and reached up to 1500 km in the nadir orientation.

Using the spacecraft position and attitude information the time of flight measurement by the laser altimeter can be converted into a height measurement representing the topography of Mercury. Consecutive altimeter measurements provide topography profiles and thereby a measurement of the global shape of the planet. In total the MLA instrument obtained 3226 laser profiles. Due to the spacecraft’s eccentric orbit the measurements by MLA were largely constrained to the northern hemisphere (Figure 5). The profiles converged near the North pole and only two equatorial profiles were obtained at the first and second Mercury flybys.

The accuracy of the laser altimeter range measurement suffers at surfaces with high slopes or large off-nadir pointing. The conversion of the range measurement into a height measurement on the ground depends strongly on the knowledge in the spacecraft attitude and position (see Paper II for a detailed discussion).

### 2.3.2 The Mercury Dual Imaging System (MDIS)

The MDIS instrument consisted of two frame cameras, the Narrow Angle Camera (NAC) with a field of view of  $1.5^\circ \times 1.5^\circ$  and the Wide Angle Camera (WAC) with a field of view of  $10.5^\circ \times 10.5^\circ$ . Each camera had a  $1024 \times 1024$  CCD chip, which



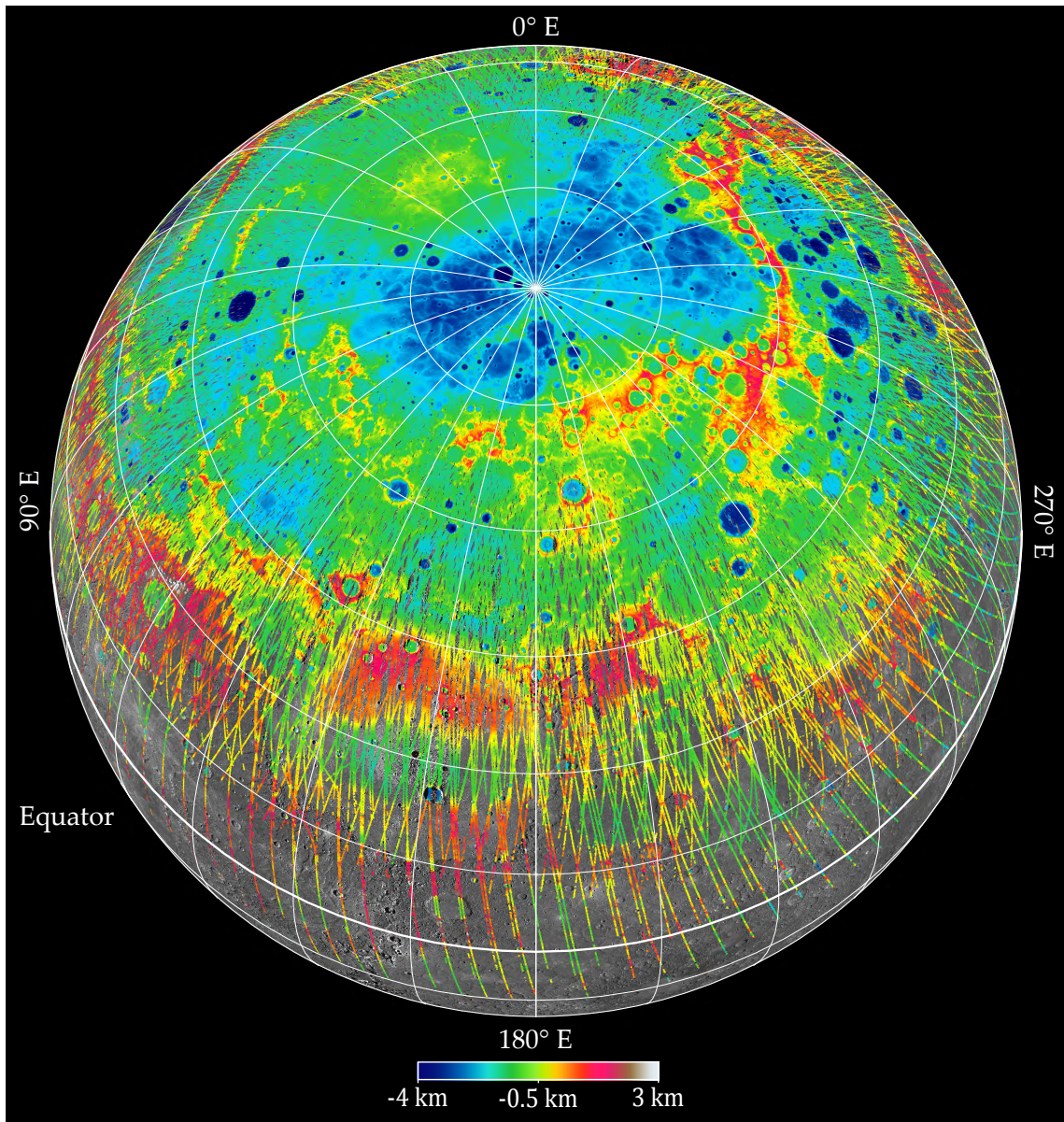


Figure 5: Orthographic projection of laser profiles obtained by the MLA from March 2011 to March 2014. Underneath the laser profiles a mosaic from MDIS images is shown (Image Credit: *NASA/Johns Hopkins University Applied Physics Laboratory/Carnegie Institution of Washington*).



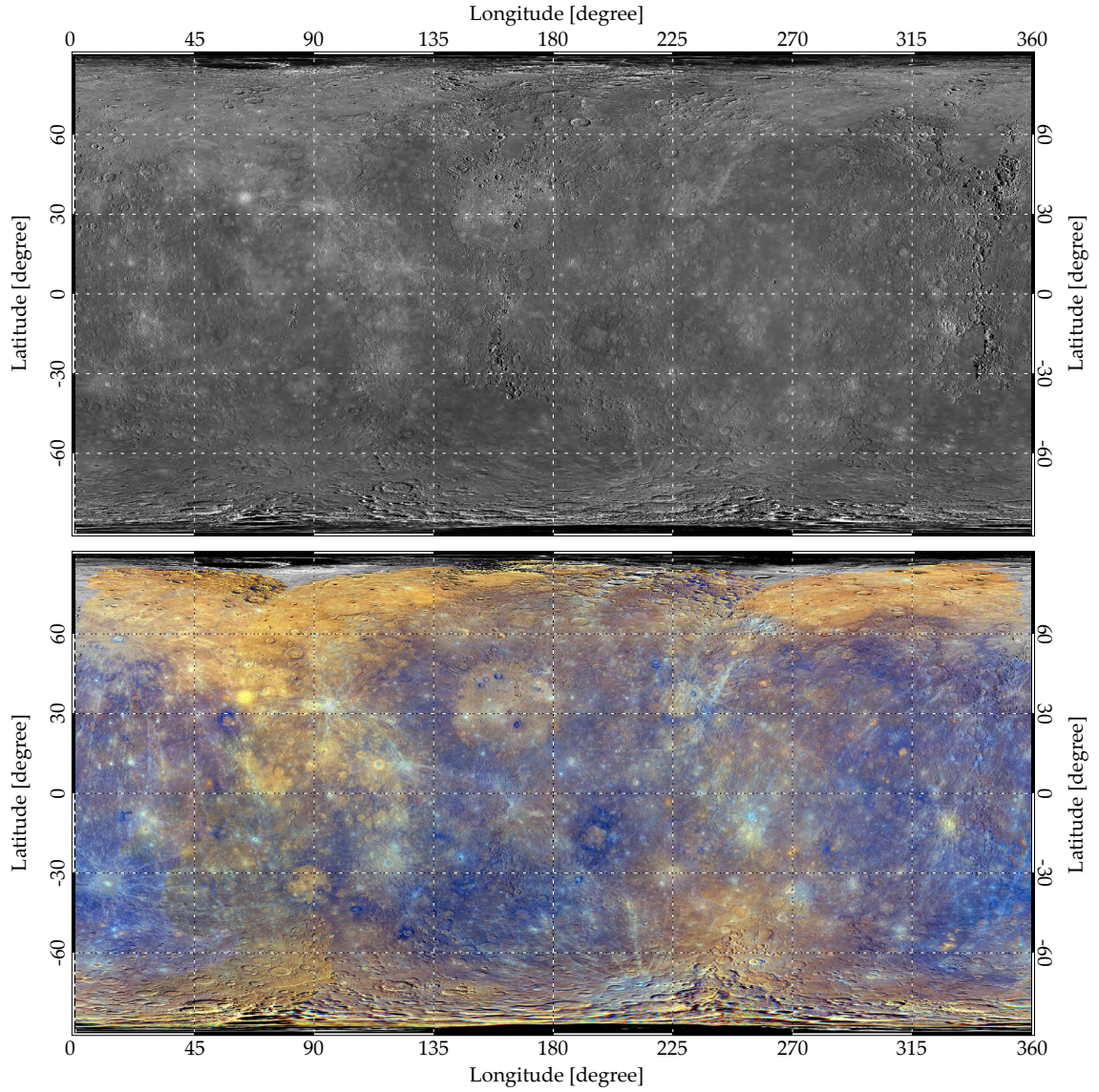


Figure 6: Mosaics of Mercury in a simple cylindrical projection as obtained by the Mercury Dual Imaging System on board the MESSENGER spacecraft. Top: Monochrome mosaic composed of NAC and WAC images acquired in the filter centered at 750 nm. Bottom: Enhanced color mosaic from WAC images (warm and cold colors indicate high and low reflectance, respectively). Image Credit: NASA/Johns Hopkins University Applied Physics Laboratory/Carnegie Institution of Washington.

results in an image resolution of 5.1 m per pixel and 35.8 m per pixel at 200 km altitude for the NAC and WAC, respectively ([Hawkins et al., 2007](#)). The WAC had a filter wheel with 9 filters covering the spectral range from 395 to 1,040 nm and the NAC had one filter with a range of 700 to 800 nm. In order to relax the pointing constraints of the spacecraft the cameras were mounted on a pivoting platform.

The NAC and WAC routinely obtained images of Mercury's surface from various distances as well as illumination and emission angles. During the MESSENGER mission the complete surface of Mercury was imaged and global mosaics were obtained. Color information had also been obtained through the help of the different filters of the WAC (Figure 6). Overlapping images under similar illumination conditions but different viewing geometries form stereo images, which can be processed to a digital terrain model by means of stereo photogrammetry (stereo DTM).

Here the stereo DTM production steps are briefly summarized (see e.g. [Oberst et al. \(2010\)](#); [Gwinner et al. \(2010\)](#); [Preusker et al. \(2011\)](#); [Oberst et al. \(2014\)](#) for more details). First, conjugate or tie points in the overlapping area of the stereo images are derived using an area-based image correlation technique (multi-image matching). Several ten thousands of those conjugate points are used to perform a photogrammetric block-adjustment, which produces improved camera attitude knowledge at the observation epochs. A combination of three stereo images provides greater accuracy on the block-adjustment results. Using the improved attitude the image correlation process is updated with a smaller search area. This produces a large number of matched points, which are used for triangulation of surface points. In order to generate a gridded DTM the surface points within one grid element are averaged using neighborhood statistics.

The processing of a stereo DTM is usually performed in the Mercury body-fixed frame, which requires knowledge of the rotation of the planet. However, the rotation parameters do not have to be known precisely, because any image coordinate errors caused by an incorrect rotation model can be fully compensated by corrections in the camera attitude. Thanks to the block-adjustment and image-matching all errors in image coordinates can be minimized and a terrain model with high internal position accuracy and rigidity can be obtained. Nevertheless, the absolute position of the DTM with respect to the Mercury center of mass is not well constrained. As a consequence, the DTM may show small lateral and vertical offsets as well as tilts with respect to the Mercury-fixed reference frame (see Paper II).

## 2.4 Mercury's rotation from MESSENGER data

The MESSENGER spacecraft provided a large amount of data from observations in Mercury orbit. By analyzing these data one can derive characteristics of the planet, its rotation, as well as its orbit around the Sun. This task is performed in the subsequent chapters presented in form of research articles. The first paper discusses the most recent ephemeris of Mercury and the derivation of the resonant rotation model based on the orbital motion of the planet. This forms important prerequisites for the interpretation of the actual rotation of Mercury. In the second paper a method for measurement of rotational parameters of Mercury from MESSENGER image and altimeter data is presented. Thereby realistic simulations of MESSENGER data acquisition are performed and used for the estimation of the uncertainty of the rotational parameter measurement. In the last research paper observations of Mercury's rotational state from MESSENGER data are presented. The results are discussed in terms of the resonant rotation model and implications on the knowledge about the interior of Mercury are assessed. In the chapter following the three research articles the results are discussed altogether and broader implications on the interior structure and the reference frame of Mercury are performed. Finally, the main results of this thesis are summarized in the synthesis chapter.

## References

- Anderson, B. J., et al. (2011), The global magnetic field of Mercury from MESSENGER orbital observations, *Science*, 333(6051), 1859–62.
- Anderson, J. D., G. Colombo, P. B. Esposito, E. L. Lau, and G. B. Trager (1987), The mass, gravity field, and ephemeris of Mercury, *Icarus*, 71(3), 337–349.
- Beletskii, V. V. (1972), Resonance rotation of celestial bodies and Cassini's laws, *Celestial mechanics*, 6(3), 356–378.
- Benkhoff, J., J. van Casteren, H. Hayakawa, M. Fujimoto, H. Laakso, M. Novara, P. Ferri, H. R. Middleton, and R. Ziethe (2010), Bepi-Colombo - Comprehensive exploration of Mercury: Mission overview and science goals, *Planetary and Space Science*, 58(1-2), 2–20.
- Blewett, D. T., et al. (2011), Hollows on Mercury: MESSENGER evidence for geologically recent volatile-related activity, *Science*, 333(6051), 1856–9.
- Byrne, P. K., C. Klimczak, A. M. C. Sengor, S. C. Solomon, T. R. Watters, and S. A. Hauck, II (2014), Mercury's global contraction much greater than earlier estimates, *Nature Geoscience*, 7(4), 301–307.
- Cassini, G. D. (1693), *Traité de l'origine et du progrès de l'astronomie*.
- Cavanaugh, J. F., et al. (2007), The Mercury Laser Altimeter instrument for the MESSENGER mission, *Space Science Reviews*, 131(1-4), 451–479.
- Colombo, G. (1965), Rotational period of the planet Mercury, *Nature*, 208(5010), 575–575.
- Colombo, G. (1966), Cassini's second and third laws, *The Astronomical Journal*, 71, 891.
- Cremonese, G., J. Warell, J. K. Harmon, F. Leblanc, M. Mendillo, and A. L. Sprague (2010), *Techniques and methods in ground-*

- based observation of Mercury, *Planetary and Space Science*, 58(1-2), 61–78.
- Dufey, J., A. Lemaître, and N. Rambaux (2008), Planetary perturbations on Mercury's libration in longitude, *Celestial Mechanics and Dynamical Astronomy*, 101(1-2), 141–157.
- Dumberry, M., A. Rivoldini, T. Van Hoolst, and M. Yseboodt (2013), The role of Mercury's core density structure on its longitudinal librations, *Icarus*, 225(1), 62–74.
- Einstein, A. (1915), Erklärung der Perihelbewegung des Merkur aus der allgemeinen Relativitätstheorie, *Sitzungsberichte der Königlich preussischen Akademie der Wissenschaften*, 47, 831–839.
- Elgner, S., A. Stark, J. Oberst, M. E. Perry, M. T. Zuber, M. S. Robinson, and S. C. Solomon (2014), Mercury's global shape and topography from MESSENGER limb images, *Planetary and Space Science*, 103, 299–308.
- Ernst, C. M., et al. (2015), Stratigraphy of the Caloris basin, Mercury: Implications for volcanic history and basin impact melt, *Icarus*, 250, 413–429.
- Fassett, C. I., et al. (2012), Large impact basins on Mercury: Global distribution, characteristics, and modification history from MESSENGER orbital data, *Journal of Geophysical Research: Planets*, 117(E12), E00L08.
- Goldreich, P., and S. Peale (1966), Spin-orbit coupling in the solar system, *The Astronomical Journal*, 71, 425.
- Grott, M., D. Breuer, and M. Laneuville (2011), Thermo-chemical evolution and global contraction of Mercury, *Earth and Planetary Science Letters*, 307(1-2), 135–146.
- Gwinner, K., et al. (2010), Topography of Mars from global mapping by HRSC high-resolution digital terrain models and orthoimages: Characteristics and performance, *Earth and Planetary Science Letters*, 294(3-4), 506–519.
- Harmon, J. K., M. A. Slade, R. A. Velez, A. Crespo, M. J. Dryer, and J. M. Johnson (1994), Radar mapping of Mercury's polar anomalies, *Nature*, 369(6477), 213–215.
- Hauck, S. A., II, et al. (2013), The curious case of Mercury's internal structure, *Journal of Geophysical Research: Planets*, 118(6), 1204–1220.
- Hawkins, S. E., III, et al. (2007), The Mercury Dual Imaging System on the MESSENGER spacecraft, *Space Science Reviews*, 131(1-4), 247–338.
- Head, J. W., et al. (2011), Flood volcanism in the northern high latitudes of Mercury revealed by MESSENGER, *Science*, 333(6051), 1853–6.
- Johnson, C. L., et al. (2015), Low-altitude magnetic field measurements by MESSENGER reveal Mercury's ancient crustal field, *Science*, 348(6237), 892–895.
- Kholin, I. (1988), Spatial-temporal coherence of a signal diffusely scattered by an arbitrarily moving surface for the case of monochromatic illumination, *Radiophysics and Quantum Electronics*, 31(5), 371–374.
- Kreslavsky, M. A., J. W. Head, G. A. Neumann, M. T. Zuber, and D. E. Smith (2014), Kilometer-scale topographic roughness of Mercury: Correlation with geologic features and units, *Geophysical Research Letters*, 41(23), 8245–8251.
- Ksanfomality, L. V. (2011), Study of the unknown hemisphere of Mercury by ground-based astronomical facilities, *Solar System Research*, 45(4), 281–303.
- Margot, J. L., S. J. Peale, R. F. Jurgens, M. A. Slade, and I. V. Holin (2007), Large longitude libration of Mercury reveals a molten core, *Science*, 316(5825), 710–714.
- Margot, J. L., et al. (2012), Mercury's moment of inertia from spin and gravity data, *Journal of Geophysical Research-Planets*, 117(E12), E00L09.
- Mazarico, E., A. Genova, S. Goossens, F. G. Lemoine, G. A. Neumann, M. T. Zuber, D. E. Smith, and S. C. Solomon (2014), The gravity field, orientation, and ephemeris of Mercury from MESSENGER observations after three years in orbit, *Journal of Geophysical Research-Planets*, 119(12), 2417–2436.

- McClintock, W. E., J. Vervack, R. J., E. T. Bradley, R. M. Killen, N. Mouawad, A. L. Sprague, M. H. Burger, S. C. Solomon, and N. R. Izenberg (2009), MESSENGER observations of Mercury's exosphere: detection of magnesium and distribution of constituents, *Science*, 324(5927), 610–3.
- Michel, N. C., S. A. Hauck, S. C. Solomon, R. J. Phillips, J. H. Roberts, and M. T. Zuber (2013), Thermal evolution of Mercury as constrained by MESSENGER observations, *Journal of Geophysical Research: Planets*, 118(5), 1033–1044.
- Neumann, G. A., et al. (2013), Bright and Dark Polar Deposits on Mercury: Evidence for Surface Volatiles, *Science*, 339(6117), 296–300.
- Nittler, L. R., et al. (2011), The Major-Element Composition of Mercury's Surface from MESSENGER X-ray Spectrometry, *Science*, 333(6051), 1847–1850.
- Noyelles, B., and C. Lhotka (2013), The influence of orbital dynamics, shape and tides on the obliquity of Mercury, *Advances in Space Research*, 52(12), 2085–2101.
- Noyelles, B., J. Frouard, V. V. Makarov, and M. Efroimsky (2014), Spin-orbit evolution of Mercury revisited, *Icarus*, 241, 26–44.
- Oberst, J., F. Preusker, R. J. Phillips, T. R. Watters, J. W. Head, M. T. Zuber, and S. C. Solomon (2010), The morphology of Mercury's Caloris basin as seen in MESSENGER stereo topographic models, *Icarus*, 209(1), 230–238.
- Oberst, J., K. Gwinner, and F. Preusker (2014), Exploration and analysis of planetary shape and topography using stereophotogrammetry, in *Encyclopedia of the Solar System*, edited by T. Spohn, D. Breuer, and T. V. Johnson, 3rd ed., pp. 1223–1233, Elsevier, Boston.
- Padovan, S., J. L. Margot, S. A. Hauck, W. B. Moore, and S. C. Solomon (2014), The tides of Mercury and possible implications for its interior structure, *Journal of Geophysical Research: Planets*, 119(4), 850–866.
- Paige, D. A., et al. (2013), Thermal stability of volatiles in the north polar region of Mercury, *Science*, 339(6117), 300–303.
- Peale, S. J. (1969), Generalized Cassini's laws, *Astronomical Journal*, 74, 483.
- Peale, S. J. (1972), Determination of parameters related to the interior of Mercury, *Icarus*, 17(1), 168–173.
- Peale, S. J. (1974), Possible histories of the obliquity of Mercury, *The Astronomical Journal*, 79, 722.
- Peale, S. J. (1976), Does Mercury have a molten core, *Nature*, 262(5571), 765–766.
- Peale, S. J. (1981), Measurement accuracies required for the determination of a Mercurian liquid core, *Icarus*, 48(1), 143–145.
- Peale, S. J., and T. Gold (1965), Rotation of the planet Mercury, *Nature*, 206(4990), 1240–1241.
- Peale, S. J., M. Yseboodt, and J. L. Margot (2007), Long-period forcing of Mercury's libration in longitude, *Icarus*, 187(2), 365–373.
- Peale, S. J., J. L. Margot, and M. Yseboodt (2009), Resonant forcing of Mercury's libration in longitude, *Icarus*, 199(1), 1–8.
- Peplowski, P. N., et al. (2011), Radioactive Elements on Mercury's Surface from MESSENGER: Implications for the Planet's Formation and Evolution, *Science*, 333(6051), 1850–1852.
- Perry, M. E., et al. (2015), The low-degree shape of Mercury, *Geophysical Research Letters*, 42(17), 6951–6958.
- Pettengill, G. H., and R. B. Dyce (1965), A radar determination of the rotation of the planet Mercury, *Nature*, 206, 1240.
- Preusker, F., J. Oberst, J. W. Head, T. R. Watters, M. S. Robinson, M. T. Zuber, and S. C. Solomon (2011), Stereo topographic models of Mercury after three MESSENGER flybys, *Planetary and Space Science*, 59(15), 1910–1917.
- Rivoldini, A., and T. Van Hoolst (2013), The interior structure of Mercury constrained by the low-degree gravity field and the rotation of Mercury, *Earth and Planetary Science Letters*, 377(0), 62–72.
- Schiaparelli, G. V. (1890), Sulla rotazione di Mercurio, *Astronomische Nachrichten*, 123(16), 241–250.

- Solomon, S. C., et al. (2001), The MESSENGER mission to Mercury: scientific objectives and implementation, *Planetary and Space Science*, 49(14-15), 1445 – 1465.
- Sun, X., and G. A. Neumann (2015), Calibration of the Mercury Laser Altimeter on the MESSENGER spacecraft, *IEEE Transactions on Geoscience and Remote Sensing*, 53(5), 2860–2874.
- Thomas, R. J., D. A. Rothery, S. J. Conway, and M. Anand (2014), Hollows on Mercury: Materials and mechanisms involved in their formation, *Icarus*, 229, 221–235.
- Tosi, N., M. Grott, A. C. Plesa, and D. Breuer (2013), Thermochemical evolution of Mercury’s interior, *Journal of Geophysical Research: Planets*, 118(12), 2474–2487.
- Van Hoolst, T., and C. Jacobs (2003), Mercury’s tides and interior structure, *Journal of Geophysical Research: Planets*, 108(E11), 1–16.
- Wieczorek, M. A., A. C. M. Correia, M. Le Feuvre, J. Laskar, and N. Rambaux (2012), Mercury’s spin-orbit resonance explained by initial retrograde and subsequent synchronous rotation, *Nature Geoscience*, 5(1), 18–21.
- Yseboodt, M., and J. L. Margot (2006), Evolution of Mercury’s obliquity, *Icarus*, 181(2), 327–337.
- Yseboodt, M., J. L. Margot, and S. J. Peale (2010), Analytical model of the long-period forced longitude librations of Mercury, *Icarus*, 207(2), 536–544.
- Yseboodt, M., A. Rivoldini, T. Van Hoolst, and M. Dumberry (2013), Influence of an inner core on the long-period forced librations of Mercury, *Icarus*, 226(1), 41–51.
- Zuber, M. T., et al. (2012), Topography of the Northern Hemisphere of Mercury from MESSENGER Laser Altimetry, *Science*, 336(6078), 217–220.



# Mercury's resonant rotation from secular orbital elements

Alexander Stark<sup>a</sup>, Jürgen Oberst<sup>a,b</sup>, Hauke Hussmann<sup>a</sup>

<sup>a</sup> German Aerospace Center, Institute of Planetary Research, D-12489 Berlin, Germany

<sup>b</sup> Moscow State University for Geodesy and Cartography, RU-105064 Moscow, Russia

The final publication is available at Springer via  
<http://dx.doi.org/10.1007/s10569-015-9633-4>.

## Abstract

We used recently produced Solar System ephemerides, which incorporate two years of ranging observations to the MESSENGER spacecraft, to extract the secular orbital elements for Mercury and associated uncertainties. As Mercury is in a stable 3:2 spin-orbit resonance these values constitute an important reference for the planet's measured rotational parameters, which in turn strongly bear on physical interpretation of Mercury's interior structure. In particular, we derive a mean orbital period of  $(87.96934962 \pm 0.00000037)$  days and (assuming a perfect resonance) a spin rate of  $(6.138506839 \pm 0.000000028)^\circ/\text{day}$ . The difference between this rotation rate and the currently adopted rotation rate (*Archinal et al., 2011*) corresponds to a longitudinal displacement of approx. 67 m per year at the equator. Moreover, we present a basic approach for the calculation of the orientation of the instantaneous Laplace and Cassini planes of Mercury. The analysis allows us to assess the uncertainties in physical parameters of the planet, when derived from observations of Mercury's rotation.



## 1 Introduction

Mercury’s orbit is not inertially stable but exposed to various perturbations which over long time scales lead to a chaotic motion ([Laskar, 1989](#)). The short-term (about few thousand years) evolution of the orbit can be approximated by a secular contribution to the orbital elements. Most prominent is the precession of the pericenter of Mercury’s orbit, which was also an important test of Einstein’s theory of general relativity ([Einstein, 1915](#)). Due to the Sun’s torque on the asymmetric mass distribution of Mercury, the rotation of Mercury is strongly coupled to its evolving orbit. Radar observations ([Pettengill and Dyce, 1965](#)) revealed that Mercury’s rotation period is about 59 days and in a stable 3:2 resonance with its orbital period ([Peale and Gold, 1965](#); [Colombo, 1965](#)). More recently [Margot et al. \(2007\)](#) have used an Earth-based radar-speckle correlation technique to precisely measure the physical libration amplitude and the obliquity of Mercury. By interpretation of these measurements in terms of physical parameters of the planet - following the idea of the Peale experiment ([Peale, 1976, 1981](#)) - the authors concluded that Mercury’s core is at least partially molten ([Margot et al., 2007, 2012](#)).

With the MESSENGER space probe (MErcury Surface, Space ENvironment, GEOchemistry, and Ranging) having entered orbit around Mercury in March 2011, the observational data of Mercury have greatly improved. Further, new Solar System ephemerides which incorporate two years of ranging and Doppler tracking observations to MESSENGER were produced. For the interpretation of the observations of Mercury’s rotation performed by instruments on MESSENGER, precise knowledge of the resonant rotation parameters of Mercury is mandatory. In fact, the resonant spin rate, currently adopted in the rotation model of Mercury, dates back to the first IAU report ([Davies et al., 1980](#)).

In this work we provide updated reference values for Mercury’s rotation assuming the perfectly resonant rotation model based on the most recent planetary ephemerides. These values serve as a basis for the interpretation of the rotational parameters of Mercury, which are proposed to be measured with high precision ([Stark et al., 2015](#)).

## 2 Secular orbital elements of Mercury

Recently, new Solar System ephemerides DE432 from the Jet Propulsion Laboratory (W. M. Folkner, personal communication, 2014) and INPOP13c from the Institut de Mécanique Céleste et de Calcul des Éphémérides ([Fienga et al., 2014](#)) were produced. Besides other improvements these ephemerides incorporate updates to the orbit of Mercury. Both ephemerides although different in their production process and covered time span led to identical results in our calculations. We

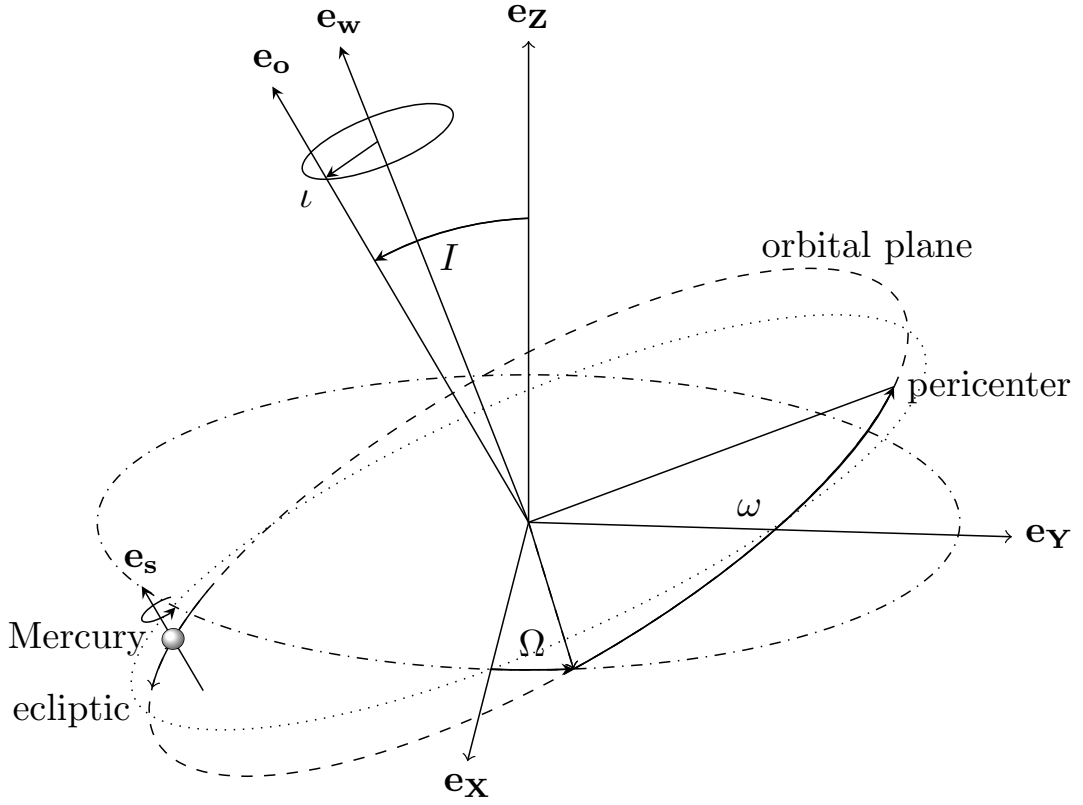


Figure 1: The unit vectors  $\mathbf{e}_{x,y,z}$  denote the International Celestial Reference Frame (ICRF). Mercury’s orbital plane is illustrated by a dashed ellipse and its orientation by the vector  $\mathbf{e}_o$ . The ecliptic and the  $\mathbf{e}_x$ - $\mathbf{e}_y$  plane of the ICRF are given by dotted and dash-dotted ellipses, respectively. The Laplace plane normal is indicated by  $\mathbf{e}_w$  and Mercury’s spin axis by  $\mathbf{e}_s$ . The figure is based on numbers given in Tab. 1 at the J2000.0 epoch.

concentrate here on the DE432 ephemeris and give the orbital elements derived from the INPOP13c ephemeris in appendix 4.

The DE432 ephemeris covers a time span of approximately 1,000 years (1 January 1550 to 1 January 2550). In this time span we derived the osculating Keplerian orbital elements of Mercury from state vectors given with respect to the Sun-centered International Celestial Reference Frame (ICRF). We used a time step of 7 days and set the gravitational parameter of the Sun to

$$GM_{\odot} = 132,712,440,041.9394 \text{ km}^3/\text{s}^2 \text{ (Folkner et al., 2014)}.$$

For the calculation of the osculating orbital elements standard techniques were used (Bate et al., 1970). In order to obtain the secular parts of the elements we

decomposed the osculating orbital elements in a quadratic polynomial and a sum of periodic terms

$$x(t) = x_0 + x_1 t / \text{cy} + x_2 (t / \text{cy})^2 + \sum_i A_i \cos(\nu_i t + \phi_i), \quad (1)$$

where  $x$  stands for a Keplerian orbital element  $a, e, I, \Omega, \omega, M$ , being semi-major axis, eccentricity, inclination, longitude of ascending node, argument of pericenter, and mean anomaly, respectively. The time  $t$  is measured in Julian centuries (cy) from the J2000.0 epoch. Higher order terms in the polynomial were discarded because their estimated uncertainty exceeded the actual value by many orders of magnitude. The periodic terms are characterized by their amplitude  $A_i$ , frequency  $\nu_i$ , and phase  $\phi_i$ . We list these values for ten highest amplitudes of each orbital element in appendix 4.

The decomposition of the osculating orbital elements time series into the form of Eq. 1 was performed with the help of the frequency mapping tool (FAMOUS<sup>1</sup>). This is done because a simple least-squares fit may lead to biased results given the fact that the variations of the orbital elements are in first order periodic and not random. At least 50 frequencies were identified and subtracted from the variation of the orbital elements. The variance of the periodic variations  $\sigma_x^2$  was used to estimate an uncertainty for the coefficients. Thus, orbital elements with relatively high periodic variations receive higher error bars. The uncertainties of the secular coefficients  $x_1$  and  $x_2$  were derived by considering the maximal slope and curvature of the polynomial within the interval  $[-\sigma_x, \sigma_x]$  and a time span of 1000 years. The resulting values are given in Table 1.

In order to demonstrate the convergence of the method we increased the number of frequencies to 100 and found only changes below 2% of the uncertainties of the polynomial coefficients. For further verification of our approach we calculated orbital elements with respect to the ecliptic at J2000.0 (see appendix 4) and compared our results with those published by [Standish and Williams \(2013\)](#). Beside the secular parts of the inclination and longitude of ascending node our values and their uncertainties are consistent with the published values. The discrepancy we found in  $I_1$  and  $\Omega_1$  may result from the fact that we consider the quadratic term, which is significant for these elements. Comparison with other literature values ([Margot, 2009](#); [Noyelles and D’Hoedt, 2012](#); [Noyelles and Lhotka, 2013](#)) shows excellent agreement with our values for these orbital elements.

Additionally, we calculated the precession of the pericenter of Mercury. Note that the secular rates are strongly dependent on the selected reference frame. We used the mean orbital plane of Mercury at J2000.0 (see Sec. 2.2) as reference frame and found a precession of  $575.3 \pm 1.5$  arc sec/cy (see appendix 4). Again this is

<sup>1</sup>F. Mignard, OCA/CNRS, <ftp://ftp.obs-nice.fr/pub/mignard/Famous>

	$x_0$	$x_1$	$x_2$
$a/(10^6 \text{ km})$	57.90909	$0.002 \times 10^{-6}$	$-0.002 \times 10^{-6}$
	$\pm 0.00011$	$\pm 22.34 \times 10^{-6}$	$\pm 4.45 \times 10^{-6}$
$e$	0.2056317	$20.4 \times 10^{-6}$	$-20 \times 10^{-6}$
	$\pm 0.0000071$	$\pm 1.4 \times 10^{-6}$	$\pm 290 \times 10^{-6}$
$I/^\circ$	28.552197	0.0048464	$-9.8 \times 10^{-6}$
	$\pm 0.000036$	$\pm 0.0000073$	$\pm 1.5 \times 10^{-6}$
$\Omega/^\circ$	10.987971	-0.032808	$-12.3 \times 10^{-6}$
	$\pm 0.000099$	$\pm 0.000020$	$\pm 4.0 \times 10^{-6}$
$\omega/^\circ$	67.5642	0.18861	$-3 \times 10^{-6}$
	$\pm 0.0020$	$\pm 0.00040$	$\pm 80 \times 10^{-6}$
$M/^\circ$	174.7948	149472.51579	$8 \times 10^{-6}$
	$\pm 0.0032$	$\pm 0.00063$	$\pm 126 \times 10^{-6}$

Table 1: Secular Keplerian orbital elements of Mercury as derived from the DE432 ephemeris at epoch J2000.0, given with respect to ICRF (see Fig. 1).

in a very good agreement to the literature value of  $(5600.73 - 5025)$  arc sec/cy =  $575.73 \pm 0.41$  arc sec/cy (computed from [Weinberg, 1972](#), p.199).

Another method to obtain the secular orbital elements involve the usage of a secular potential and integration of the averaged differential equation of Mercury’s motion. However, such a method neglects the mutual interaction of the perturbing planets and is not appropriate for precise interpretation of spacecraft data ([Yseboodt and Margot, 2006](#)). More details on averaging methods can be found in e.g., [Sanders et al. \(2007\)](#).

## 2.1 Mean orbital period

The mean period of the orbit is defined as  $T_{\text{orbit}} = 2\pi/n_0$ , where  $n_0$  is the mean motion of Mercury. We can derive  $n_0$  from the first order term of the mean anomaly  $M = M_0 + M_1 t = n_0(t_0 + t)$ . The time  $t_0$  is the elapsed time at J2000.0 since the last pericenter passage. Using the values in Tab. 1 we derive

$$n_0 = M_1 = (4.092334450 \pm 0.000000017)^\circ/\text{day} \quad (2)$$

$$t_0 = M_0/M_1 = (42.71274 \pm 0.00077) \text{ day} \quad (3)$$

$$T_{\text{orbit}} = 360^\circ/M_1 = (87.96934962 \pm 0.00000037) \text{ day}. \quad (4)$$

In order to check the derived value of  $n_0$  we used Kepler’s third law

$$n_0 = \sqrt{GM_\odot/a_0^3}$$

and found  $4.092343 \pm 0.000083^\circ/\text{day}$ . This value is consistent with Eq. 2 but has an error larger by two orders of magnitude.

## 2.2 Mean orbital plane

From the secular parts of the orbital elements  $\Omega$  and  $I$  we can calculate the mean normal vector of the orbital plane by

$$\mathbf{e}_o = \sin \Omega \sin I \mathbf{e}_x - \cos \Omega \sin I \mathbf{e}_y + \cos I \mathbf{e}_z \quad (5)$$

$$= \cos \alpha^{\text{orbit}} \cos \delta^{\text{orbit}} \mathbf{e}_x + \sin \alpha^{\text{orbit}} \cos \delta^{\text{orbit}} \mathbf{e}_y + \sin \delta^{\text{orbit}} \mathbf{e}_z, \quad (6)$$

where  $\mathbf{e}_{x,y,z}$  denote the orientation of the ICRF (see also Fig. 1). Comparing Eq. 5 and 6 we find the right ascension and declination of the orbit pole to be  $\alpha^{\text{orbit}} = \Omega - \pi/2$  and  $\delta^{\text{orbit}} = \pi/2 - I$ . At J2000.0 the values are  $\alpha_0^{\text{orbit}} = (280.987971 \pm 0.000099)^\circ$  and  $\delta_0^{\text{orbit}} = (61.447803 \pm 0.000036)^\circ$ , respectively. From the secular components of  $\Omega$  and  $I$  we can directly derive the first order precession rates of the orbit pole  $\alpha_1^{\text{orbit}} = \Omega_1 = (-0.032808 \pm 0.000020)^\circ/\text{cy}$  and  $\delta_1^{\text{orbit}} = -I_1 = (-0.0048464 \pm 0.0000073)^\circ/\text{cy}$ . It should be noted that the precession of the orbit normal is treated here as a secular variation in inclination and longitude of ascending node, which is justified by the long period of the precession. By that reason the given description of the mean orbital plane is strictly valid only for the time span of the ephemeris, i.e. about  $\pm 500$  years around the J2000.0 epoch. The error bars on the orbit pole orientation and precession rates were obtained through propagation of the uncertainties in the orbital elements. Note that the derived values are in agreement with the findings of [Margot \(2009\)](#) with  $\alpha^{\text{orbit}} = 280.9880^\circ - 0.0328^\circ t/\text{cy}$  and  $\delta^{\text{orbit}} = 61.4478^\circ - 0.0049^\circ t/\text{cy}$ , where DE408 ephemeris and a period of 200 year was used.

## 2.3 Laplace plane

The other planets of the Solar System exert a torque on the orbital plane of Mercury, which leads to a quasi-periodic precession of the orbit normal. Further, the plane to which the inclination of Mercury remains constant, i.e., the Laplace plane, also undergoes slow variations ([Noyelles and D'Hoedt, 2012](#)). Several attempts have been made to calculate the orientation of the Laplace plane normal ([Yseboodt and Margot, 2006](#); [Peale, 2006](#); [D'Hoedt et al., 2009](#)), each of them leading to different results in the Laplace pole position and the precession period (see Fig. 2).

The concept of the "instantaneous" Laplace plane was proposed for Mercury by [Yseboodt and Margot \(2006\)](#) to derive an approximate Laplace plane valid for several thousand years. Note that without additional assumptions the instantaneous precession vector  $\mathbf{w}$  is only constrained to a line. In order to overcome the ambiguity in the instantaneous Laplace plane either a fit to the ephemeris ([Yseboodt and Margot, 2006](#)) or some additional assumptions ([Peale, 2006](#); [D'Hoedt et al., 2009](#)) are used.

Here we introduce a concept of an instantaneous Laplace plane, which removes the ambiguity in its instantaneous orientation and precession frequency. As the only assumption we require the instantaneous Laplace plane to be invariable, i.e.  $\dot{\mathbf{w}} \equiv 0$ . Note that a similar concept was suggested by [Yseboodt \(2011\)](#). When an instantaneous Laplace plane is considered it is also important to clarify in which time period it should be instantaneous. The free precession period of Mercury is in the order of 1000 years ([Peale, 2005](#)). This means that the rotation axis will not be affected by the short period (on the order of decades) changes in the orientation of the orbit normal, but will follow the changes at long periods due to adiabatic invariance ([Peale, 2005](#)). In order to obtain an instantaneous Laplace plane, which is relevant for Mercury's spin, we can neglect all periodic variations and consider only the secular terms.

The general equation for the precession around an axis  $\mathbf{w}$  is

$$\mathbf{w} \times \mathbf{e}_o = \dot{\mathbf{e}}_o. \quad (7)$$

The precession vector  $\mathbf{w}$  is given by  $\mathbf{w} = -\mu \mathbf{e}_w$ , where  $\mathbf{e}_w$  is the orientation of the Laplace plane and  $\mu$  the precession rate. First we multiply both sides of Eq. 7 with  $\mathbf{e}_o$  and obtain

$$\mathbf{w} = (\mathbf{e}_o \times \dot{\mathbf{e}}_o) - \mu \cos \iota \mathbf{e}_o, \quad (8)$$

where we used  $\mathbf{e}_o \cdot \mathbf{w} = -\mu \cos \iota$  and  $\iota$  is the inclination of Mercury's orbit with respect to the Laplace plane. In order to constrain the instantaneous orientation of the Laplace plane we have to find an instantaneous value for  $\mu \cos \iota$ . By differentiating Eq. 7 and the requirement  $\dot{\mathbf{w}} \equiv 0$  we obtain

$$\ddot{\mathbf{e}}_o + \mu^2 \mathbf{e}_o = -\mu \cos \iota \mathbf{w}, \quad (9)$$

where we make use of  $\mathbf{w} \times \dot{\mathbf{e}}_o = \mathbf{w} \times (\mathbf{w} \times \mathbf{e}_o) = -\mu \cos \iota \mathbf{w} - \mu^2 \mathbf{e}_o$ . The differential equation Eq. 9 describes a regular (uniform) rotation of  $\mathbf{e}_o$  around  $\mathbf{e}_w$  with the frequency  $\mu$ . Following the concept of the instantaneous Laplace plane Eq. 9 is only fulfilled with a unique  $\mathbf{w}$  for a specific time  $t$ . By multiplying Eq. 9 with  $\mathbf{e}_o$  and using Eq. 7 we can find

$$\mu \cos \iota = \frac{\dot{\mathbf{e}}_o \cdot (\mathbf{e}_o \times \ddot{\mathbf{e}}_o)}{|\dot{\mathbf{e}}_o|^2}. \quad (10)$$

By using Eq. 5 for  $\mathbf{e}_o$  and  $\ddot{\mathbf{e}}_o$  we can obtain the values of  $\mu \cos \iota$  as it would be in a regular form and by that an expression for the instantaneous Laplace plane. The combination of Eq. 8 and 10 gives the instantaneous Laplace plane orientation

$$\mathbf{w} = (\mathbf{e}_o \times \dot{\mathbf{e}}_o) - \frac{\dot{\mathbf{e}}_o \cdot (\mathbf{e}_o \times \ddot{\mathbf{e}}_o)}{|\dot{\mathbf{e}}_o|^2} \mathbf{e}_o. \quad (11)$$

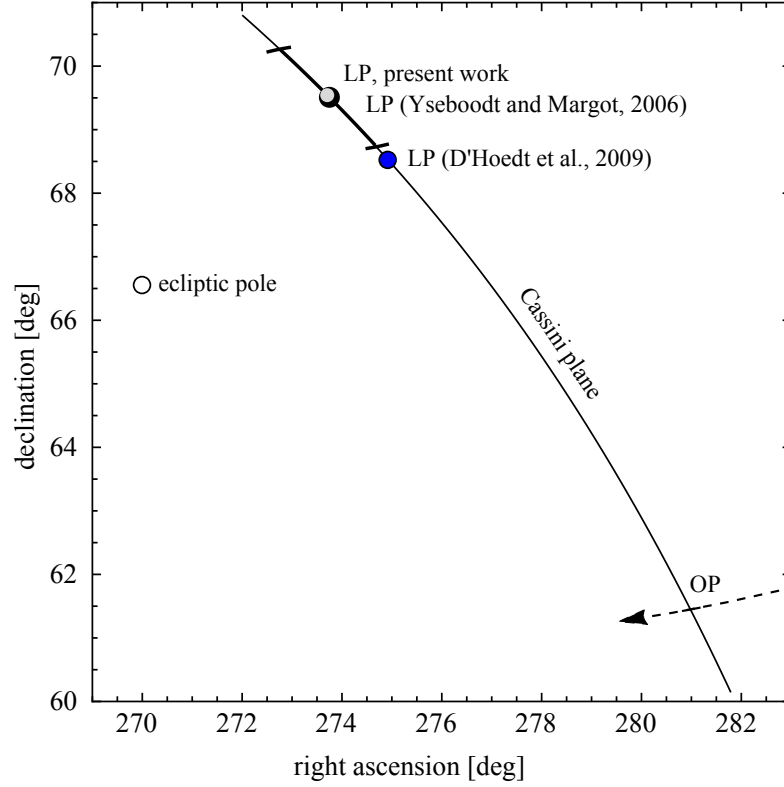


Figure 2: Orientation of the orbit (OP) and the Laplace plane (LP, black disk with error bars) normal at J2000.0 epoch with respect to the ICRF. The precession of the orbit pole around the instantaneous Laplace pole is indicated by a dashed arc. The Laplace plane orientation of [Yseboodt and Margot \(2006\)](#) (grey disk) overlaps with the values derived in this work. Note that the longitude of the Laplace pole is given incorrect in ([D’Hoedt et al., 2009](#)) and was corrected in ([Noyelles and D’Hoedt, 2012](#)). The figure shows the corrected position (blue disk).

Following the formalism of [Peale \(2006\)](#) Eq. 11 can be expressed as

$$\begin{aligned} \mathbf{w} = & (\dot{I} \cos \Omega + (w_z - \dot{\Omega}) \tan I \sin \Omega) \mathbf{e}_X + \\ & + (\dot{I} \sin \Omega - (w_z - \dot{\Omega}) \tan I \cos \Omega) \mathbf{e}_Y + w_z \mathbf{e}_Z \end{aligned} \quad (12)$$

and  $w_z$  given by

$$w_z = \dot{\Omega} + \frac{(\ddot{I}\dot{\Omega} - \dot{I}\ddot{\Omega}) \sin I + \dot{\Omega} \dot{I}^2 \cos I}{\dot{I}^2 + (\dot{\Omega} \sin I)^2} \cos I. \quad (13)$$

The instantaneous Laplace pole given by Eq. 11 is practically equivalent to the fit of the ephemeris to a cone, performed by [Yseboodt and Margot \(2006\)](#).

Using Eq. 11 we calculate the coordinates of the Laplace pole at J2000.0 to  $\alpha_0^{\text{LP}} = (273.8 \pm 1.0)^\circ$  and  $\delta_0^{\text{LP}} = (69.50 \pm 0.77)^\circ$  in the ICRF. It should be noted that the covariance  $\text{Cov}(\alpha_0^{\text{LP}}, \delta_0^{\text{LP}}) = -(0.77^\circ)^2$  is very high, indicating a high



correlation ( $-99.8\%$ ) of the right ascension and declination values. The instantaneous precession rate is  $\mu = (0.00192 \pm 0.00018)/\text{cy}$ ,  $T_{\text{LP}} = (327300 \pm 32000)$  years and  $\iota = (8.58 \pm 0.84)^\circ$ .

However, if Mercury is in a Cassini state (see Sec. 3.4) the determination of the polar moment of inertia from the obliquity is not largely affected by the uncertainties of the Laplace pole ([Yseboodt and Margot, 2006](#); [Peale, 2006](#)). Using our formalism we can derive the relevant quantities and their errors

$$\mu \sin \iota = (2.8645 \pm 0.0016) \times 10^{-6} / \text{years} \quad (14)$$

$$\mu \cos \iota = (18.98 \pm 1.83) \times 10^{-6} / \text{years}. \quad (15)$$

The correlation between  $\mu \sin \iota$  and  $\mu \cos \iota$  is very low

$$\text{Corr}(\mu \sin \iota, \mu \cos \iota) = -10^{-3}.$$

### 3 Mercury’s rotation

#### 3.1 Rotation model

The rotation model of a celestial body consists of a set of values defining its orientation as a function of time with respect to a reference frame. Here we recall briefly the IAU convention of a rotation model for Mercury (e.g. [Archinal et al., 2011](#)).

The orientation of Mercury’s spin axis is described by the right ascension  $\alpha$  and declination  $\delta$  coordinates of the intercept of the spin axis vector  $\mathbf{e}_s$  with the celestial sphere. The spin axis vector  $\mathbf{e}_s$  with respect to the ICRF is given by

$$\mathbf{e}_s = \cos \alpha \cos \delta \mathbf{e}_x + \sin \alpha \cos \delta \mathbf{e}_y + \sin \delta \mathbf{e}_z, \quad (16)$$

where  $\mathbf{e}_{x,y,z}$  denotes the ICRF. The orientation at J2000.0 epoch is denoted by  $\alpha_0$  and  $\delta_0$  and the first order precession rates are  $\alpha_1$  and  $\delta_1$ . The rotational axis is consequently given by

$$\alpha(t) = \alpha_0 + \alpha_1 t \quad (17)$$

$$\delta(t) = \delta_0 + \delta_1 t. \quad (18)$$

The rotation of Mercury around its axis is described by the longitude of the prime meridian  $\varphi_0$ , the rotation rate  $\varphi_1$ , and the physical longitudinal libration  $\varphi_{\text{lib}}$

$$\varphi(t) = \varphi_0 + \varphi_1 t + \varphi_{\text{lib}}(t). \quad (19)$$

The rotation model is of great importance, as it is used to derive body-fixed coordinates of observations performed by spacecraft. The matrix  $\mathbf{R}$  which transforms coordinates from ICRF to body-fixed is composed from three rotations

$$\mathbf{R} = \mathbf{R}_z^T(\varphi) \mathbf{R}_x^T(\pi/2 - \delta) \mathbf{R}_z^T(\alpha + \pi/2), \quad (20)$$



where  $\mathbf{R}_{x,z}$  denote counter-clockwise rotations (right hand rule) around the x- and z-axis, respectively. Note that the spin axis orientation can be computed by  $\mathbf{e}_s = \mathbf{R}_z(\alpha + \pi/2)\mathbf{R}_x(\pi/2 - \delta)\mathbf{e}_z$ .

### 3.2 Resonant rotation

Using the secular orbital elements in Tab. 1 we derive the resonant spin rate of Mercury  $\varphi_1^{(3/2)}$  for the case that the spin is in perfect 3:2 resonance to the motion of the planet on its orbit. Using the mean motion value  $n_0 = M_1$  derived from the mean anomaly and the precession of the argument of pericenter  $\omega_1$  we compute the mean resonant spin rate to

$$\varphi_1^{(3/2)} = \frac{3}{2}n_0 + \omega_1 = (6.138506839 \pm 0.000000028)^\circ/\text{day}. \quad (21)$$

The current value of Mercury's rotation found in the literature is  $6.1385025^\circ/\text{day}$  ([Archinal et al., 2011](#)). The difference between these rates corresponds to a longitudinal displacement of 5.7 arc sec per year (approx. 67 m per year at the equator of Mercury), which should be noticeable during e.g. the MESSENGER mapping mission (where typical image resolution vary from few kilometers to few meters).

We want to stress that the resonant spin rate  $\varphi_1^{(3/2)}$  in the rotation model is composed of the planet's rotation around its spin axis and the precession of Mercury's orbit. Thereby, we have to consider the precession of the argument of pericenter  $\omega_1 = (5.164 \pm 0.011) \times 10^{-6}^\circ/\text{day}$ , and not the precession of the longitude of pericenter  $\varpi_1 = \Omega_1 + \omega_1$  since the precession of the ascending node  $\Omega_1$  is already incorporated in the precession of the rotational axis. Note that the spin rate  $\varphi_1^{(3/2)}$  is defined with respect to a precessing frame and is not strictly "sidereal" since the rotation axis changes slowly its orientation. Further, Mercury has a small but non-zero obliquity of  $i_c = 2.04$  arc min ([Margot et al., 2012](#)). However, the correction arising from the obliquity is in the order of  $i_c\Omega_1^2/I_1$  and can be neglected when comparing with the error of  $\omega_1$  (see appendix 4).

If one of the sub-solar points at perihelion is used for the definition of the prime meridian  $\varphi_0$ , the orientation of Mercury's long axis at J2000.0 with resonant rotation would be

$$\varphi_0^{(3/2)} = \frac{3}{2}M_0 + \omega_0 = (329.7564 \pm 0.0051)^\circ. \quad (22)$$

We find excellent agreement of this value with the findings of [Margot \(2009\)](#), who stated a value of  $329.75^\circ$ . Note that the actual prime meridian of Mercury  $\varphi_0$  is defined with respect to the crater Hun Kal located at  $20^\circ$  W ([Archinal et al., 2011](#)).

### 3.3 Physical libration in longitude

The annual libration of Mercury is closely tied to the revolution of Mercury about the Sun. Of particular importance is the mean anomaly  $M$  of Mercury since it defines the period and the phase of the libration. The libration is modeled as follows ([Goldreich and Peale, 1966](#))

$$\varphi_{\text{lib}}(t) = \sum_k g_{88/k} \sin(k n_0(t + t_0)) . \quad (23)$$

The amplitudes  $g_{88/k}$  follow a recursive relationship

$$g_{88/(k+1)} = g_{88/k} \frac{G_{201}(k+1, e_0)}{G_{201}(k, e_0)} , \quad (24)$$

where  $G_{201}(k, e_0)$  are given by Kaula’s eccentricity functions ([Kaula, 2000](#))

$$G_{201}(k, e) = \frac{G_{201-k}(e) - G_{201+k}(e)}{k^2} . \quad (25)$$

Using  $e_0 = 0.2056317 \pm 0.0000071$  from Tab. 1 we calculate the first five terms to

$$G_{201}(1, e_0) = 0.569650 \pm 0.000027 \quad (26)$$

$$G_{201}(2, e_0) = (-60.0733 \pm 0.0042) \times 10^{-3} \quad (27)$$

$$G_{201}(3, e_0) = (-5920.32 \pm 0.77) \times 10^{-6} \quad (28)$$

$$G_{201}(4, e_0) = (-1200.10 \pm 0.20) \times 10^{-6} \quad (29)$$

$$G_{201}(5, e_0) = (-267.691 \pm 0.053) \times 10^{-6} . \quad (30)$$

The main period of the annual libration is the mean orbital period  $T_{\text{orbit}}$  (Eq. 4) with the phase given by  $M_0 = n_0 t_0$ . In addition, long-period variations of the orbital elements can lead to forced librational motion of Mercury with periods other than the orbital period ([Peale et al., 2007](#); [Yseboodt et al., 2010](#)), but these are not considered in this work.

The measurement of the libration amplitude provides important constraints on the interior structure of Mercury. The amplitude of the annual libration  $g_{88}$  is related by ([Peale, 1981](#))

$$g_{88} = \frac{3}{2} \frac{B - A}{C_m} G_{201}(1, e_0) \quad (31)$$

to the ratio of moments of inertia  $(B - A)/C_m$ , where  $A \leq B < C$  are the principal axes of inertia of the planet and  $C_m$  is the polar moment of inertia of the mantle and crust. Assuming the libration amplitude could be measured with a negligible error, the uncertainty in  $(B - A)/C_m$  would be only at  $6 \times 10^{-7}$ , due to the uncertainty in the eccentricity of Mercury’s orbit. Here we used a libration amplitude of  $g_{88} = 38.5$  arc sec ([Margot et al., 2012](#)).

### 3.4 Cassini state

Mercury is assumed to occupy a Cassini state 1 (Peale, 1969), implying that the spin vector of Mercury  $\mathbf{e}_s$  lies in the plane defined by the Laplace plane normal  $\mathbf{e}_w$  and the orbit normal  $\mathbf{e}_o$  with the latter being enclosed by the others. The spin axis is consequently in a 1:1 resonance to the precession of the orbit normal, i.e.  $\alpha_1 \approx \alpha_1^{\text{orbit}}$  and  $\delta_1 \approx \delta_1^{\text{orbit}}$ . Note that the spin axis precesses with slightly higher rates as described in appendix 4. The Cassini plane  $\mathbf{e}_c$ , which contains all Cassini states can be expressed as a linear combination of the orbit and Laplace plane normal

$$\mathbf{e}_c = r \mathbf{e}_o + s \mathbf{w}. \quad (32)$$

We can constrain  $r$  and  $s$  by  $|\mathbf{e}_c| = 1$  and  $\mathbf{e}_c \cdot \mathbf{e}_o = \cos i_c$ , where  $i_c$  is the obliquity. By using Eq. 8 for  $\mathbf{w}$  and  $|\mathbf{e}_o \times \dot{\mathbf{e}}_o| = |\dot{\mathbf{e}}_o|$  this results in

$$\mathbf{e}_c = \cos i_c \mathbf{e}_o + \sin i_c \frac{\mathbf{e}_o \times \dot{\mathbf{e}}_o}{|\dot{\mathbf{e}}_o|}, \quad (33)$$

with

$$\begin{aligned} \mathbf{e}_o \times \dot{\mathbf{e}}_o &= (\dot{I} \cos \Omega - \dot{\Omega} \sin I \cos I \sin \Omega) \mathbf{e}_x \\ &+ (\dot{I} \sin \Omega + \dot{\Omega} \sin I \cos I \cos \Omega) \mathbf{e}_y + \dot{\Omega} (\sin I)^2 \mathbf{e}_z \end{aligned} \quad (34)$$

$$|\dot{\mathbf{e}}_o| = \mu \sin \iota = \sqrt{\dot{I}^2 + (\dot{\Omega} \sin I)^2}. \quad (35)$$

From Eq. 33 it can be verified that the plane defining the Cassini state is independent from the exact form of the precession of the orbit around the Laplace plane. Especially, it is not dependent on  $w_z$  as recognized by Peale (2006) and Yseboodt and Margot (2006). The Cassini plane is sufficiently defined by the orientation of the orbit normal and its temporal change. In fact, the Cassini plane normal is the vector  $\dot{\mathbf{e}}_o$  given by

$$\begin{aligned} \dot{\mathbf{e}}_o &= (\dot{\Omega} \cos \Omega \sin I + \dot{I} \sin \Omega \cos I) \mathbf{e}_x + \\ &(\dot{\Omega} \sin \Omega \sin I - \dot{I} \cos \Omega \cos I) \mathbf{e}_y - \\ &\dot{I} \sin I \mathbf{e}_z. \end{aligned} \quad (36)$$

With the uncertainty of the orbital elements we can estimate the "thickness" of the Cassini plane, which results from uncertainties in the knowledge of the secular variation of Mercury's ephemeris. At  $i_c = 2.04$  arc min (Margot et al., 2012) we find a  $1\sigma$  thickness of 0.18 arc sec. This allows to interpret possible offsets of Mercury's spin orientation from the exact Cassini state (Margot et al., 2012; Peale et al., 2014).

Using the obliquity  $i_c$  the polar moment of inertia  $C/mR^2$  (scaled with the mass  $m$  and radius  $R$  of Mercury) can be calculated by (Peale, 1981)

$$\frac{C}{mR^2} = \frac{n_0 \sin i_c ((J_2(1 - e^2)^{-3/2} \cos i_c + C_{22}G_{201}(e)(1 + \cos i_c))}{\mu \sin \iota \cos i_c - \mu \cos \iota \sin i_c}, \quad (37)$$

where  $J_2 = 5.03216 \times 10^{-5}$  and  $C_{22} = 0.80389 \times 10^{-5}$  (Mazarico *et al.*, 2014) are the second degree harmonic coefficients of Mercury’s gravity field. Assuming perfect knowledge in the obliquity and the gravitational coefficients the error on  $C/mR^2$  is only at  $6.1 \times 10^{-5}$  due to the uncertainty of the orbital elements. Note that our analysis does not include model uncertainties of Eq. 37, e.g., simplifying assumptions which were made in the derivation of the equation. We only infer the uncertainty of  $C/mR^2$  due to orbital elements if Eq. 37 holds exactly and all other quantities are perfectly known. A more sophisticated analysis including higher order gravity field and tides can be found in Noyelles and Lhotka (2013).

## 4 Discussion and conclusion

In this work we extract orbital elements for Mercury from ephemeris data and predict a mean rotational model for Mercury in the view of a perfect resonance to its orbit. In this case the rotation is, besides the obliquity and the libration amplitude, completely determined by the mean orbital elements and their rates. On the basis of the uncertainties in the mean orbital elements, errors of the theoretical perfectly resonant rotation model can be estimated. Note that ephemeris uncertainties are estimated from the periodic variation of the orbital elements and do not reflect any accuracy or "error" of the ephemeris. They can be rather understood as model uncertainties, since the secular part of Mercury’s orbital elements does not capture the full variation of the orbit. In this work we introduced a consistent approach which allows us to estimate the uncertainties of the rotational parameters resulting from the simplified secular orbital elements. The findings are of great importance for interpretation of the current and future observations of Mercury’s rotation by MESSENGER and BepiColombo spacecraft.

## Appendix 1

The Keplerian orbital elements derived from the INPOP13c ephemeris (Fienga *et al.*, 2014) are given in Tab. 2. We find very little difference of the values when comparing to the DE432 ephemeris (see Tab. 1). The deviation for the trend  $a_1$  of the semi-major axis is about 1.7 meter per century.

In Tab. 3 we give values for reference frame dependent orbital elements with respect to the ecliptic (ECLIP, inclination  $23.439291^\circ$ ), Mercury orbital plane (OP),

	$x_0$	$x_1$	$x_2$
$a/(10^6 \text{ km})$	57.90909	$-44 \times 10^{-12}$	$420 \times 10^{-12}$
$e$	0.2056317	$20.4 \times 10^{-6}$	$-0.027 \times 10^{-6}$
$I/^\circ$	28.552197	0.0048473	$-9.8 \times 10^{-6}$
$\Omega/^\circ$	10.987969	$-0.032808$	$-11.9 \times 10^{-6}$
$\omega/^\circ$	67.5642	0.18862	$-4 \times 10^{-6}$
$M/^\circ$	174.7948	149472.51578	$7 \times 10^{-6}$

Table 2: The same as Tab. 1 but derived from the INPOP13c ephemeris and a time span of 2000 years (09.06.973 AD - 23.06.2973).

and Mercury Laplace plane (LP) at J2000.0. The rotation matrices for the transformation to these reference frames from the ICRF are given by

$$\mathbf{R}_{\text{ECLIP}} = \begin{pmatrix} 1 & 0 & 0 \\ 0 & 0.91748206 & 0.39777716 \\ 0 & -0.39777716 & 0.91748206 \end{pmatrix}, \quad (38)$$

$$\mathbf{R}_{\text{OP}} = \begin{pmatrix} 0.98166722 & 0.19060290 & 0 \\ -0.16742216 & 0.86227887 & 0.47795918 \\ 0.09110040 & -0.46919686 & 0.87838205 \end{pmatrix}, \quad (39)$$

$$\mathbf{R}_{\text{LP}} = \begin{pmatrix} 0.88845611 & 0.43672271 & 0.14113473 \\ -0.45838720 & 0.82896828 & 0.32045711 \\ 0.02295468 & -0.34940643 & 0.93669004 \end{pmatrix}. \quad (40)$$

The precession of the pericenter of Mercury is given by  $\dot{\omega}_1^{\text{OP}} = \dot{\Omega}_1^{\text{OP}} + \dot{\omega}_1^{\text{OP}} = 575.3 \text{ arc sec/cy}$ . The inclination of the orbital plane with respect to the Laplace plane  $I_0^{\text{LP}} = \iota = 8.58^\circ$  remains constant  $I_1^{\text{LP}} = I_2^{\text{LP}} \approx 0$ . The precession of the orbit around the Laplace plane is  $|\dot{\Omega}_1^{\text{LP}}| = \mu = 0.109981^\circ/\text{cy}$ .

## Appendix 2

In Tab. 4 we list the first ten periodic terms, which were identified in the osculating orbital elements time series. Some of the periods can be assigned to planetary perturbations, e.g., Venus:  $(\lambda_V)$  0.62 years;  $(2\lambda_V)$  0.31 years;  $(2\lambda_M - 5\lambda_V)$  5.66 years;  $(\lambda_M - 3\lambda_V)$  1.38 years;  $(\lambda_M - 2\lambda_V)$  1.11 years;  $(2\lambda_M - 4\lambda_V)$  0.55 years; Earth:  $(\lambda_M - 4\lambda_E)$  6.58 years; Jupiter:  $(\lambda_J)$  11.86 years;  $(2\lambda_J)$  5.93 years;  $(3\lambda_J)$  3.95 years; Saturn:  $(2\lambda_S)$  14.73 years, where  $\lambda = M + \omega = M + \Omega + \omega$  denotes the mean longitude of the planet, respectively.

	$x_0$	$x_1$	$x_2$
<i>Ecliptic</i>			
$I/^\circ$	7.004975	0.0059524	$0.7 \times 10^{-6}$
$\Omega/^\circ$	48.330908	-0.125416	$-89.2 \times 10^{-6}$
$\omega/^\circ$	29.1252	0.28428	$80 \times 10^{-6}$
$\varpi/^\circ$	77.4561	0.15886	$-13 \times 10^{-6}$
<i>Mercury orbital plane</i>			
$I/^\circ$	0.0	-0.016413	$-3.9 \times 10^{-6}$
$\Omega/^\circ$	68.735669	-0.054375	$337.0 \times 10^{-6}$
$\omega/^\circ$	320.3895	0.21417	$-350 \times 10^{-6}$
$\varpi/^\circ$	29.1252	0.15980	$-13 \times 10^{-6}$
<i>Mercury Laplace plane</i>			
$I/^\circ$	8.582338	$1 \times 10^{-18}$	$5 \times 10^{-21}$
$\Omega/^\circ$	0.0	-0.109981	$-25.9 \times 10^{-6}$
$\omega/^\circ$	50.3895	0.26855	$13 \times 10^{-6}$
$\varpi/^\circ$	50.3895	0.15857	$-13 \times 10^{-6}$

Table 3: Orbital elements of Mercury as derived from the DE432 ephemeris at epoch J2000.0 with respect to the following reference frames: Ecliptic and Earth equinox of J2000; Mercury orbital plane of J2000.0 and ascending node with respect to the ecliptic; Mercury Laplace plane and ascending node with respect to the Mercury orbital plane of J2000.0.

## Appendix 3

The obliquity of the spin axis  $i_c$  introduces small changes in the precession and resonant rotation rates. To stay within the Cassini plane the spin axis has to precess slightly faster than the orbital plane normal. In order to compute the corrections we expand equation Eq. 33 to first order in the obliquity  $i_c$ . The declination  $\delta$  and right ascension  $\alpha$  of the spin axis are then given by

$$\delta(t) = \frac{\pi}{2} - I + \frac{\dot{\Omega} \sin I}{\sqrt{I^2 + (\dot{\Omega} \sin I)^2}} i_c = \delta_0 + \delta_1 t \quad (41)$$

and

$$\alpha(t) = \Omega - \frac{\pi}{2} + \frac{\dot{I} / \sin I}{\sqrt{I^2 + (\dot{\Omega} \sin I)^2}} i_c = \alpha_0 + \alpha_1 t. \quad (42)$$

By deriving the series in  $t$  we obtain the precession rates at J2000.0

$$\delta_1 = I_1 \left( -1 + \frac{\Omega_1 I_1^2 \cos I_0 + 2(\Omega_2 I_1 - I_2 \Omega_1)}{\sqrt{(I_1^2 + (\Omega_1 \sin I_0)^2)^3}} i_c \right) \quad (43)$$

$a$ [km]				$e$ [ $10^{-6}$ ]		
$i$	$A_i$	$T_i$	$\phi_i$	$A_i$	$T_i$	$\phi_i$
1	109.56	1.11	145.25	7.23	5.93	272.97
2	56.37	0.20	140.65	4.63	1.11	326.10
3	54.55	5.66	356.60	3.53	5.66	181.05
4	35.31	0.29	213.41	2.53	1.38	141.21
5	31.01	0.12	76.038	1.52	11.86	123.83
6	29.41	1.38	325.51	0.89	0.25	261.39
7	21.92	0.13	211.50	0.88	0.55	109.00
8	21.19	0.25	81.45	0.86	14.73	304.98
9	20.27	0.55	285.27	0.81	0.46	128.90
10	19.46	0.40	70.013	0.78	0.29	36.27
$I$ [ $10^{-3}$ arc sec]				$\Omega$ [ $10^{-3}$ arc sec]		
$i$	$A_i$	$T_i$	$\phi_i$	$A_i$	$T_i$	$\phi_i$
1	167.3	5.93	15.01	399.8	5.93	292.75
2	52.5	5.66	71.86	165.8	5.66	135.33
3	31.9	1.38	250.97	145.2	11.86	145.14
4	22.1	11.86	267.19	116.6	1.11	249.76
5	20.1	14.73	58.16	107.3	1.38	189.18
6	17.5	6.58	343.74	57.5	0.62	356.75
7	17.2	3.95	51.01	52.3	0.40	155.89
8	11.8	0.31	326.19	48.3	14.73	336.52
9	9.9	0.24	112.99	44.0	6.56	59.20
10	9.6	0.12	99.47	42.6	0.24	45.75
$\omega$ [arc sec]				$M$ [arc sec]		
$i$	$A_i$	$T_i$	$\phi_i$	$A_i$	$T_i$	$\phi_i$
1	7.36	5.93	180.64	10.71	5.66	87.97
2	4.57	1.11	55.93	8.04	1.11	235.40
3	3.49	5.66	272.57	7.70	5.93	3.50
4	2.55	1.38	50.09	1.92	1.38	230.24
5	1.62	11.86	17.21	1.90	11.86	186.46
6	0.89	14.73	212.80	1.31	6.57	334.16
7	0.84	0.25	351.58	1.22	0.55	17.86
8	0.84	0.55	200.04	1.10	0.46	38.25
9	0.78	0.46	219.04	1.10	0.29	305.42
10	0.78	0.62	194.46	1.09	0.25	171.25

Table 4: Ten leading terms of the decomposition of the time series of the oscillating orbital elements in  $\sum_i A_i \cos(\nu_i t + \phi_i)$  with  $\nu_i = 2\pi/T_i$ . The unit of the amplitude  $A_i$  is given in the brackets beside each orbital elements symbol, respectively. The periods  $T_i$  are given in years and the phases  $\phi_i$  in degrees. The values are given for orbital elements in the ICRF and derived from the DE432 ephemeris.

and

$$\alpha_1 = \Omega_1 - \frac{(I_1^2 \cot I_0 + \Omega_1^2 \sin 2I_0) I_1^2 / \sin I_0}{\sqrt{(I_1^2 + (\Omega_1 \sin I_0)^2)^3}} i_c. \quad (44)$$

For  $i_c = 2.04$  arc min ([Margot et al., 2012](#)) this results in

$$\delta_1 = -0.00486^\circ / \text{cy} \text{ and } \alpha_1 = -0.03291^\circ / \text{cy}. \quad (45)$$

The rotation rate is also slightly modified due to the obliquity. For small  $i_c$  we get

$$\varphi(t) = \frac{3}{2}M + \omega - \frac{\dot{I} \cot I}{\sqrt{\dot{I}^2 + (\dot{\Omega} \sin I)^2}} i_c = \varphi_0^{(3/2)} + \varphi_1^{(3/2)} t. \quad (46)$$

The resonant rotation rate is consequently

$$\begin{aligned} \varphi_1^{(3/2)} = & \frac{3}{2}n_0 + \omega_1 + \\ & + \frac{(I_1 \Omega_1)^2 (3 + \cos 2I_0) / 2 + (\Omega_2 I_1 - I_2 \Omega_1) \Omega_1 \sin 2I_0 + I_1^4 / (\sin I_0)^2}{\sqrt{(I_1^2 + (\Omega_1 \sin I_0)^2)^3}} i_c \end{aligned} \quad (47)$$

and with  $i_c = 2.04$  arc min this amounts to  $6.138506841^\circ / \text{day}$ . The introduced correction is not significant when compared to the error of the resonant rotation rate in Eq. 21.

## Acknowledgments

The authors thank Jean-Luc Margot, Benoît Noyelles, Stanton J. Peale, and Marie Yseboodt for fruitful discussions, and we also thank William M. Folkner and Charles H. Acton for providing information on the DE432 ephemeris. The reviews by two anonymous reviewers significantly improved earlier versions of this manuscript. J.O. greatly acknowledges being hosted by MIIGAiK and supported by the Russian Science Foundation under project 14-22-00197.

Reprinted from [Mercury’s resonant rotation from secular orbital elements](#), Stark, A., Oberst, J., Hussmann, H., *Celestial Mechanics and Dynamical Astronomy*, 123, 263-277, Copyright (2015), with permission from Springer.



## References

- Archinal, B. A., et al. (2011), Report of the IAU Working Group on Cartographic Coordinates and Rotational Elements: 2009, *Celestial Mechanics and Dynamical Astronomy*, 109(2), 101–135.
- Bate, R. R., D. D. Mueller, and J. E. White (1970), *Fundamentals of astrodynamics*, Dover publications, p. 62–64.
- Colombo, G. (1965), Rotational period of the planet Mercury, *Nature*, 208(5010), 575–575.
- Davies, M. E., et al. (1980), Report of the IAU Working Group on Cartographic Coordinates and Rotational Elements of the Planets and Satellites, *Celestial mechanics*, 22(3), 205–230.
- D’Hoedt, S., B. Noyelles, J. Dufey, and A. Lemaître (2009), Determination of an instantaneous Laplace plane for Mercury’s rotation, *Advances in Space Research*, 44(5), 597–603.
- Einstein, A. (1915), Erklärung der Perihelbewegung des Merkur aus der allgemeinen Relativitätstheorie, *Sitzungsberichte der Königlich preussischen Akademie der Wissenschaften*, 47, 831–839.
- Fienga, A., H. Manche, J. Laskar, M. Gastineau, and A. Verma (2014), INPOP new release: INPOP13b, *arXiv preprint arXiv:1405.0484*.
- Folkner, W. M., J. G. Williams, D. H. Boggs, R. S. Park, and P. Kuchynka (2014), The Planetary and Lunar Ephemerides DE430 and DE431, *Interplanetary Network Progress Report*, 196, 1–81.
- Goldreich, P., and S. Peale (1966), Spin-orbit coupling in the solar system, *The Astronomical Journal*, 71, 425.
- Kaula, W. M. (2000), *Theory of Satellite Geodesy: Applications of Satellites to Geodesy*, 36–38 pp., Dover, Mineola, N.Y., 160 p.
- Laskar, J. (1989), A numerical experiment on the chaotic behaviour of the Solar System, *Nature*, 338(6212), 237–238.
- Margot, J. L. (2009), A Mercury orientation model including non-zero obliquity and librations, *Celestial Mechanics and Dynamical Astronomy*, 105(4), 329–336.
- Margot, J. L., S. J. Peale, R. F. Jurgens, M. A. Slade, and I. V. Holin (2007), Large longitude libration of Mercury reveals a molten core, *Science*, 316(5825), 710–714.
- Margot, J. L., et al. (2012), Mercury’s moment of inertia from spin and gravity data, *Journal of Geophysical Research-Planets*, 117(E12), E00L09.
- Mazarico, E., A. Genova, S. Goossens, F. G. Lemoine, G. A. Neumann, M. T. Zuber, D. E. Smith, and S. C. Solomon (2014), The gravity field, orientation, and ephemeris of Mercury from MESSENGER observations after three years in orbit, *Journal of Geophysical Research-Planets*, 119(12), 2417–2436.
- Noyelles, B., and S. D’Hoedt (2012), Modeling the obliquity of Mercury, *Planetary and Space Science*, 60(1), 274–286.
- Noyelles, B., and C. Lhotka (2013), The influence of orbital dynamics, shape and tides on the obliquity of Mercury, *Advances in Space Research*, 52(12), 2085–2101.
- Peale, S. J. (1969), Generalized Cassini’s laws, *Astronomical Journal*, 74, 483.
- Peale, S. J. (1976), Does Mercury have a molten core, *Nature*, 262(5571), 765–766.
- Peale, S. J. (1981), Measurement accuracies required for the determination of a Mercurian liquid core, *Icarus*, 48(1), 143–145.
- Peale, S. J. (2005), The free precession and libration of Mercury, *Icarus*, 178(1), 4–18.
- Peale, S. J. (2006), The proximity of Mercury’s spin to Cassini state 1 from adiabatic invariance, *Icarus*, 181(2), 338–347.
- Peale, S. J., and T. Gold (1965), Rotation of the planet Mercury, *Nature*, 206(4990), 1240–1241.
- Peale, S. J., M. Yseboodt, and J. L. Margot (2007), Long-period forcing of Mercury’s libration in longitude, *Icarus*, 187(2), 365–373.

- Peale, S. J., J. L. Margot, S. A. Hauck, II, and S. C. Solomon (2014), Effect of core-mantle and tidal torques on Mercury’s spin axis orientation, *Icarus*, 231(0), 206–220.
- Pettengill, G. H., and R. B. Dyce (1965), A radar determination of the rotation of the planet Mercury, *Nature*, 206, 1240.
- Sanders, J. A., F. Verhulst, and J. Murdock (2007), *Some Elementary Exercises in Celestial Mechanics, Applied Mathematical Sciences*, vol. 59, pp. 363 – 376, Springer New York.
- Standish, E. M., and J. G. Williams (2013), Orbital ephemerides of the sun, moon, and planets, in *Explanatory Supplement to the Astronomical Almanac*, edited by S. E. Urban and P. K. Seidelmann, 3 ed., chap. 8, pp. 338–339, University Science Books.
- Stark, A., J. Oberst, F. Preusker, K. Gwinner, S. J. Peale, J.-L. Margot, R. J. Phillips, M. T. Zuber, and S. C. Solomon (2015), Mercury’s rotational parameters from MESSENGER image and laser altimeter data: A feasibility study, *Planetary and Space Science*, 117, 64–72.
- Weinberg, S. (1972), *Gravitation and cosmology: Principle and applications of general theory of relativity*, 199 pp., John Wiley and Sons, Inc., New York.
- Yseboodt, M. (2011), The Laplace plane of Mercury, *EPSC-DPS Joint Meeting 2011, EPSC-DPS2011-996*.
- Yseboodt, M., and J. L. Margot (2006), Evolution of Mercury’s obliquity, *Icarus*, 181(2), 327–337.
- Yseboodt, M., J. L. Margot, and S. J. Peale (2010), Analytical model of the long-period forced longitude librations of Mercury, *Icarus*, 207(2), 536–544.

# Mercury's rotational parameters from MESSENGER image and laser altimeter data: A feasibility study

Alexander Stark<sup>a,b</sup>, Jürgen Oberst<sup>a,c</sup>, Frank Preusker<sup>a</sup>, Klaus Gwinner<sup>a</sup>, Stanton J. Peale<sup>d</sup>, Jean-Luc Margot<sup>e,f</sup>, Roger J. Phillips<sup>g</sup>, Maria T. Zuber<sup>h</sup>, Sean C. Solomon<sup>i,j</sup>

<sup>a</sup> German Aerospace Center, Institute of Planetary Research, D-12489 Berlin, Germany,

<sup>b</sup> Technische Universität Berlin, Institute of Geodesy and Geoinformation Science, D-10623 Berlin, Germany, <sup>c</sup> Moscow State University for Geodesy and Cartography, RU-105064 Moscow, Russia, <sup>d</sup> Department of Physics, University of California, Santa Barbara, CA 93106, USA, <sup>e</sup> Department of Earth, Planetary, and Space Sciences, University of California, Los Angeles, CA 90095, USA, <sup>f</sup> Department of Physics and Astronomy, University of California, Los Angeles, CA 90095, USA, <sup>g</sup> Southwest Research Institute, Boulder, CO 80302, USA, <sup>h</sup> Department of Earth, Atmospheric and Planetary Sciences, Massachusetts Institute of Technology, Cambridge, MA 02139, USA,

<sup>i</sup> Lamont-Doherty Earth Observatory, Columbia University, Palisades, NY 10964, USA,

<sup>j</sup> Department of Terrestrial Magnetism, Carnegie Institution of Washington, Washington, DC 20015, USA

The final publication is available at Elsevier via  
<http://dx.doi.org/10.1016/j.pss.2015.05.006>.

## Abstract

A novel method has been developed to determine the rotational parameters of Mercury from data acquired by the MESSENGER spacecraft. We exploit the complementarity of laser altimeter tracks taken at different rotational phases and rigid stereo terrain models to determine a Mercury rotational model. In particular, we solve for the orientation of the spin axis, the rotation rate, and the amplitude of the forced libration. In this paper, we verify the proposed method and carry out an extensive simulation of MESSENGER data acquisition with assumed rotational parameters. To assess the uncertainty in the rotational parameters we use mission-typical assumptions for spacecraft attitude and position knowledge as well as for small-scale terrain morphology. We find that the orientation of the spin axis and the libration amplitude can be recovered with an accuracy of a few arc seconds from three years of MESSENGER orbital observations. The rotation rate can be determined to within 5 arc seconds per year. The method developed here serves as a framework for the ongoing analysis of data from the MESSENGER spacecraft. The rotational parameters of Mercury hold important constraints on the internal structure and evolution of the planet.

# 1 Introduction

Mercury, located deep in the gravity well of the Sun, displays distinctive dynamics. The rotation and orbital motion of the planet are tidally coupled, and Mercury rotates precisely three times for every two revolutions about the Sun. In addition to its mean rotation, the planet displays small forced librations in longitude, i.e., oscillations about the average rotation rate. Measurements of rotational parameters are of considerable interest, as the amplitude of the forced libration and the planet’s obliquity provide (when combined with gravity field parameters) important constraints on the planet’s interior structure ([Peale, 1976, 1988](#); [Margot et al., 2012](#); [Smith et al., 2012](#); [Hauck et al., 2013](#)). This situation thus offers an opportunity to derive information about a planet’s interior, particularly the size and state of the planetary core, not easily accessible for other planets of the Solar System family.

Measurements of Mercury’s librations and obliquity with Earth-based radar revealed a large libration amplitude (approximately 450 m at the equator), suggesting that Mercury’s core is at least partially molten ([Margot et al., 2007, 2012](#)). With this method, instantaneous spin rate values are obtained from radar time-lag measurements, which have provided the most accurate measurements of the spin rate variations to date. However, the precision remains somewhat limited and prevents the detection of small variations, such as those expected from long-period librations ([Peale et al., 2007](#); [Yseboodt et al., 2010](#)).

Several other techniques have been proposed to measure the rotational parameters of Mercury. An obvious approach is to use images from different rotation phases and apply image correlation techniques to constrain the unknown rotation parameters ([Wu et al., 1997](#); [Jehn et al., 2004](#); [Pfyffer et al., 2011](#)). However, precise camera attitude and spacecraft position information must be available for this approach to be feasible. Alternative methods make use of laser altimetric cross-over points ([Rosat et al., 2008](#)) or employ a separation of the dynamic and static topography by spherical harmonic expansion of the latter ([Koch et al., 2008, 2010](#)). Observations of Mercury’s gravitational field can also be used to determine the rotational parameters ([Cicalò and Milani, 2012](#); [Mazarico et al., 2014](#)). This technique requires precise radio tracking and modeling of non-conservative forces acting on the spacecraft. However, as the dynamics of the gravity field can be influenced by differential rotation of the core, the combination of shape and core rotation could provide more information about the interior structure than either quantity alone.

Here we investigate the quality of measurements obtained by the MErcury Surface, Space ENvironment, GEOchemistry, and Ranging (MESSENGER) spacecraft. Precise measurements of a planet’s rotation rate from an orbiting platform

are far from straightforward, as, for example, a fixed reference against which the rotation can be observed is not readily available. Knowledge of a spacecraft's orbit and instrument pointing data suffer from errors that make the accurate measurement of small libration effects challenging. The application of these methods to MESSENGER data is complicated by the spacecraft's highly eccentric orbit and observational constraints for the instruments set by that orbit as well as by limitations on spacecraft attitude relative to the planet-Sun line. Our new approach combines the benefits of both laser altimetry and stereo imaging to overcome their individual drawbacks. In particular, we discuss the combination of time-dependent, high-accuracy range measurements by the laser altimeter with the static terrain data obtained from stereo images.

In order to assess the potential as well as the limitations of our approach we carry out an extensive simulation of MESSENGER data. We adopt a given topographic model, derived from MESSENGER stereo images, and we perform a simulation of laser altimeter observations given an assumed rotational model for Mercury (see Fig. 1). Then, an attempt is made to recover the rotational parameters by analysis of the simulated data. This simulation serves as a basis for future analysis of actual data acquired by MESSENGER's instruments and the estimation of the rotational parameters of Mercury from those data.

The paper is structured as follows. First we describe the available data from MESSENGER, concentrating specifically on laser altimeter profiles and topographic models generated from stereo images. In the subsequent section we report on forward modeling to generate synthetic laser altimeter profiles. Finally, we describe our method for the measurement of rotational parameters and the results obtained with the simulation.

## 2 MESSENGER data

MESSENGER was inserted into orbit about Mercury in March 2011. Its initial orbit was highly eccentric and near-polar, with a 12 h period. In April 2012, the orbit period was shortened in two propulsive maneuvers to 8 h. For our study, we use data from the Mercury Laser Altimeter (MLA) ([Cavanaugh et al., 2007](#)) and the Mercury Dual Imaging System (MDIS) ([Hawkins et al., 2007](#)). We next describe the data obtained by these instruments.

### 2.1 Laser altimeter

MLA carries out its measurements along approximately great-circle profiles, as the spacecraft moves along its orbit track. With a pulse energy of 20 mJ, the instrument can range from altitudes as great as 1500 km in the nadir orientation

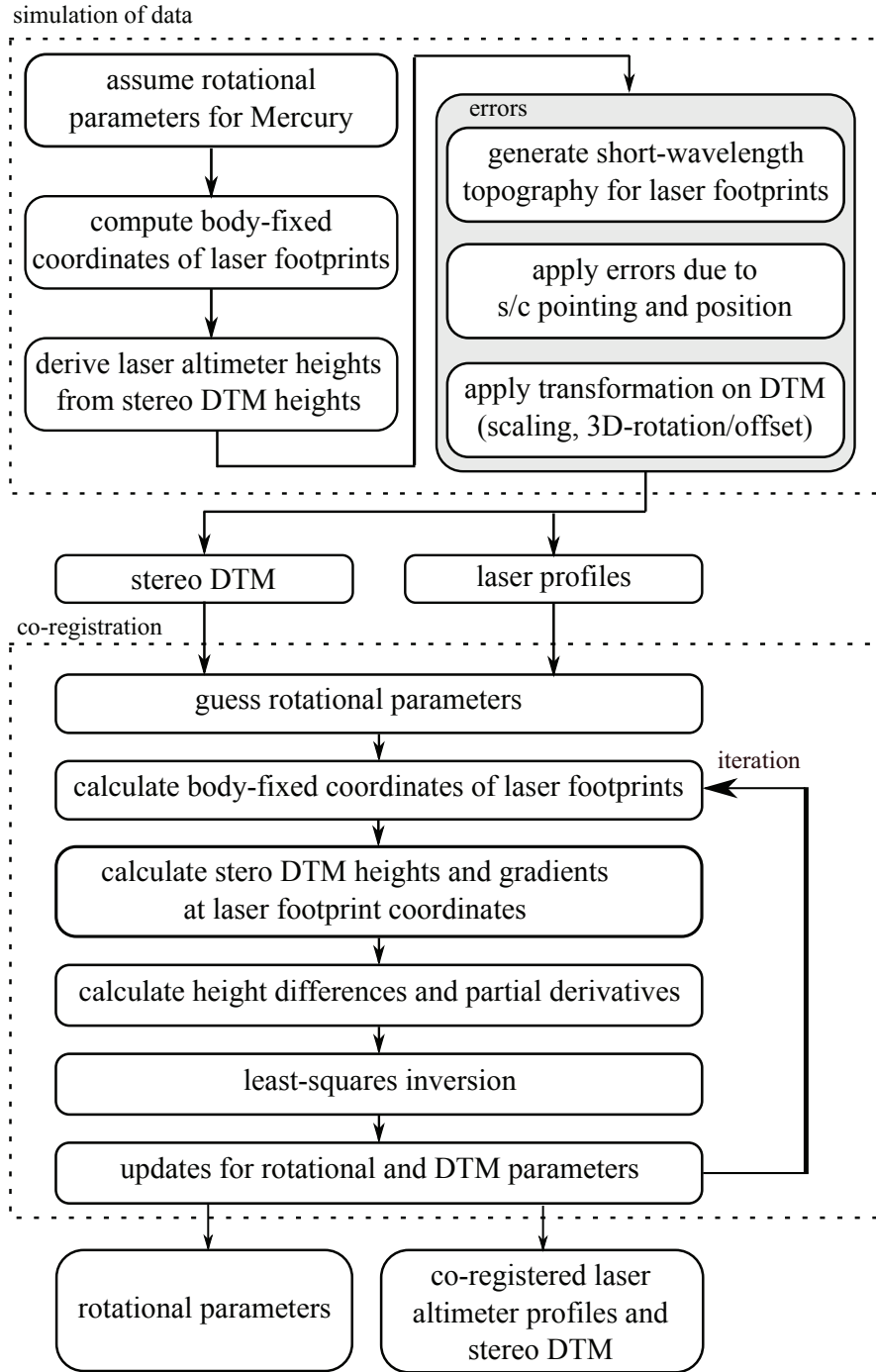


Figure 1: Scheme of the simulation of observational data and determination of rotational parameters (s/c denotes spacecraft, and 3D denotes three-dimensional).

and to distances as great as 1000 km at an off-nadir angle of  $40^\circ$  ([Zuber et al., 2008, 2012](#)). The along-track resolution of the measurements is determined by the size and spacing of the laser footprints on the surface. The distance between footprints at the 8 Hz pulse repetition rate varies with the velocity of the spacecraft between 170 m and 440 m. Depending on the ranging distance, the laser footprint diameters vary from 16 m to 134 m. As of August 2013, after an observation time of 850 days, MLA had acquired 1768 laser profiles that span the latitude range from  $90^\circ$  N to  $20^\circ$  S.

In our simulation, we used laser profiles over a small area of Mercury's surface, for which a digital terrain model (DTM) derived from stereo images is available. The area extends in latitude from  $25$  to  $65^\circ$  N and in longitude from  $190$  to  $270^\circ$  E. Clearly, the final accuracy of the rotational parameters will depend on the size of the DTM area considered and the number of laser altimeter observations within that area.

## 2.2 Stereo photogrammetry

We define the topography represented by the stereo DTM as the length of the local planetary radius from the center of mass of Mercury to the surface, relative to the radius of a reference sphere, here taken as 2440 km.

The production of a DTM from stereo images follows established procedures ([Gwinner et al., 2010](#); [Preusker et al., 2011](#)). With the benefit of image correlation and least-squares block adjustment techniques, we concatenated large numbers of images, and we obtained a terrain model with high internal geometric accuracy and rigidity. On the other hand, the absolute position of a local DTM with respect to Mercury's center of mass is uncertain, and the DTM may show small lateral and vertical offsets as well as tilts with respect to the Mercury-fixed reference frame.

For our study we used a DTM reconstructed from more than 2500 individual MDIS images. Fig. 2 shows a part of the DTM along with the coverage of the same area by MLA. To minimize distortion by the map projection, in our calculations we used a Lambert conic conformal projection with two standard parallels. The DTM is available as a structured map grid with a lateral resolution of 222 m. Although the size of an individual grid element is typically determined by the resolution of the images that were used to generate the terrain model, the effective resolution (i.e., the size of the smallest topographic feature resolved by the DTM) may be larger (see 4.2 below). The vertical resolution of the DTM is about 60 m.



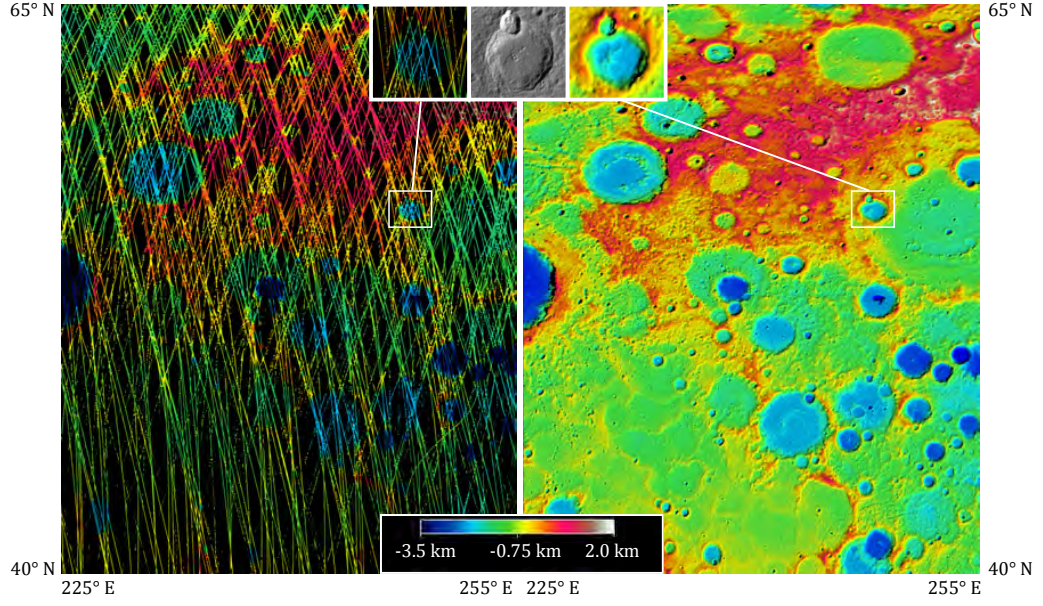


Figure 2: (Left) MLA coverage as of August 2013 of a part (20%) of the area considered in this study. (Right) The same area reconstructed in a stereo DTM. Both maps share the same color bar. The inset shows detailed views of an unnamed crater (centered at  $56.6^\circ$  N,  $24^\circ$  E and enclosed in a white box on both panels) along with an MDIS image (EW0226964842G).

### 3 Rotational model of Mercury

The rotational parameters consist of a set of values defining the orientation of Mercury with respect to a given reference frame at a given epoch. In this study we determined the rotational elements at J2000.0 with respect to the International Celestial Reference Frame (ICRF). The ICRF is approximately (within 0.1 arc sec) the reference frame of the mean Earth equator and equinox of the J2000 epoch (*Archinal et al., 2011*). The orientation of Mercury's spin axis is described by the right ascension  $\alpha_0$  and declination  $\delta_0$  of the intercept of the rotational axis vector with the celestial sphere. The precession of the spin axis is predicted to have a period of around 300,000 years (*Yseboodt and Margot, 2006; Stark et al., 2015*) and is described by  $\alpha_1$  and  $\delta_1$  (expressed in degrees per unit time). The coordinates of Mercury's north pole with respect to the ICRF at a given time  $t$  are given by the angles

$$\alpha(t) = \alpha_0 + \alpha_1 t \quad \text{and} \quad \delta(t) = \delta_0 + \delta_1 t, \quad (1)$$

where the time is measured with respect to the J2000.0 epoch. The rotation of the planet around its spin axis is described by

$$\omega(t) = \omega_0 + \omega_1 t + \sum_k g_{(88/k)} \sin(kn_0(t + t_0)), \quad (2)$$



where  $\omega_0$  is the prime meridian constant,  $\omega_1$  is the rotation rate, and the last term is the physical libration in longitude (Margot, 2009; Yseboodt et al., 2010). The latter is composed from the superposition of  $k$  harmonics of the orbital frequency. The libration is parameterized by the amplitude of the  $k$ th harmonic  $g_{(88/k)}$ , the mean motion  $n_0 = 4.09233445^\circ/\text{day}$ , and the time offset that ties the libration phase to the J2000.0 epoch,  $t_0 = 42.71182$  days. The amplitudes of the harmonics are related by

$$g_{(88/(k+1))} = g_{(88/k)} \frac{G_{(201)}(k+1, e)}{G_{(201)}(k, e)}, \quad (3)$$

where  $G_{(201)}(k, e) = (G_{(201-k)}(e) - G_{(201+k)}(e))/k^2$  is the difference between two Kaula eccentricity functions (Kaula, 2000) and  $e = 0.2056317$  is Mercury's orbital eccentricity (Stark et al., 2015). Given the amplitude of the fundamental frequency  $g_{88}$ , the amplitudes of the higher harmonics can be derived with Eq. 3. The sum in Eq. 2 is truncated at  $k = 5$ , neglecting libration terms with amplitudes below  $10^{-3}$  arc sec.

In our treatment of the rotation of the planet we neglected any long-term (more than 88 days) longitudinal librations. It is expected that because of a resonance effect the perturbation of Mercury's orbit by Jupiter can lead to an 11.86-yr libration with an amplitude comparable to that of the annual libration (Peale et al., 2007; Yseboodt et al., 2010). However, during the observation time considered in this work any long-term libration will appear only as an increase or decrease of the mean spin rate  $\omega_1$ , which is already a parameter of the model. The same holds for the precession rates, which we do not attempt to determine but assume to be fixed at  $\alpha_1 = -0.032808^\circ$  per century and  $\delta_1 = -0.0048464^\circ$  per century (Stark et al., 2015). Any changes in the value of the prime meridian constant  $\omega_0$  are equivalent to a rotation around the polar axis. This rotation will be treated elsewhere, and the prime meridian constant is fixed at  $\omega_0 = 329.5469^\circ$ .

## 4 Simulation of topographic observations

The simulation, outlined in Fig. 1, was conducted as follows. First, from a user-defined rotation model (Table 1), body-fixed coordinates of the MLA footprints were obtained. At these positions we determined the corresponding heights from the stereo DTM derived from MDIS images. We then performed a simulation of MLA measurements across this DTM. To obtain a realistic simulation, we started with the known spacecraft position and attitude and applied typical errors to both quantities (see Section 4.1). To account for the higher spatial resolution of the MLA measurements, we simulated short-wavelength topography by signal synthesis from a random but appropriately distributed power spectrum for topography (see Section 4.2). Finally, as the DTM is also part of the simulation,

we applied a similarity transformation to the DTM, leading to different reference systems for the laser footprints and the DTM. From the simulation we obtained a set of simulated laser profiles and a stereo DTM, which were used for the co-registration and the recovery of rotational parameters (see Section 5).

#### 4.1 Errors in spacecraft position and attitude

The conditions on spacecraft navigation and instrument operation in orbit about Mercury are challenging. The spacecraft is affected by strong and variable solar radiation and planetary thermal flux. The spacecraft must keep its sunshade pointed toward the Sun to within a tolerance of  $\pm 10^\circ$  in pitch and yaw, and a series of attitude changes, many of which result in off-nadir pointing for the MLA, must be performed on every orbit. These off-nadir observations have greater uncertainties in the laser footprint positions. Further, precise orbit information is mandatory to transform laser range measurements to heights on the planet. The reconstruction of MESSENGER's orbit position is complicated by the spacecraft's eccentric orbit and limitations to radio-tracking observations arising from proximity to the Sun. All of these systematic errors can influence the estimation of the rotational parameters.

Typically, cross- and along-track orbit errors are higher than the radial errors. We conservatively assume that radial errors are smaller than 10 m and lateral position errors are smaller than 250 m ([Srinivasan et al., 2007](#)). The uncertainty in the spacecraft attitude over an observation time of 0.1 s (pointing jitter) is assumed to be smaller than  $15 \mu\text{rad}$ , and the attitude knowledge error is assumed to be smaller than  $250 \mu\text{rad}$  ([Santo et al., 2001](#)). The post-launch alignment of MLA with respect to a spacecraft-fixed coordinate system was determined with passive scans during MESSENGER's Earth flyby in 2005 ([Smith et al., 2006](#)). We assume that the remaining alignment error is approximately  $500 \mu\text{rad}$ . Because attitude knowledge and alignment error can compensate each other, a conservative estimate of the total MLA boresight error is given by  $\sqrt{(250 \mu\text{rad})^2 + (500 \mu\text{rad})^2} = 560 \mu\text{rad}$ . All errors are given by one standard deviation ( $1\sigma$ ), i.e., a 68% confidence level, and are assumed to follow a Gaussian distribution.

The spacecraft position and attitude errors are presumed to remain fixed within the short ( $< 11$  min) acquisition time of an individual laser altimeter profile over the stereo DTM. The consideration of measurement conditions allows us to simulate possible correlations between the observational uncertainties and the rotational parameters.

## 4.2 High-resolution topography

Because MLA measurements typically are superior in height resolution to the stereo-derived DTM, we generated artificial high-resolution topography (on the scale of the laser footprint) beyond the resolution of the DTM. Following methods described by [Preusker et al. \(2011\)](#), we first derived the "effective resolution" of the stereo DTM by comparing it with the laser profiles. For the DTM under study with its grid size of 222 m we obtained an effective horizontal resolution of 3.8 km. For further insight, we co-registered actual MLA profiles and the stereo DTM (see Section 5) and performed a Fourier analysis of the residuals. In the frequency spectrum we can observe two regimes (Fig. 3, top) that are separated by the effective DTM resolution. Short-wavelength topography, not realized in the DTM, follows a power-law relation between wavelength and amplitude, whereas residuals at longer wavelengths produce approximately white noise in the spectrum.

We generated synthetic laser altimeter measurements for each MLA profile from randomly generated power spectra having variances that obey the power-wavelength relationship we found from actual data (see Fig. 3, top). After signal synthesis from the spectrum, we obtained simulated height residuals for each MLA "measurement". By adding these residuals to the DTM heights, we produced a laser profile that follows the DTM heights but has an additional synthetic topography with a much finer artificial resolution than the effective resolution of the DTM (Fig. 3, bottom).

## 4.3 Stereo model

We applied offsets to the stereo DTM, as they are typically observed in stereo image processing. In particular, we carried out a seven-parameter similarity transformation, and we shifted the DTM by a three-dimensional offset vector and applied a rotation and scaling (see Section 5). The offset vector is  $(t_x, t_y, t_z) = (400 \text{ m}, 200 \text{ m}, -700 \text{ m})$ . The quaternion forming the similarity transformation is  $(q_0, q_1, q_2, q_3) = (1.0002, 0.00004, 0.00005, 0.0006)$ . This quaternion corresponds to a scaling factor of 1.0004 and a sequential rotation of about 16.5 arc sec, 20.6 arc sec, and 24.7 arc sec around the  $x$ -,  $y$ -, and  $z$ -axes of the body-fixed Mercury frame, respectively, where the  $x$ -,  $y$ -, and  $z$ -axes are in the direction  $0^\circ\text{N}$ ,  $0^\circ\text{E}$ ;  $0^\circ\text{N}$ ,  $90^\circ\text{E}$ ; and  $90^\circ\text{N}$  from the planet center, respectively. This transformation accounts for the different observational and instrumental errors of the MDIS and MLA instruments. The effect of this assumed deformation on height residuals is visualized in Fig. 4 (left panels).

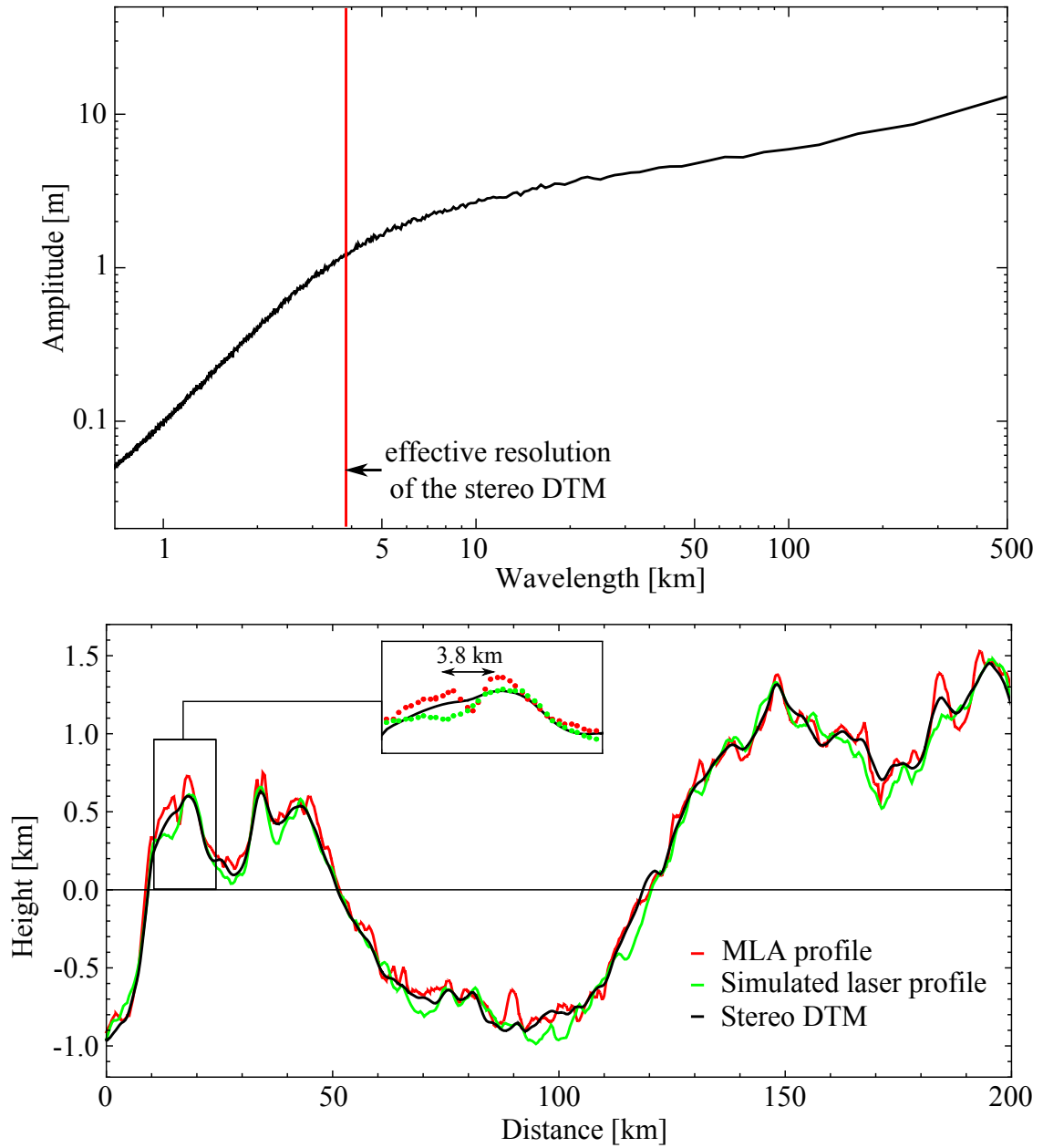


Figure 3: (Top) Averaged power spectrum of the height residuals of MLA profiles along the stereo DTM obtained by a discrete Fourier transform. The red line marks the position of the "effective resolution" of the DTM at 3.8 km. (Bottom) Simulated laser altimeter profile (green) along with actual MLA measurements (red) and stereo DTM heights (black). The inset shows a zoomed view of a portion of the profile; the arrow indicates the "effective resolution" of the DTM.

## 5 Determination of rotational parameters

In the next step, we used the generated synthetic data and attempted to recover the rotational parameters. The key to this step is the co-registration of laser altimeter tracks to the stereo DTM. Thereby we relate a time-dependent, spatially distributed set of laser altimeter footprints to a static and rigid stereo DTM.

Several techniques for co-registration or comparison of laser altimetry and photogrammetrically derived topography have been proposed (e.g., *Habib and Schenk (1999)*; *Baltsavias (1999)*; *Postolov et al. (1999)*). Such techniques have been successfully applied to laser altimeter data and stereo topographic models for Mars and the Moon (*Lin et al., 2010*; *Wu et al., 2013*; *Gläser et al., 2013*). In this work we generalized and extended the method developed by *Gläser et al. (2013)* to the determination of dynamical parameters of a rotating body.

The goal of the co-registration is to find a transformation that relates the reference system of the laser altimeter tracks to the reference system of the stereo DTM. Our approach is to co-register points in three dimensions to a quasi-continuous representation of the surface. For this reason we prefer to solve for the transformation from the laser altimeter points,  $\mathbf{r}_{\text{LA}}$ , to the stereo DTM points,  $\mathbf{r}_{\text{DTM}}$ , although it is the laser altimetry that provides a reliable absolute reference. After the co-registration is performed, it is straightforward to transform the stereo DTM points to the reference frame of the laser altimeter points.

In order to perform the co-registration we assume that the data sets are related by a three-dimensional similarity transformation with seven parameters: a scaling factor, three rotations, and a translation vector  $\mathbf{t} = (t_x, t_y, t_z)$ . The scaling and the rotations are performed by the matrix  $\mathbf{R}_q$ , which is parameterized by a quaternion  $\mathbf{q} = (q_0, q_1, q_2, q_3)$ . The seven parameters of the transformation are  $\mathbf{p}^{\text{DTM}} = (q_0, q_1, q_2, q_3, t_x, t_y, t_z)$ . The transformed laser altimeter points  $\mathbf{r}_{\text{ILA}}^i$  are given by

$$\mathbf{r}_{\text{ILA}}^i = \mathbf{R}_q \left( \mathbf{r}_{\text{LA}}^i + \mathbf{t} \right), \quad (4)$$

where  $i$  is the index for each of the  $n$  laser altimeter points used in the co-registration. The body-fixed coordinates of the laser altimeter points  $\mathbf{r}_{\text{LA}}^i$  are calculated via a rotation matrix  $\mathbf{R}$  from the inertial points  $\mathbf{r}_{\text{ILA}}^i$  by  $\mathbf{r}_{\text{LA}}^i = \mathbf{R} \mathbf{r}_{\text{ILA}}^i$ . The rotation matrix  $\mathbf{R}$ , i.e., a unitary transformation from inertial to body-fixed coordinates, is a composite of three rotations

$$\mathbf{R} = \mathbf{R}_z(\omega(t^i)) \mathbf{R}_x(\delta(t^i)) \mathbf{R}_z(\alpha(t^i)), \quad (5)$$

where  $\mathbf{R}_x$  and  $\mathbf{R}_z$  are rotations around the X- and Z-axes of the ICRF inertial frame, respectively. The time-dependent angles  $\alpha$ ,  $\delta$ , and  $\omega$  define a rotation model (Eqs. 1 and 2) and are evaluated at the time  $t^i$  when the laser pulse

hits the surface. The rotation parameters are  $\mathbf{p}^{\text{rot}} = (\alpha_0, \delta_0, \omega_1, g_{88})$ . Consequently, the transformed points are related to the inertial laser altimeter points by  $\mathbf{r}_{\text{tLA}}^i = \mathbf{R}_q(\mathbf{R} \mathbf{r}_{\text{tLA}}^i + \mathbf{t})$ .

When an optimal set of parameters is found, the radial component of the transformed points  $|\mathbf{r}_{\text{tLA}}^i|$  should be identical to the DTM heights,  $r_{\text{DTM}}^i = |\mathbf{r}_{\text{DTM}}^i|$ . We use radial differences as residuals to be minimized. Hence, the functional model  $g(\mathbf{p})$  for the co-registration is given by

$$\mathbf{g}^i(\mathbf{p}) = r_{\text{DTM}}^i(\lambda^i(\mathbf{p}), \phi^i(\mathbf{p})) - |\mathbf{r}_{\text{tLA}}^i(\mathbf{p})|, \quad (6)$$

where  $\mathbf{p} = (\mathbf{p}^{\text{rot}}, \mathbf{p}^{\text{DTM}})$  is the parameter vector containing the transformation  $\mathbf{p}^{\text{DTM}}$  and the rotation parameters  $\mathbf{p}^{\text{rot}}$ . The DTM heights  $r_{\text{DTM}}^i$  are obtained at the coordinates of the transformed points,  $\mathbf{r}_{\text{tLA}}^i$ , i.e., the latitude  $\lambda^i$  and longitude  $\phi^i$ . These coordinates are obtained from the inertial coordinates  $\mathbf{r}_{\text{tLA}}^i$  and the rotation parameters  $\mathbf{p}^{\text{rot}}$ .

The optimal parameters of this heavily overdetermined problem are obtained iteratively from (Tarantola and Valette, 1982)

$$\mathbf{p}_{k+1} = \mathbf{p}_k - \left( \mathbf{G}_k \mathbf{C}_g^{-1} \mathbf{G}_k^T \right)^{-1} \mathbf{G}_k^T \mathbf{C}_g^{-1} \mathbf{g}(\mathbf{p}_k), \quad (7)$$

where  $\mathbf{C}_g$  is the weighting matrix of the observations (see Section 6), and  $T$  denotes transpose. The matrix of partial derivatives  $\mathbf{G}$  is built from the gradients of the stereo DTM heights

$$G_{ij} = \frac{\partial g^i(\mathbf{p})}{\partial p_j} = \left( \frac{\partial r_{\text{DTM}}^i}{\partial \lambda} \right) \frac{\partial \lambda}{\partial p_j} + \left( \frac{\partial r_{\text{DTM}}^i}{\partial \phi} \right) \frac{\partial \phi}{\partial p_j} - \frac{\partial |\mathbf{r}_{\text{tLA}}^i|}{\partial p_j} \quad (8)$$

and is recalculated every iteration. By using  $\mathbf{r}_{\text{tLA}}^i = (x, y, z)$ ,  $r = |\mathbf{r}_{\text{tLA}}^i|$ ,  $\rho = \sqrt{x^2 + y^2}$ ,  $\lambda = \arcsin(z/r)$ , and,  $\phi = \arctan(y, x)$  we obtain

$$G_{ij} = \left[ \left( \frac{\partial r_{\text{DTM}}^i}{\partial \lambda} \right) \frac{1}{r^2 \rho} \begin{pmatrix} -zx \\ -zy \\ \rho^2 \end{pmatrix} + \left( \frac{\partial r_{\text{DTM}}^i}{\partial \phi} \right) \frac{1}{\rho^2} \begin{pmatrix} -y \\ x \\ 0 \end{pmatrix} - \frac{1}{r} \begin{pmatrix} x \\ y \\ z \end{pmatrix} \right] \cdot \frac{\partial \mathbf{r}_{\text{tLA}}^i}{\partial p_j}. \quad (9)$$

In order to compute the sub-pixel DTM heights  $r_{\text{DTM}}^i(\lambda, \phi)$  and the height gradients  $\partial r_{\text{DTM}}^i / \partial \lambda$  and  $\partial r_{\text{DTM}}^i / \partial \phi$ , an interpolation technique is applied. The nearest DTM grid element to the coordinates of the laser footprint  $(\lambda, \phi)$  is treated as the central grid element. The eight neighboring pixels surrounding the central pixel are used for interpolation. Height differences on the edge of the DTM or in the vicinity of data gaps that do not have eight neighbors are discarded. As described in Section 4.2, the effective resolution of the DTM is approximately an order of magnitude larger than the size of the DTM grid elements. Thus, the topography within the  $3 \times 3$  patch is sufficiently described by a sloped plane, the

parameters of which are determined by a least-squares estimation. From the fitted plane, sub-pixel DTM heights can be extracted at any coordinate pair, and the normal vector of the plane gives the required gradient.

The height differences  $\mathbf{g}(\mathbf{p}) = (g^1(\mathbf{p}), \dots, g^n(\mathbf{p}))$  may contain extreme outliers, caused, for example, by false detections of laser pulses, or small-scale topographic features (e.g., craters) not seen in the stereo DTM. These points can substantially bias the co-registration procedure. Thus, we exclude all observations that are predicted to occur with a probability of less than 1% ( $3\sigma$  threshold). For the initial iteration, the threshold is set to 5 km. At each subsequent iteration step, the threshold criterion is reevaluated to see if measurements that were excluded at the beginning could be incorporated into subsequent co-registration steps.

Because the co-registration is a non-linear method, and thus requires an initial guess of the solution parameters, we initialized the parameters with the assumed (current best estimates) values and performed five iterations to let the parameters evolve to their final values. Given that the improvement in the root mean square (RMS) residual for the subsequent iteration was under the centimeter level, we found five iterations to be sufficient. Starting from different initial values did not change the results but increased the number of iterations needed.

## 6 Data weighting and error estimation

The data used in the co-registration can be weighted in a variety of ways to account for the quality of the measurements. Laser altimeter measurements performed on sloped surfaces, for instance, or at off-nadir orientations are prone to higher errors in the range estimation. These uncertainties can be considered through the covariance of the height differences  $\mathbf{C}_g$ . Our observations are the inertial laser altimeter footprint coordinates and DTM heights, and we must propagate the uncertainties in the observations to the height differences. The observations vector  $\mathbf{h}$  is composed of

$$\mathbf{h} = \left( \lambda_{\text{iLA}}^1, \dots, \lambda_{\text{iLA}}^n, \phi_{\text{iLA}}^1, \dots, \phi_{\text{iLA}}^n, r_{\text{iLA}}^1, \dots, r_{\text{iLA}}^n, r_{\text{DTM}}^1, \dots, r_{\text{DTM}}^m \right), \quad (10)$$

where  $(\lambda_{\text{iLA}}, \phi_{\text{iLA}}, r_{\text{iLA}})$  are the coordinates and height of the laser footprint in the inertial frame and  $r_{\text{DTM}}^i$  are the DTM heights used in the interpolation of the sub-pixel DTM heights. Individual DTM heights can be used to compute more than one observation as a result of the interpolation technique applied to the DTM. Thus, the number of DTM pixels  $m$  is different from the number of laser footprints  $n$ . This situation leads to a block structure of the weighting matrix and reflects correlations among the observations. To calculate the weighting matrix  $\mathbf{C}_g$  we

have to propagate the errors in the observed quantities to the height differences by means of

$$\mathbf{C}_g = \mathbf{T}_h^\top \mathbf{C}_h \mathbf{T}_h, \quad (11)$$

where  $\mathbf{T}_h$  is the matrix of partial derivatives  $[\mathbf{T}_h]_{ij} = \partial g^i / \partial h_j$  of the height differences with respect to the observations  $\mathbf{h}$ , and  $\mathbf{C}_h$  is the covariance of the observations. The variances of the observations are

$$\sigma^2(\lambda_{\text{ILA}}^i) = \frac{(r_{\text{s/c}}^i \sigma_p)^2 + (\sigma_{o\lambda})^2}{R^2}, \quad (12)$$

$$\sigma^2(\phi_{\text{ILA}}^i) = \frac{(r_{\text{s/c}}^i \sigma_p)^2 + (\sigma_{o\phi}^2)^2}{(R \cos \lambda^i)^2}, \quad (13)$$

$$\sigma^2(r_{\text{ILA}}^i) = (\sigma_{or})^2 + (\sigma_h^i)^2, \quad (14)$$

where  $r_{\text{s/c}}^i$  is the range distance from the spacecraft (s/c) to the laser footprint, and  $R = 2440$  km is Mercury's mean radius. We set the uncertainties in the observations according to the simulation (see Section 4). The pointing error is  $\sigma_p = 560 \mu\text{rad}$ , the lateral orbit error is  $\sigma_{o\lambda} = \sigma_{o\phi} = 250$  m, and the radial orbital error is  $\sigma_{or} = 10$  m.  $\sigma_h^i = r_{\text{s/c}}^i \sigma_p \sin \phi^i$  for an off-nadir angle  $\phi^i$ . The DTM pixel error is  $\sigma(r_{\text{DTM}}^i) = 60$  m.

The quantity  $\mathbf{C}_p = (\mathbf{G}^\top \mathbf{C}_g^{-1} \mathbf{G})^{-1}$  gives the precision achievable with the given data but provides no information on the accuracy of the solved parameters. However, we can estimate the accuracy of the proposed method and the underlying data by performing several simulations and calculating the differences between the estimated and the assumed rotational parameters.

We performed 100 different simulations of laser altimeter measurements and estimated the covariance from

$$[\hat{\mathbf{C}}_p]_{ij} = \frac{1}{99} \sum_{n=1}^{100} (p_i^n - p_i^*)(p_j^n - p_j^*), \quad (15)$$

where  $p_i^n$  is the value of the  $i$ th parameter of the  $n$ th simulation, and  $p_j^*$  is the  $j$ th assumed parameter. The expected value  $\hat{\mathbf{p}}$  of the parameters from the simulations is obtained from  $\hat{\mathbf{p}} = 1/100 \sum_{n=1}^{100} \mathbf{p}^n$ . Comparison of the error estimates derived from  $\hat{\mathbf{C}}_p$  with the errors derived from the formal covariance  $\mathbf{C}_p$  shows that the formal errors underestimate the actual errors by a factor of 20.

## 7 Results

A comparison of the "assumed" parameters  $p^*$  with the parameters "estimated" from the simulations  $\hat{\mathbf{p}}$  as well as the parameter errors obtained with Eq. 15 are shown in Table 1. The results indicate that the rotational parameters were determined with high accuracy. The orientation of the spin axis was estimated with an



Table 1: Simulated and estimated values for the rotational parameters.

	simulated	estimated	error ( $1\sigma$ )
$\alpha_0$ [ $^\circ$ ]	281.001030	281.0101	0.0012
$\delta_0$ [ $^\circ$ ]	61.41550	61.41578	0.00072
$\omega_1$ [ $^\circ$ /day]	6.1385025	6.1385025	0.0000038
$g_{88}$ [arc sec]	38.5	38.1	4.6

Notes:  $\alpha_0$  and  $\delta_0$  define the orientation of the spin axis at J2000.0,  $\omega_1$  is the spin rate, and  $g_{88}$  is the libration amplitude. The assumed values are taken from the most recent observations by Earth-based radar (Margot *et al.*, 2012). The estimated  $1\sigma$  errors were calculated from Eq. 15. The precession rates  $\alpha_1$  and  $\delta_1$  as well as the prime meridian  $\omega_0$  were treated as constants.

accuracy of approximately 3 arc sec. Converting the coordinates of the rotation axis to the obliquity, we obtain  $(2.024 \pm 0.042)$  arc min, a value in agreement with the simulated value of 2.041 arc min.

The spin rate parameter  $\omega_1$  contains the highest number of significant figures among the parameters and again shows very good agreement between simulated and assumed values. The estimated  $1\sigma$  uncertainty is only 5 arc sec per year. Thus with the stable body-fixed reference provided through the stereo DTM, it is possible to measure precisely the spin rate and even track its small variation with time, i.e., the libration in longitude. The libration amplitude  $g_{88}$  has an estimated uncertainty of 4.6 arc sec, which corresponds to only 54 m at the equator. Hence, we can confirm that our method and the given data set lead to accurate estimations.

The co-registration involves 11 parameters (four rotational and seven similarity transformation parameters) determined from about 2.16 million of observed height differences. To study the performance of the co-registration we show the height differences before and after co-registration (Fig. 4). The RMS height difference was initially 205 m and decreased to 96 m after co-registration. This final height difference RMS is consistent with the RMS value for simulated heights of 92 m. Furthermore, it can be observed in Fig. 4 that tilts and vertical offsets are minimized during the co-registration process. The lateral offsets between the data sets, which cause relief-like signatures in the height residuals, are removed as well. It is worthwhile to determine the number of observations required to obtain a given accuracy for the parameter estimates. The significance of a parameter in a regression is determined by its  $t$  – statistic  $= \Delta p_i / \sqrt{[\hat{C}_p]_{ii}}$ , where  $\Delta p_i$  is a defined significance of the  $i$ th parameter and  $[\hat{C}_p]_{ii}$  the corresponding estimated variance. We define the significance levels (95%) as follows: 30 arc sec for the right ascension  $\alpha_0$ , 15 arc sec for the declination  $\delta_0$ , 15 arc sec for the libration

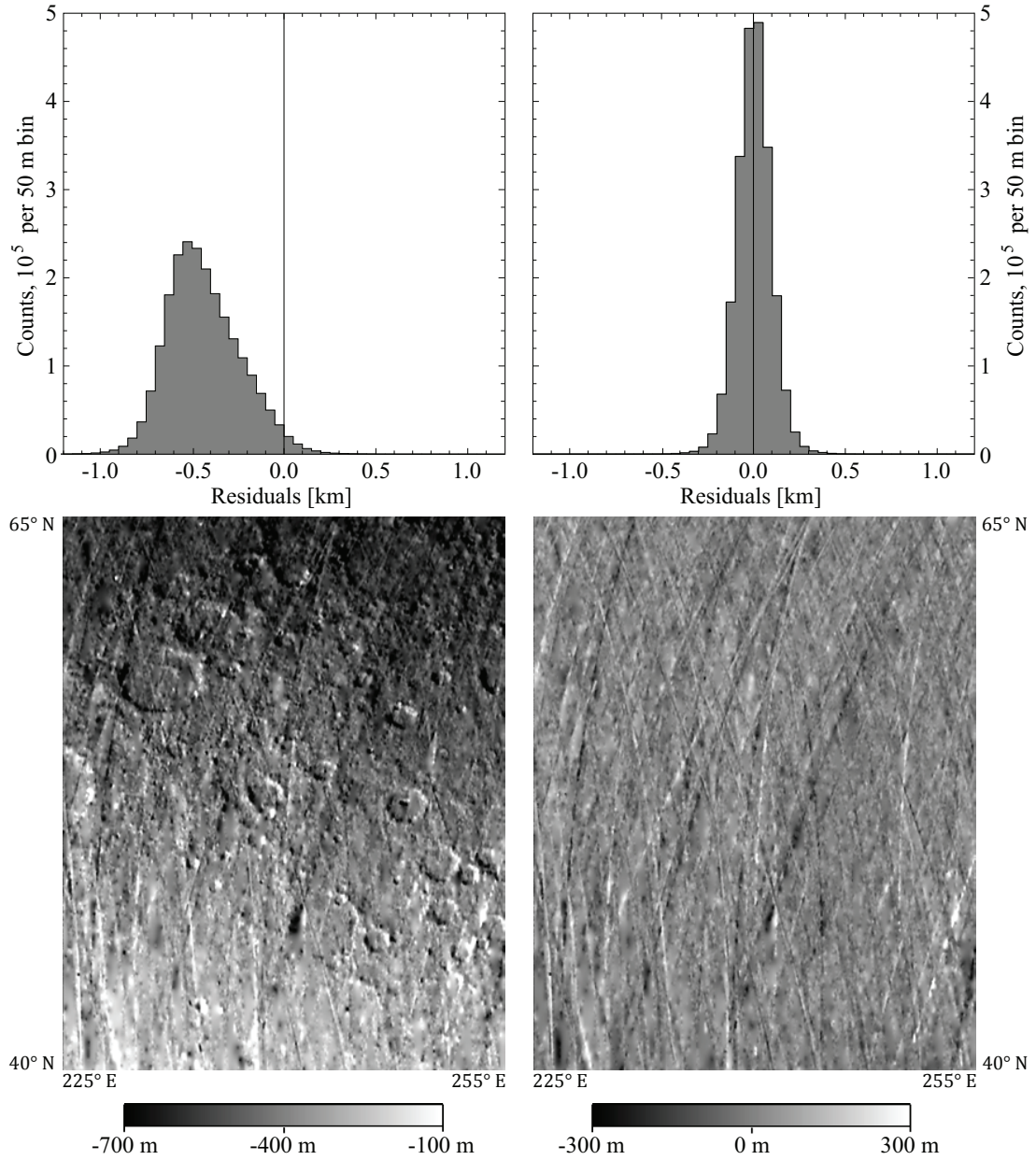


Figure 4: Histogram and map of height residuals before (left) and after (right) co-registration. The map shows the same region as in Fig. 2.

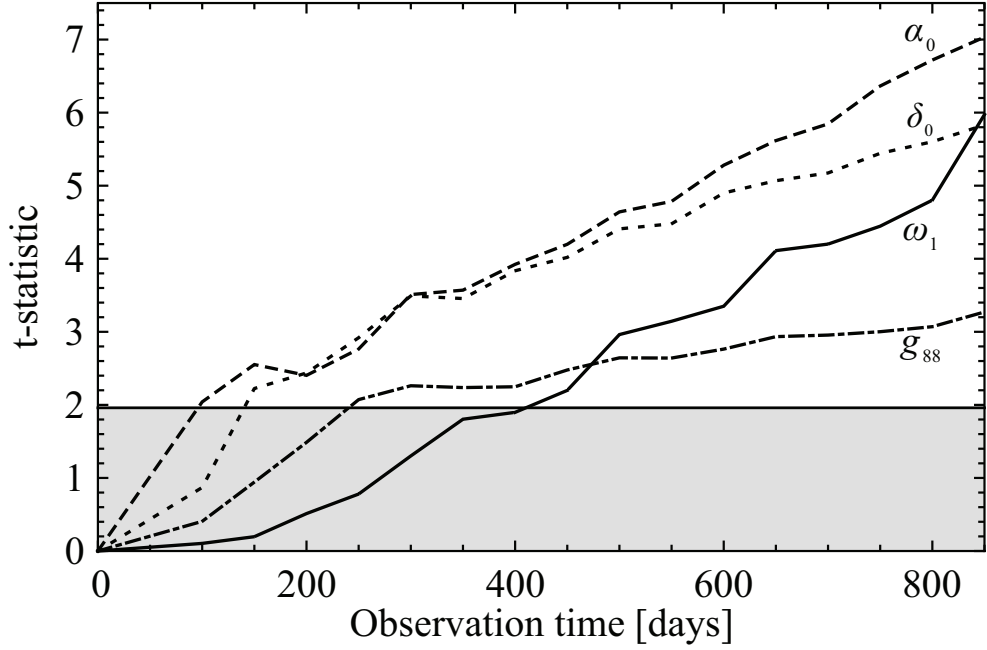


Figure 5:  $t$ -statistic of rotational parameters as a function of observation time (dashed:  $\alpha_0$ ; dotted:  $\delta_0$ ; solid:  $\omega_1$ ; dot-dashed:  $g_{88}$ ). The parameter significance values are defined in the text. The gray shaded area indicates significance levels less than 95%.

amplitude  $g_{88}$ , and 30 arc sec per year ( $0.000023^\circ / \text{day}$ ) for the spin rate  $\omega_1$ . Fig. 5 visualizes the  $t$ -statistic as a function of observation time for the several rotational parameters. The error estimates were obtained with Eq. 15 and appropriately shortened versions of the 100 simulations of laser altimeter measurements. The step size was thereby 50 days (almost one Mercury rotation period). A correction of 15 arc sec (177 m) in the pole position reaches a 95% level of significance after an observing time of approximately 150 (Earth) days. The spin rate and the libration amplitude require the longest observing times (approximately 400 and 250 days, respectively) to become significant at the defined levels. Thus, observation times of several Mercury sidereal days are mandatory to determine precisely the rotation rate and its small oscillations. Whereas the significance of the libration amplitude parameter increases only slowly over time, the spin rate estimation improves quickly, benefiting from any included observations. Note that the significance of the rotational parameters is not only a function of the observing time but also of DTM quality. A stereo DTM with a higher resolution or higher spatial coverage would lead to more accurate estimates within a given observation time.

## 8 Discussion and conclusion

We have demonstrated that it is feasible to determine Mercury’s rotational parameters from image and laser altimeter data acquired by the MESSENGER spacecraft. An extensive simulation of observational data verified that the parameters are estimated correctly by our method.

As an additional benefit, our approach allows the establishment of a global control for individual stereo topographic models by connection through laser altimeter profiles or sparse topographic data, e.g., limb profiles ([Elgner et al., 2014](#)) in the southern hemisphere, where MLA data are not generally available. Although the co-registration method transforms the control points (laser or limb profiles) into the reference frame of the DTM, it is straightforward to compute the inverse transformation that transforms the DTM to the control points. Once co-registration is performed, it is easy to detect outliers and achieve improvements in either of the two data sets. Additional observations, e.g., height differences at intersecting laser profiles (cross-overs), in combination with the co-registration to the stereo DTM, can lead to a substantial increase in the accuracy of the rotational parameters.

The actual data collected by the MESSENGER spacecraft corresponds to a single run of the simulation performed in this study. Thus, the measurements once obtained by the spacecraft cannot be repeated, and any systematic errors may not be evident. We do not correct for systematic errors, but rather we assume that over a long time span the effect of the systematic errors on the rotational parameters can be approximated as random. With the method of this paper we could learn how these errors translate into uncertainties in the rotational parameters and verify that the estimated parameters are unbiased. Usage of additional stereo DTMs ([Preusker et al., 2014](#)) at different locations on Mercury can substantially increase the precision of the estimation. The determination of the orientation of the spin axis can benefit in particular from the extensive MLA coverage at high northern latitudes. Furthermore, a detailed study of the quality of the observational data can be expected to improve the results of parameter estimation. Visual inspection of the height residuals may help to identify systematic errors or outliers.

We see great potential for the method presented here for determining rotational parameters of Mercury from MESSENGER data. Moreover, the formalism developed here is also suitable for other celestial bodies, for which laser altimetry data in combination with stereo topographic models are available or will be in the near future.

## Acknowledgments

This research was funded by a grant from the German Research Foundation (OB124/11-1). The MESSENGER mission is supported by the NASA Discovery Program under contract NAS5-97271 to The Johns Hopkins University Applied Physics Laboratory and NASW-00002 to the Carnegie Institution of Washington. We thank two anonymous reviewers for their thoughtful comments on an earlier version of the manuscript. The authors thank Philipp Gläser, Hauke Hussmann, and Erwan Mazarico for helpful comments and discussions. J. Oberst greatly acknowledges being hosted by MIIGaIK and supported by the Russian Science Foundation under Project 14-22-00197.

Reprinted from *Mercury's rotational parameters from MESSENGER image and laser altimeter data: A feasibility study*, Stark, A., Oberst, J., Preusker, F., Gwinner, K., Peale, S.J., Margot, J.-L., Phillips, R.J., Zuber, M.T., Solomon, S.C., Planetary and Space Science, 117, 64-72, Copyright (2015), with permission from Elsevier.

## References

- Archinal, B. A., et al. (2011), Report of the IAU Working Group on Cartographic Coordinates and Rotational Elements: 2009, *Celestial Mechanics and Dynamical Astronomy*, 109(2), 101–135.
- Baltsavias, E. P. (1999), A comparison between photogrammetry and laser scanning, *ISPRS Journal of Photogrammetry and Remote Sensing*, 54(2-3), 83–94.
- Cavanaugh, J. F., et al. (2007), The Mercury Laser Altimeter instrument for the MESSENGER mission, *Space Science Reviews*, 131(1-4), 451–479.
- Cicalò, S., and A. Milani (2012), Determination of the rotation of Mercury from satellite gravimetry, *Monthly Notices of the Royal Astronomical Society*, 427(1), 468–482.
- Elgner, S., A. Stark, J. Oberst, M. E. Perry, M. T. Zuber, M. S. Robinson, and S. C. Solomon (2014), Mercury's global shape and topography from MESSENGER limb images, *Planetary and Space Science*, 103, 299–308.
- Gläser, P., I. Haase, J. Oberst, and G. A. Neumann (2013), Co-registration of laser altimeter tracks with digital terrain models and applications in planetary science, *Planetary and Space Science*, 89(0), 111–117.
- Gwinner, K., et al. (2010), Topography of Mars from global mapping by HRSC high-resolution digital terrain models and orthoimages: Characteristics and performance, *Earth and Planetary Science Letters*, 294(3-4), 506–519.
- Habib, A., and T. Schenk (1999), A new approach for matching surfaces from laser scanners and optical scanners, in *Mapping Surface Structure and Topography by Airborne and Spaceborne Lasers*, vol. 32-3/W14, edited by B. M. Csatho, International Archives of the Photogrammetry, Remote Sensing and Spatial Information Societies, 7 pp.
- Hauck, S. A., II, et al. (2013), The curious case of Mercury's internal structure, *Journal of Geophysical Research: Planets*, 118(6), 1204–1220.
- Hawkins, S. E., III, et al. (2007), The Mercury Dual Imaging System on the MESSENGER spacecraft, *Space Science Reviews*, 131(1-4), 247–338.

- Jehn, R., C. Corral, and G. Giampieri (2004), Estimating Mercury's 88-day libration amplitude from orbit, *Planetary and Space Science*, 52(8), 727–732.
- Kaula, W. M. (2000), *Theory of Satellite Geodesy: Applications of Satellites to Geodesy*, 36–38 pp., Dover, Mineola, N.Y., 160 p.
- Koch, C., U. Christensen, and R. Kallenbach (2008), Simultaneous determination of global topography, tidal Love number and libration amplitude of Mercury by laser altimetry, *Planetary and Space Science*, 56(9), 1226–1237.
- Koch, C., R. Kallenbach, and U. Christensen (2010), Mercury's global topography and tidal signal from laser altimetry by using a rectangular grid, *Planetary and Space Science*, 58(14–15), 2022–2030.
- Lin, S. Y., J. P. Muller, J. P. Mills, and P. E. Miller (2010), An assessment of surface matching for the automated co-registration of MOLA, HRSC and HiRISE DTMs, *Earth and Planetary Science Letters*, 294(3–4), 520–533.
- Margot, J. L. (2009), A Mercury orientation model including non-zero obliquity and librations, *Celestial Mechanics and Dynamical Astronomy*, 105(4), 329–336.
- Margot, J. L., S. J. Peale, R. F. Jurgens, M. A. Slade, and I. V. Holin (2007), Large longitude libration of Mercury reveals a molten core, *Science*, 316(5825), 710–714.
- Margot, J. L., et al. (2012), Mercury's moment of inertia from spin and gravity data, *Journal of Geophysical Research-Planets*, 117(E12), E00L09.
- Mazarico, E., A. Genova, S. Goossens, F. G. Lemoine, G. A. Neumann, M. T. Zuber, D. E. Smith, and S. C. Solomon (2014), The gravity field, orientation, and ephemeris of Mercury from MESSENGER observations after three years in orbit, *Journal of Geophysical Research-Planets*, 119(12), 2417–2436.
- Peale, S. J. (1976), Does Mercury have a molten core, *Nature*, 262(5571), 765–766.
- Peale, S. J. (1988), The rotational dynamics of mercury and the state of its core, in *Mercury*, edited by F. Vilas, C. R. Chapman, and M. S. Matthews, pp. 461–493, University of Arizona Press, Tucson, Ariz.
- Peale, S. J., M. Yseboodt, and J. L. Margot (2007), Long-period forcing of Mercury's libration in longitude, *Icarus*, 187(2), 365–373.
- Pfyffer, G., T. Van Hoolst, and V. Dehant (2011), Librations and obliquity of Mercury from the BepiColombo radio-science and camera experiments, *Planetary and Space Science*, 59(9), 848–861.
- Postolov, Y., A. Krupnik, and K. McIntosh (1999), Registration of airborne laser data to surfaces generated by photogrammetric means, in *Mapping Surface Structure and Topography by Airborne and Spaceborne Lasers*, vol. 32-3/W14, edited by B. M. Csatho, p. 5 pp., International Archives of the Photogrammetry, Remote Sensing and Spatial Information Societies.
- Preusker, F., J. Oberst, J. W. Head, T. R. Waters, M. S. Robinson, M. T. Zuber, and S. C. Solomon (2011), Stereo topographic models of Mercury after three MESSENGER flybys, *Planetary and Space Science*, 59(15), 1910–1917.
- Preusker, F., A. Stark, J. Oberst, K. J. Becker, M. E. Perry, and S. C. Solomon (2014), Topography of Mercury: A global model from MESSENGER orbital stereo mapping, *European Planetary Science Congress 2014, EPSC2014-709*.
- Rosat, S., P. Rosenblatt, A. Trinh, and V. Dehant (2008), Mars and Mercury rotation variations from altimetry crossover data: Feasibility study, *Journal of Geophysical Research-Planets*, 113(E12), E12,014.
- Santo, A. G., et al. (2001), The MESSENGER mission to Mercury: spacecraft and mission design, *Planetary and Space Science*, 49(14–15), 1481–1500.
- Smith, D. E., M. T. Zuber, X. Sun, G. A. Neumann, J. F. Cavanaugh, J. F. McGarry, and T. W. Zagwodzki (2006), Two-way laser link over interplanetary distance, *Science*, 311(5757), 53.
- Smith, D. E., et al. (2012), Gravity field and internal structure of Mercury from MESSENGER, *Science*, 336(6078), 214–217.

- Srinivasan, D. K., M. E. Perry, K. B. Fielhauer, D. E. Smith, and M. T. Zuber (2007), The radio frequency subsystem and radio science on the MESSENGER mission, *Space Science Reviews*, 131(1-4), 557–571.
- Stark, A., J. Oberst, and H. Hussmann (2015), Mercury’s resonant rotation from secular orbital elements, *Celestial Mechanics and Dynamical Astronomy*, 123(3), 263–277.
- Tarantola, A., and B. Valette (1982), Generalized nonlinear inverse problems solved using the least squares criterion, *Reviews of Geophysics*, 20(2), 219.
- Wu, B., J. Guo, H. Hu, Z. L. Li, and Y. Q. Chen (2013), Co-registration of lunar topographic models derived from Chang’E-1, SELENE, and LRO laser altimeter data based on a novel surface matching method, *Earth and Planetary Science Letters*, 364(0), 68–84.
- Wu, X., P. L. Bender, S. J. Peale, G. W. Rosborough, and M. A. Vincent (1997), Determination of Mercury’s 88 day libration and fluid core size from orbit, *Planetary and Space Science*, 45(1), 15–19.
- Yseboodt, M., and J. L. Margot (2006), Evolution of Mercury’s obliquity, *Icarus*, 181(2), 327–337.
- Yseboodt, M., J. L. Margot, and S. J. Peale (2010), Analytical model of the long-period forced longitude librations of Mercury, *Icarus*, 207(2), 536–544.
- Zuber, M. T., et al. (2008), Laser Altimeter observations from MESSENGER’s first Mercury flyby, *Science*, 321(5885), 77–79.
- Zuber, M. T., et al. (2012), Topography of the Northern Hemisphere of Mercury from MESSENGER Laser Altimetry, *Science*, 336(6078), 217–220.



# First MESSENGER Orbital Observations of Mercury's Librations

Alexander Stark<sup>a,b</sup>, Jürgen Oberst<sup>a,c</sup>, Frank Preusker<sup>a</sup>, Stanton J. Peale<sup>d</sup>, Jean-Luc Margot<sup>e,f</sup>, Roger J. Phillips<sup>g</sup>, Gregory A. Neumann<sup>h</sup>, David E. Smith<sup>i</sup>, Maria T. Zuber<sup>i</sup>, Sean C. Solomon<sup>j,k</sup>

<sup>a</sup> German Aerospace Center, Institute of Planetary Research, D-12489 Berlin, Germany, <sup>b</sup> Technische Universität Berlin, Institute of Geodesy and Geoinformation Science, D-10623 Berlin, Germany, <sup>c</sup> Moscow State University for Geodesy and Cartography, RU-105064 Moscow, Russia, <sup>d</sup> Department of Physics, University of California, Santa Barbara, CA 93106, USA, <sup>e</sup> Department of Earth, Planetary, and Space Sciences, University of California, Los Angeles, CA 90095, USA, <sup>f</sup> Department of Physics and Astronomy, University of California, Los Angeles, CA 90095, USA, <sup>g</sup> Southwest Research Institute, Boulder, CO 80302, USA, <sup>h</sup> NASA Goddard Space Flight Center, Greenbelt, Maryland, USA <sup>i</sup> Department of Earth, Atmospheric and Planetary Sciences, Massachusetts Institute of Technology, Cambridge, MA 02139, USA, <sup>j</sup> Lamont-Doherty Earth Observatory, Columbia University, Palisades, NY 10964, USA, <sup>k</sup> Department of Terrestrial Magnetism, Carnegie Institution of Washington, Washington, DC 20015, USA

The final publication is available at Wiley via  
<http://dx.doi.org/10.1002/2015GL065152>.

## Abstract

We have co-registered laser altimeter profiles from three years of MESSENGER orbital observations with stereo digital terrain models to infer the rotation parameters for the planet Mercury. In particular, we provide the first observations of Mercury's librations from orbit. We have also confirmed available estimates for the orientation of the spin axis and the mean rotation rate of the planet. We find a large libration amplitude of  $38.9 \pm 1.3$  arc seconds and an obliquity of the spin axis of  $2.029 \pm 0.085$  arc minutes, results confirming that Mercury possesses a liquid outer core. The mean rotation rate is observed to be  $(6.13851804 \pm 9.4 \times 10^{-7})^\circ / \text{day}$  (a spin period of  $58.6460768 \text{ days} \pm 0.78 \text{ s}$ ), significantly higher than the expected resonant rotation rate. As a possible explanation we suggest that Mercury is undergoing long-period librational motion, related to planetary perturbations of its orbit.



# 1 Introduction

Mercury, moving deep in the gravitational field of the Sun, exhibits a distinctive rotation state. Its rotation is locked in a 3:2 spin-orbit resonance. Both the spin axis and the orbit-plane normal precess around the instantaneous Laplace-plane normal with a period near 330,000 years. In addition, action of the tidal torque of the Sun on the asymmetric mass distribution of the planet forces a physical libration in longitude, i.e., a small oscillation about the mean rotation. Measurement of the rotational state of Mercury, in combination with gravity field data, allows a determination of the size and state of Mercury’s core ([Peale, 1972, 1988](#); [Margot et al., 2007, 2012](#); [Smith et al., 2012](#); [Hauck et al., 2013](#); [Rivoldini et al., 2009](#); [Smith et al., 2012](#); [Hauck et al., 2013](#); [Rivoldini and Van Hoolst, 2013](#); [Dumberry and Rivoldini, 2015](#)).

The first accurate observations of Mercury’s rotation ([Pettengill and Dyce, 1965](#)) demonstrated the distinctive resonance of the planet. On the basis of Mariner 10 images the rotation period was constrained to  $58.6461 \pm 0.005$  days ([Klaasen, 1976](#)). More recently, Earth-based radar measurements of Mercury’s obliquity and the amplitude of its forced libration ([Margot et al., 2007](#)) indicated that Mercury possesses a liquid core that is decoupled from the mantle on the 88-day timescale of the librations. However, the implications for the interior of Mercury from those radar observations were limited by uncertainties in the long-wavelength gravity field of the planet derived from Mariner 10 tracking observations. After the insertion of the MESSENGER spacecraft into orbit about Mercury in 2011, spacecraft Doppler and ranging measurements yielded precise estimates of Mercury’s gravity field, particularly the coefficients of the terms of low degree and order in a spherical harmonic expansion of that field ([Mazarico et al., 2014](#)).

In this paper, we make use of orbital image and laser altimeter data acquired by MESSENGER to take a fresh look at the rotational state of Mercury. In particular, we report on the first determination of Mercury’s librations from orbital observations. Our results validate those from Earth-based radar measurements by [Margot et al. \(2012\)](#). We also update Mercury’s spin axis orientation and rotation rate parameters. The estimation of Mercury’s obliquity and libration amplitude is performed using a novel approach ([Stark et al., 2015a](#)) by which we co-register laser altimeter profiles acquired over the three years of MESSENGER orbital operations to large-area topographic models derived from images by stereo photogrammetry.

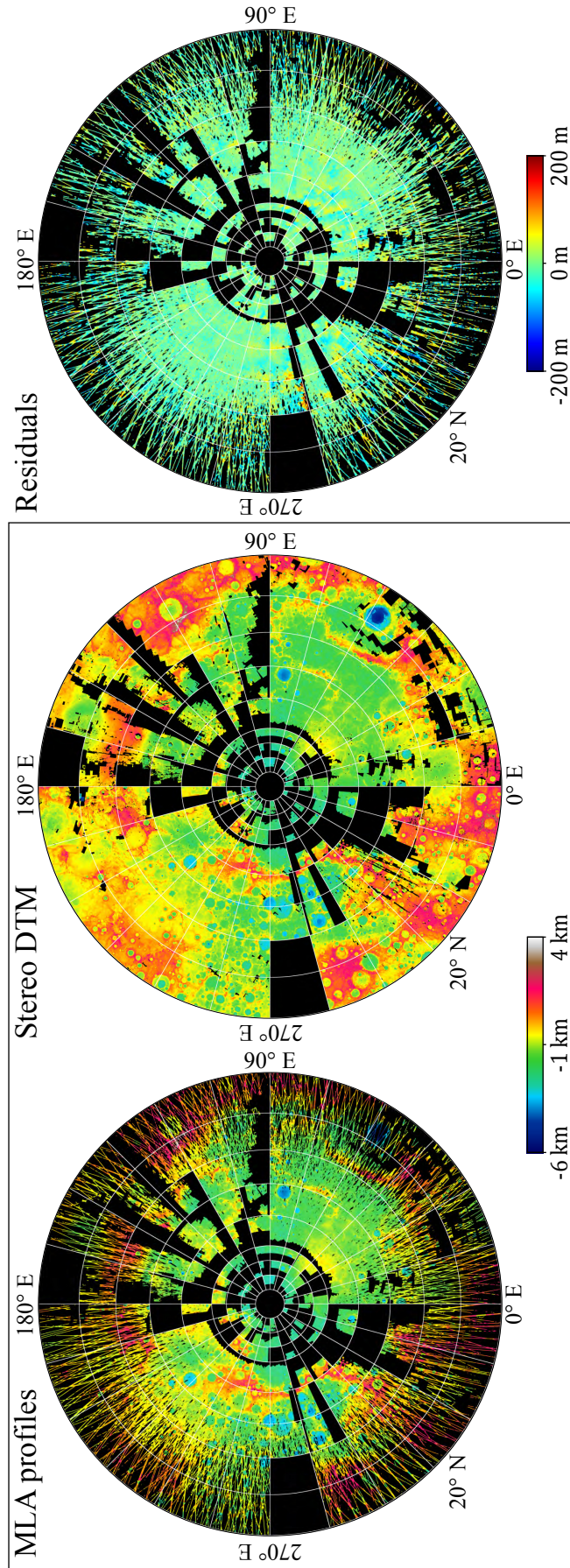


Figure 1: Left: MLA profiles used for measurement of rotational parameters. Middle: DTM tiles derived from stereo images by stereo photogrammetry. Each element of the grid corresponds to one DTM tile, for which separate offset and shift parameters are calculated. Gaps indicate lack of coverage by stereo DTMs. Right: Height residuals between MLA profiles and the stereo DTM tiles after co-registration. The mean value of the residuals is -1.2 m, and the standard deviation is 51.6 m. All maps are in stereographic projection centered at the north pole.

## 2 Data preparation

The Mercury Dual Imaging System (MDIS) ([Hawkins et al., 2007](#)) acquired more than 200,000 images during three years of observations, providing multiple coverage for nearly the entire surface at high resolution (better than 250 m/pixel). In contrast, data from the Mercury Laser Altimeter (MLA) ([Cavanaugh et al., 2007](#)) are largely confined to the northern hemisphere, as a result of limits on ranging distance and MESSENGER’s highly eccentric, near-polar orbit.

We computed digital terrain models (DTMs) from stereo images following established procedures ([Gwinner et al., 2010](#); [Preusker et al., 2011](#); [Oberst et al., 2014](#)) that included image correlation and least-squares block adjustment techniques. We combined at least three overlapping images to overcome uncertainties in spacecraft orbit, camera pointing direction, and calibration parameters, and consequently we obtained terrain models with very high internal robustness. Despite that geometric consistency, the stereo terrain models may have lateral and vertical offsets with respect to Mercury’s center of mass. These global offsets are caused by residual uncertainties in spacecraft position and attitude (including camera pointing for individual images), as well as intrinsic camera calibration parameters. We produced 165 individual gridded DTMs (all at a grid size of 222 m/pixel) that cover approximately 50% of the northern hemisphere (Figure 1) with an average height error of 60 m. There are gaps in the image coverage because several geometric constraints (e.g., image resolution, incidence angle of sunlight, and stereo angle) must be satisfied in order to assemble stereo images. The topography in each DTM is expressed as height above a reference sphere of radius 2440 km.

The laser profiles acquired by the MLA instrument are highly complementary to the stereo DTMs. We used three years of MLA observations (29 March 2011 to 31 March 2014), including 2325 laser profiles across the northern hemisphere of Mercury (Figure 1). The highest density of data is in the north polar area, where the altimeter profiles converge. The nominal ranging accuracy is on the order of 1 m ([Cavanaugh et al., 2007](#)) and increases with ranging distance and off-nadir pointing. The profiles were obtained continuously, except for approximately two weeks in each Mercury orbit cycle. During those two weeks the spacecraft periaapsis was over the dayside of Mercury, and the MLA was turned off to limit instrument temperature. At least two laser profiles per 24-h period (three profiles per day after the first year in orbit) were obtained, and observations covering more than 12 Mercury libration cycles (every  $\approx 88$  days) and 18 Mercury rotation cycles (every  $\approx 59$  days) are available for the analysis.

The comparison between laser altimeter observations acquired over a wide range of times and robust stereo DTMs with broad coverage and high spatial resolution is highly sensitive to rotational parameters for the planet.

### 3 Method

Our approach is to co-register the time-dependent spatially distributed network of laser altimeter profiles to the static topography of the stereo models. We compute the coordinates of the laser footprints in an inertial frame, i.e., the International Celestial Reference Frame (ICRF). The ICRF is approximately (to within 0.1 arc sec) the reference frame of the mean Earth equator and equinox of the J2000.0 epoch ([Archinal et al., 2011](#)). Coverage by laser profiles at a variety of rotation phases for Mercury allows us to determine all relevant parameters of the rotational model. We may thereby determine parameters that minimize height differences between laser altimeter measurements and the stereo DTMs. At the same time, we determine the static transformation parameters for each of the 165 DTMs, i.e., offsets, rotation angles, and scaling factors. We use a non-linear least-squares inversion to solve for the unknown parameters. Our observations are the radial height differences between the two data sets. The functional model  $g(\mathbf{p})$  is given by

$$g(\mathbf{p}) = r_{\text{DTM}}(\lambda(\mathbf{p}), \phi(\mathbf{p})) - |r_{\text{MLA}}(\mathbf{p})|, \quad (1)$$

where  $r_{\text{DTM}}(\lambda(\mathbf{p}), \phi(\mathbf{p}))$  is the height of the stereo DTM at the body-fixed latitude  $\lambda$  and longitude  $\phi$  of the laser footprint, and  $|r_{\text{MLA}}(\mathbf{p})|$  is the height of the corresponding laser footprint (see ([Stark et al., 2015a](#)) for more details). The parameter vector  $\mathbf{p}$  includes the set of rotation parameters and the DTM transformation parameters for each of the available 165 DTM tiles. In total, 1161 parameters are determined from the co-registration.

The unknowns in the rotational model include the orientation of the rotational axis with respect to the ICRF, the rotation rate, and the amplitude of the forced libration at an 88 day period. In addition, we introduce two parameters to correct the coordinates of Mercury’s center of mass within the planet’s equatorial plane, a step needed because of small uncertainties in the ephemeris of Mercury.

For practical reasons the reference epoch for the rotational parameters is set to a mid-term point of the MESSENGER orbital mission phase at MJD56353.5, or 2 March 2013, 12:00:00 barycentric dynamical time (TDB), 4809 days after the J2000.0 epoch. The precession of Mercury’s spin axis, not resolvable within the duration of the MESSENGER orbital mission phase, is held fixed at

$$\alpha_1 = -0.032808^\circ / \text{century} \text{ and } \delta_1 = -0.0048464^\circ / \text{century}$$



for the right ascension and declination of the spin axis, respectively (Margot, 2009; Stark et al., 2015b). Because Mercury is in a Cassini state (Peale, 1969), the spin axis is fixed in the orbit frame of reference and precesses at the same rate as the orbit. The precession of the spin axis is important, as during the three years of MESSENGER observations considered here the spin axis precessed by 1.8 arcsec. Given the precession rates, the spin axis orientation at the J2000.0 epoch can be calculated for comparison.

We adopt a model for the annual longitudinal librations  $\varphi_{\text{lib}}$ , which follows from the solution of the differential equation for tidal torque (Goldreich and Peale, 1966; Margot et al., 2007; Margot, 2009)

$$\varphi_{\text{lib}} = \sum_k g_{88} \sin(kn_0(t + t_0)), \quad (2)$$

where  $n_0 = 4.09233445^\circ / \text{day}$  is the mean motion of Mercury,  $t_0 = (4809 + 42.71182)$  days defines the libration phase at the reference epoch, and  $g_{(88/k)}$  denotes the amplitude of the  $k$ th harmonic of the libration. The amplitudes follow a recursive relation

$$g_{(88/(k+1))} = g_{(88/k)} \frac{G_{(201)}(k+1, e)}{G_{(201)}(k, e)} \quad (3)$$

where

$$G_{(201)}(k, e) = [G_{(201-k)}(e) - G_{(201+k)}(e)]/k^2 \text{ and } G_{(201 \pm k)}(e)$$

are Kaula’s eccentricity functions (Kaula, 2000), and  $e = 0.2056317$  is the orbital eccentricity of Mercury (Stark et al., 2015b). We limit the libration model to five harmonics, as we observed that the amplitudes of the higher-frequency terms (on the order of  $0.0001g_{88}$ ) are negligible.

In addition to the annual libration, there could be long-period librations with periods of several years, resulting from periodic perturbations to Mercury’s orbit by other planets or other mechanisms (see below). Although planetary perturbations to Mercury’s orbit are relatively small, their effect can be enhanced when their frequency is close to the free libration frequency of Mercury. However, considering the limited observational period of about 3 years, we are unable to track these long-period librations. Instead, we have searched for small deviations of Mercury’s spin rate from the resonant spin rate.

Other entries in the parameter vector  $\mathbf{p}$  describe adjustments to the DTM tiles, which include three rotation angles, three components of a translation vector, and a scaling factor (Stark et al., 2015a) for each DTM tile. The static transformations allow for the co-registration of the data sets in the spatial domain, whereas the adjustment of the rotational parameters ensures a proper alignment of the

laser altimetry footprints at their observation time. Note that because the small DTM tiles include regional topography the similarity transformation can be non-unique, but with the inclusion of all seven transformation parameters we allow maximal flexibility in the spatial co-registration. Because of the gaps in the stereo coverage mentioned above, only 50% of the full set of MLA measurements can be used in the estimation process. To obtain sub-pixel heights of the gridded DTMs at the coordinates of the laser footprints we perform a bi-linear interpolation of the DTM heights, whereby an area of  $3 \times 3$  pixels is approximated by an inclined plane. This step is not a limitation given that the "effective resolution" of the DTMs was determined to be as large as 3.8 km ([Stark et al., 2015a](#)).

In contrast to the stereo DTM data, which are coarse but fairly uniform in height precision, the MLA data, although more precise, suffer from individual uncertainties introduced by variations in ranging distance and occasional off-nadir pointing. We therefore introduced a weighting scheme for each individual observation (see [Stark et al. \(2015a\)](#)). In addition, we introduced a threshold to identify and remove extreme outliers (such as false detected laser pulses, or small-scale topographic features not seen in the stereo DTM); the threshold is estimated from the standard deviation of the residuals from the preceding iteration step.

We initiated the iterations with the rotational axis aligned with the orbit normal, the rotation rate set precisely to the resonant rotation rate of  $6.138506839^\circ$  per day, and the libration amplitude set to zero. The DTM transformation parameters were initialized under the assumption of perfect alignment of DTMs and MLA data.

Although the parameter estimation procedure yields formal uncertainties from the covariance matrix, we also derive more robust uncertainty estimations. We performed 100 Monte Carlo simulations of artificial MLA observations over the complete time span of three years treated here, and we derived uncertainties in the unknowns from their distribution in the simulation results. To account for the different resolution of the data sets we performed a synthesis of artificial laser altimeter measurements derived from the topography of the stereo DTMs. Each simulation was performed as follows. We started with the inertial spacecraft coordinates immediately before the transmission of the laser pulse. With the nominal information on spacecraft position and attitude, as well as laser pulse time of flight, we obtained the height information from the DTM at the laser footprint coordinates. Then, we added random errors to the nominal spacecraft position and attitude and generated high-resolution topography from the DTM heights at the nominal laser footprint locations. Thus, we obtained synthetic laser altimeter topography at perturbed laser footprint locations. The simulated observables were then co-registered and led to slightly different best-fit parameters. More de-

Table 1: Rotational parameters (observed) and corresponding interior structural parameters (derived) for Mercury.

Quantity	Value
<i>Observed rotational parameters</i>	
Annual libration amplitude	$38.9 \pm 1.3$ arc seconds
Mean rotation rate <sup>a</sup>	$(6.13851804 \pm 9.4 \times 10^{-7})^\circ/\text{day}$
Mean rotation period <sup>a</sup>	$58.6460768 \pm 0.0000090$ days
Right ascension of spin axis <sup>b</sup>	$281.00980 \pm 0.00088^\circ$
Declination of spin axis <sup>b</sup>	$61.4156 \pm 0.0016^\circ$
Obliquity of the spin axis	$2.029 \pm 0.085$ arc minutes
<i>Derived interior structure parameters<sup>c</sup></i>	
$(B - A)/C_m$	$(2.206 \pm 0.074) \times 10^{-4}$
$C/MR^2$	$0.346 \pm 0.011$
$C_m/C$	$0.421 \pm 0.021$
$C_m/MR^2$	$0.1458 \pm 0.0049$

Note: Gravitational parameters are from (Mazarico et al., 2014).

<sup>a</sup> Mean value during the time between 29 March 2011 and 31 March 2014.

<sup>b</sup> At J2000.0 with respect to the ICRF.

<sup>c</sup> Under the assumption that there is no or at most a small solid inner core.

tails on the simulation of topographic observables have been given by Stark et al. (2015a). The covariance of the unknown parameters  $\hat{\mathbf{C}}_p$  is finally given by

$$[\hat{\mathbf{C}}_p]_{ij} = \frac{1}{99} \sum_{k=1}^{100} (p_i^k - p_i^*)(p_j^k - p_j^*), \quad (4)$$

where  $p_i^*$  and  $p_i^k$  denote the  $i$ -th best-fit parameters from the actual data and from the  $k$ -th simulation of observations, respectively. The covariance matrix  $\hat{\mathbf{C}}_p$  is used to calculate uncertainties for all derived quantities, such as the moment of inertia values presented below.

## 4 Results

Following the inversion, we obtained a parameter set for the rotational model of Mercury (Table 1). We performed 15 iterations and stopped the calculation when

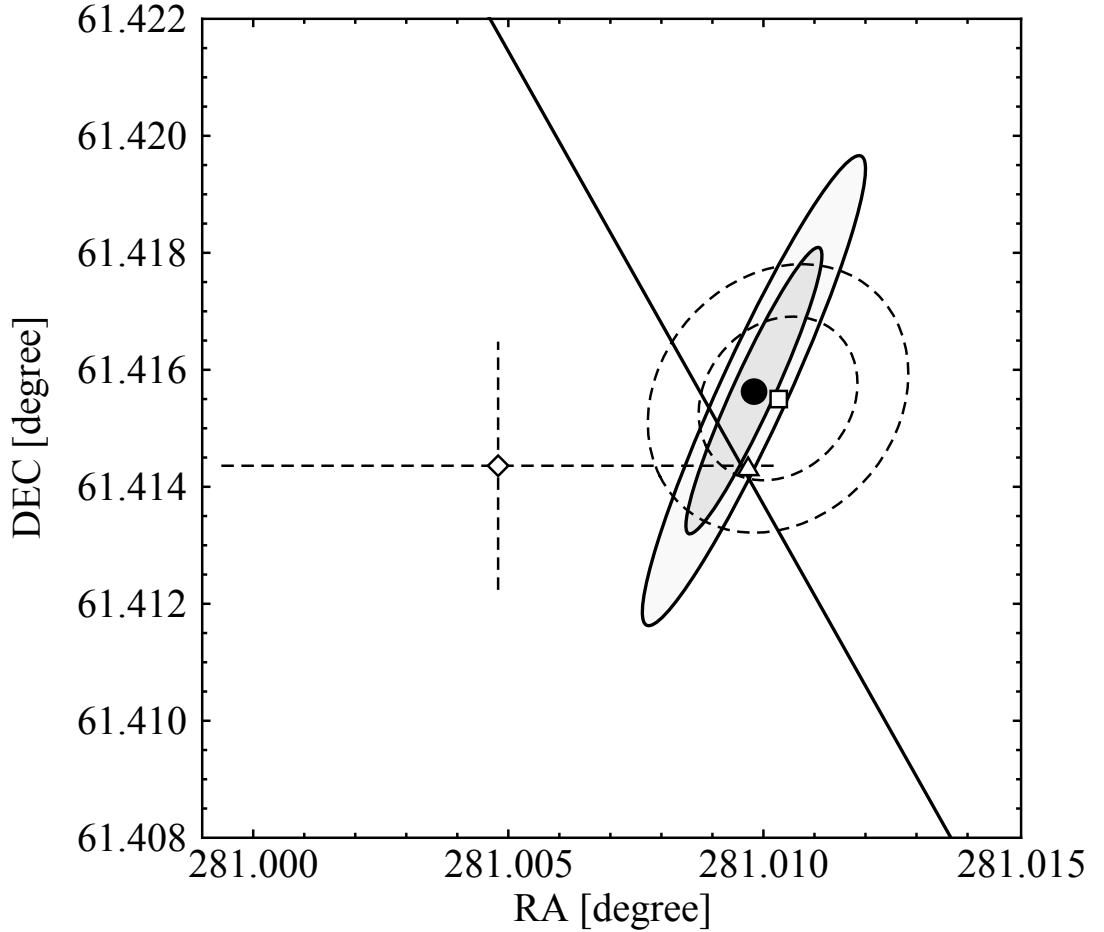


Figure 2: Right ascension (RA) and declination (DEC) of Mercury’s spin axis in the ICRF (filled circle) and one- and two-standard deviation uncertainties (shaded ellipses). The ground-based estimates of [Margot et al. \(2007\)](#) and [Margot et al. \(2012\)](#) are shown by the triangle and square, respectively; one- and two-standard-deviation errors are shown for the latter determination (dashed ellipses). The estimate inferred from the gravity field rotation ([Mazarico et al., 2014](#)) is denoted by a diamond, and the errors shown are at one standard deviation. The oblique line shows the predicted locations of Cassini state 1 from the values of [Stark et al. \(2015b\)](#), which are consistent with those of [Yseboodt and Margot \(2006\)](#). All spin axis orientations correspond to the J2000.0 epoch.



the improvement in the root mean squared residual was less than the centimeter level. We determined an annual libration amplitude of  $g_{88} = 38.9 \pm 1.3$  arc seconds, corresponding approximately to  $(460 \pm 15)$  m at the equator. These values are in agreement with the results from Earth-based radar observations ([Margot et al., 2012](#)), cited as  $(38.5 \pm 1.6)$  arc seconds. The absolute difference between the two values is 0.4 arc seconds, well within the respective one-standard-deviation errors. This high libration amplitude indicates that the rotation of Mercury’s crust and mantle is decoupled from that of the fluid core (see below).

The mean rotation rate of Mercury was determined as  $(6.13851804 \pm 9.4 \times 10^{-7})^\circ/\text{day}$ , higher by 14.72 arc seconds per year (or  $\approx 2$  ppm) than the expected resonant rate of  $6.1385068^\circ/\text{day}$  ([Stark et al., 2015b](#)). The estimated rotation rate corresponds to a rotation period of  $(58.6460768 \pm 0.0000090)$  days and is lower by 9.24 s than the resonant rotation period. The value obtained for the rotation rate is also significantly higher than the value of  $6.1385025^\circ/\text{day}$  currently adopted by the International Astronomical Union (IAU) ([Archinal et al., 2011](#)), but it is in agreement with the value estimated from Mariner 10 imaging of  $(6.13852 \pm 0.00052)^\circ/\text{day}$  ([Klaasen, 1976](#)). Recent estimates derived from the rotation of the gravity field of Mercury indicate a rotation rate of  $(6.13851079 \pm 1.2 \times 10^{-6})^\circ/\text{day}$  ([Mazarico et al., 2014](#)), also greater than the IAU value and the resonant rotation value but not in agreement with our estimate.

At the reference epoch of MJD56353.5 the orientation of the spin axis of Mercury’s mantle is obtained at  $\alpha_0(\text{MJD56353.5}) = 281.00548 \pm 0.00088^\circ$  in right ascension and  $\delta_0(\text{MJD56353.5}) = 61.4150 \pm 0.0016^\circ$  in declination with respect to the ICRF. With precession as discussed above, we find  $\alpha_0 = 281.00980 \pm 0.00088^\circ$  and  $\delta_0 = 61.4156 \pm 0.0016^\circ$  at the J2000.0 epoch (Figure 4). The obliquity of the spin axis with respect to the mean orbit normal ( $\alpha_0^{\text{OP}} = 280.98797^\circ$ ;  $\delta_0^{\text{OP}} = 61.4478^\circ$ ) is  $2.029 \pm 0.085$  arc minutes. We find that the spin axis orientation is slightly offset by 1.7 arc seconds, but well within the error bounds, from the precise Cassini state 1 position, known to within 0.3 arc seconds ([Stark et al., 2015b](#)). Again, all data are in excellent agreement with Earth-based radar results ([Margot et al., 2007, 2012](#)) (Figure 4). The absolute angular deviation from the most recent Earth-based result ([Margot et al., 2012](#)) is only 1 arc second. We observe somewhat larger values for the right ascension and declination of the spin axis than the gravity-based estimates of [Mazarico et al. \(2014\)](#). However, given the large error in the gravity-based estimate, further discussion of this difference in spin axis position is not warranted.

## 5 Implications and Discussion

The amplitude of the annual libration provides information on the coupling between the mantle and the core of the planet. For a molten outer core, the rotation of outer core and mantle will be nearly fully decoupled, and a large libration amplitude is possible. On the other hand, if the entire core is solid, the mantle and core will have a common rotation, in which case a smaller libration amplitude is expected. The observed large libration amplitude value of  $g_{88} = (38.9 \pm 1.3)$  arc seconds suggests at most limited coupling between mantle and outer core, and we can compute the corresponding asymmetry of the mass distribution within the planet from (Peale, 1972; Dumberry et al., 2013; Dumberry and Rivoldini, 2015)

$$\frac{B - A}{C_m} = \frac{2g_{88}}{3G_{(201)}(1, e)}(1 + \xi), \quad (5)$$

where  $A < B$  are the moments of inertia of the planet about the principal equatorial axes and  $C_m$  is the polar moment of inertia of the mantle and crust. The parameter  $\xi$  is a small correction that depends on the size of the solid inner core and interior density structure (Veasey and Dumberry, 2011; Van Hoolst et al., 2012; Dumberry et al., 2013; Dumberry and Rivoldini, 2015). The correction factor in equation (5) is below the uncertainty in the libration amplitude  $g_{88}$  even for a large inner core with a radius of about 1500 km (Van Hoolst et al., 2012; Dumberry et al., 2013). Hence, we assume that the equatorial asymmetry is due to the mantle alone, and we thereby neglect the coupling to a possible solid inner core, so  $\xi \approx 0$ . From our estimate of  $g_{88}$  we find a value of  $(B - A)/C_m = (2.206 \pm 0.074) \times 10^{-4}$ . This value provides an important constraint on the interior structure of the planet.

One possible explanation for the observation of a greater rotation rate than the expected resonant rotation value is that the planet is undergoing forced long-period librations, which modulate the mean rotation rate on timescales of several years (Peale et al., 2007; Yseboodt et al., 2010, 2013). The amplitude of the long-period libration is strongly related to the free libration frequency  $\omega_0$  of the planet (Yseboodt et al., 2010; Dumberry et al., 2013)

$$\omega_0 = n_0 \sqrt{3G_{(201)}(e) \frac{B - A}{C_m}}, \quad (6)$$

where  $G_{(201)}(e) = 7/2e + 123/16e^3 + O(e^5) \approx 0.654259$ . A large inner core can significantly change the free libration frequency given in equation (6). Here we discuss the case where Mercury has no or only a small solid inner core. The observed value of the mass-distribution asymmetry  $(B - A)/C_m = (2.206 \pm 0.074) \times 10^{-4}$  indicates that the free libration frequency of Mercury is  $0.5428 \pm 0.0091$  radians per year, corresponding to a period of  $11.58 \pm 0.19$  years, close to

the period of the orbital perturbations of Mercury’s orbit by Jupiter (11.864 years). With the analytical model of [Yseboodt et al. \(2010\)](#) and given a damping time of the free libration of about  $2 \times 10^5$  years ([Peale, 2005](#)), we searched for the free libration frequency that would be consistent with the observed rotation rate. We find that such high deviations from the resonant rate are possible only when they are resonantly enhanced, i.e., when the free libration frequency of Mercury is close to the frequency of the orbital perturbation. Because of its proximity to Jupiter’s orbital frequency, a free libration frequency of 0.536 radians per year (11.725 years) could lead to a sufficient enhancement of the effect of the small orbital perturbations of Mercury’s orbit to be in agreement with the observed mean rotation rate. The libration frequency inferred from long-period libration considerations (see supplementary online material for more details) corresponds to a mass-distribution asymmetry of  $(B - A)/C_m = 2.1498 \times 10^{-4}$ . Note that this value is consistent with our estimate from the annual libration amplitude  $g_{88}$  and the estimate by [Margot et al. \(2012\)](#) to within the one-standard-deviation uncertainty. In addition to forced longitudinal librations, free librations with large amplitudes are also theoretically possible under the condition of small internal dissipation or recent excitation. This discussion, of course, was of only one possible explanation for an increased rotation rate. Other mechanisms such as contributions from the solid inner core ([Dumberry, 2011](#); [Van Hoolst et al., 2012](#); [Dumberry et al., 2013](#); [Yseboodt et al., 2013](#)) or turbulent convection in the fluid core ([Koning and Dumberry, 2013](#)) can also affect the rotation rate.

[Peale et al. \(2014\)](#) considered several coupling mechanisms between the core and the mantle, any of which could lead to a mantle spin orientation that lags the precise Cassini state 1. Further, the small offset from the precise Cassini state 1 may represent the signature of a free precession. Nonetheless, the parameters of Cassini state 1 fall within the uncertainties in our estimate of the spin axis orientation. Further work is needed to understand the interplay of different torques acting on the mantle and the core, as well as the Cassini state 1 position (see ([Peale et al., 2015](#)) for a discussion of the consequences of a solid inner core on Mercury’s spin axis orientation).

From the observed obliquity of  $2.029 \pm 0.085$  arc minutes we can compute the normalized polar moment of inertia of the planet  $C/MR^2$ , where  $M$  is the mass of the planet and  $R$  its mean radius. We use equation (4) of [Peale \(1981\)](#) and  $\mu \sin \iota = 2.8645 \times 10^{-6}$  / year and  $\mu \cos \iota = 18.9 \times 10^{-6}$  / year ([Stark et al., 2015b](#)), where  $\mu$  is the precession rate of the mean orbital plane and  $\iota$  is the angle between the orbital plane and the Laplace plane. Further, we use the most recent estimates for the gravitational coefficients  $J_2 = (5.03216 \pm 0.00093) \times 10^{-6}$  and  $C_{22} = (0.80389 \pm 0.00019) \times 10^{-6}$  ([Mazarico et al., 2014](#)). We obtain a polar moment of inertia of the planet of  $C/MR^2 = 0.346 \pm 0.011$ .

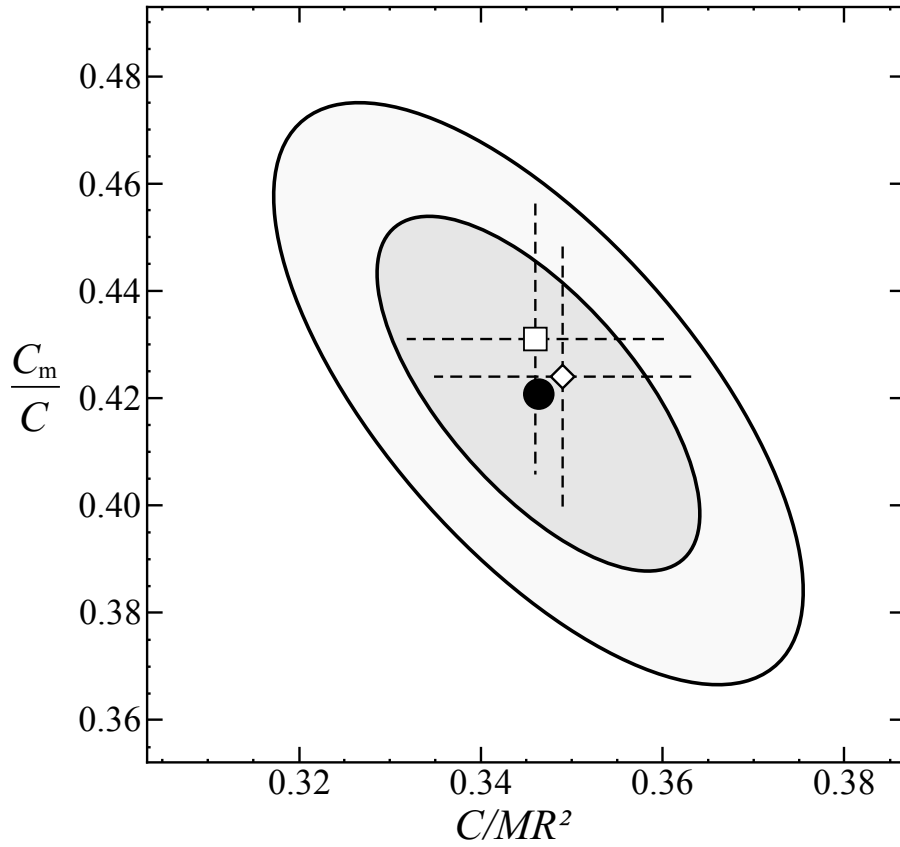


Figure 3: Mercury’s normalized polar moment of inertia  $C/MR^2$  and the fractional moment of inertia of the mantle and crust  $C_m/C$  as inferred from measured values for libration amplitude and obliquity (filled circle). The ellipses denote one- and two-standard-deviation uncertainties. The square and the diamond with dashed one-standard deviation uncertainties show the estimates of [Margot et al. \(2012\)](#) and [Mazarico et al. \(2014\)](#), respectively.

From the identity relation ([Peale, 1972](#); [Margot et al., 2012](#))

$$\frac{C_m}{C} = 4C_{22} \frac{MR^2}{C} \frac{C_m}{B - A}, \quad (7)$$

and our value for  $C/MR^2$  and  $(B - A)/C_m$ , we can compute the ratio  $C_m/C$  between the polar moment of inertia of the outer rigid shell  $C_m$  and that of the entire planet  $C$ . We find a value  $C_m/C = 0.421 \pm 0.021$  and consequently  $C_m/MR^2 = 0.1458 \pm 0.0049$  (Figure 5). The covariance between  $C/MR^2$  and  $C_m/C$  is  $-8.04 \times 10^{-5}$ . These results are again in very good agreement with those derived from Earth-based estimates of obliquity and libration amplitude by ([Margot et al., 2012](#)) and the gravity field of [Mazarico et al. \(2014\)](#).

The derived values for the moment of inertia form first-order constraints for the interior structure of Mercury. Given the total mass and shape of Mercury ([Perry et al., 2015](#)) one can constrain the densities of the core and the mantle, as

well as the location of the core-mantle boundary. Models for the interior structure of Mercury treat distinct crustal and mantle layers, the possibility of compositional layering in the mantle, the ellipticity of layer boundaries, and the effects of a possible solid inner core ([Smith et al., 2012](#); [Hauck et al., 2013](#); [Rivoldini and Van Hoolst, 2013](#); [Dumberry and Rivoldini, 2015](#)). The tidal Love number  $k_2$ , recently determined from MESSENGER’s radio science data ([Mazarico et al., 2014](#)), can provide an additional constraint on the structure and rheology of the planetary interior ([Padovan et al., 2014](#)).

For our analysis we used only three years of MLA observations and a small fraction of processed images. Expanding the data sets and elaborating the co-registration method ([Stark et al., 2015a](#)) by the use of crossover points on laser profiles are warranted in future applications of the methods applied here. Use of crossovers may provide additional constraints, which could further reduce the uncertainties in the rotational parameters. Our estimates of the uncertainties in the rotational parameters are based on a pessimistic scenario with a relatively poor knowledge of the position and attitude of the spacecraft and its alignment to MLA. Nonetheless, because of the combination of data from varying observation conditions in our analysis, e.g., variations in the distance of MESSENGER to Mercury’s surface from 200 km to 1790 km, we expect that the estimation of rotational parameters presented here is robust.

## 6 Conclusion

With laser altimetry and imaging data from the MESSENGER spacecraft we provide the first orbital measurement of the amplitude of the annual libration of Mercury. Further, we obtain values for the mean rotation rate and the orientation of the spin axis. The results are in excellent agreement with existing estimates from ground-based radar observations ([Margot et al., 2007, 2012](#)) and measurements of the rotation of the gravity field ([Mazarico et al., 2014](#)). Considering that the MESSENGER spacecraft operated for more than an additional year beyond the data treated in this paper, further refinement of Mercury’s rotational parameters can be expected from future analysis with the full set of orbital observations.

## Supplementary Material

### Introduction

We provide further details here on the interpretation of the measured rotation rate of Mercury. We also give a rotation model with long-period libration components.

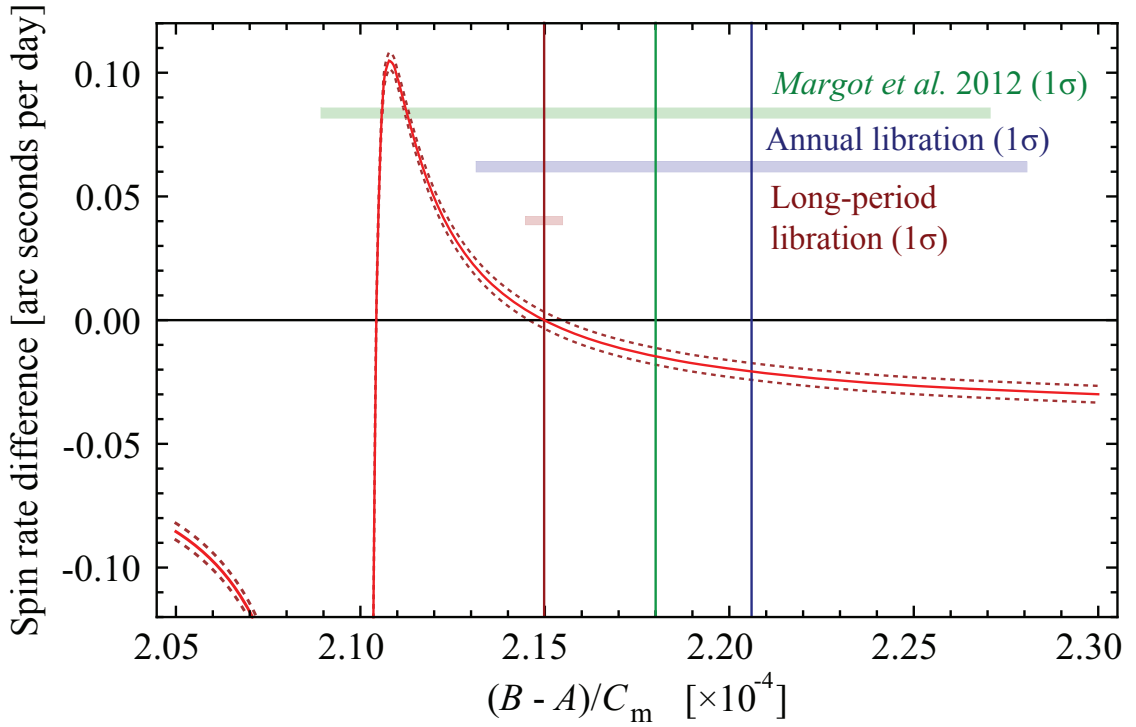


Figure 4: Plot of equation (12) (red line) as a function of  $(B - A)/C_m$ . The uncertainties in the measured spin rate  $\phi_1$  are denoted by dashed red lines. Shown, in addition, are the  $(B - A)/C_m$  values from the amplitude of the annual libration (blue vertical line), from *Margot et al. (2012)* (green vertical line), and from the long-period libration (red vertical line) and their corresponding uncertainties (one standard deviation, horizontal bands).

### Text S1

In order to obtain a model-independent estimate of the spin of Mercury we considered only a deviation of the spin rate from the resonant spin rate value. In particular, the rotation angle  $\phi(t)$  around the spin axis is modelled as

$$\phi(t) = \phi_0^* + \phi_1 t + \phi_{\text{lib}}(t), \quad (8)$$

where  $\phi_0^*$  is the effective prime meridian constant,  $\phi_1$  the mean spin rate during the period of observations, and  $\phi_{\text{lib}}$  the annual libration model given by equation (2). We can consider a long-period libration model, which can treat the deviation of the measured spin rate  $\phi_1$  from the resonant spin rate  $\phi_1^{(3/2)}$  by means of the simple analytical model given by *Yseboodt et al. (2010)*

$$\phi(t) = \phi_0 + \phi_1^{(3/2)} t + \phi_{\text{lib}}(t) + \phi_{\text{long-lib}}(t). \quad (9)$$

The long-period libration term is given by

$$\phi_{\text{long-lib}}(t) = \sum_{i=1}^5 \psi_i \cos(w_i t + \varphi_{\psi_i}), \quad (10)$$

where  $w_i$  is the frequency,  $\psi_i$  the amplitude, and  $\varphi_{\psi_i}$  the amplitude-dependent phase angle of the  $i$ -th long-period libration component. The amplitude  $\psi_i$  is a function of the free libration frequency (see [Yseboodt et al. \(2010\)](#) for more details). The sum is truncated to five forcing terms associated with perturbations of Mercury’s orbit by Jupiter, Venus, Saturn, and Earth. To establish the comparison with our rotation model we calculate a Taylor series of  $\phi_{\text{long-lib}}(t)$  at the reference epoch  $t_0 = 4809$  days (MJD56353.5)

$$\phi_{\text{long-lib}}(t) = \sum_{j=0}^{\infty} \left. \frac{\partial^j \phi_{\text{long-lib}}(t)}{\partial t^j} \right|_{t=t_0} (t - t_0)^j. \quad (11)$$

With this expansion we perform the comparison of terms in equations 8 and 9, which are linear in  $t$ , and we obtain

$$\phi_1 = \phi_1^{(3/2)} - \sum_{i=1}^5 \psi_i w_i \sin(w_i t + \varphi_{\psi_i}). \quad (12)$$

As the amplitudes  $\psi_i$  are functions of  $(B - A)/C_m$ , the roots of equation 12 can be determined with the measured value  $\phi_1 = (6.13851804 \pm 9.4 \times 10^{-7})^\circ / \text{day}$  and the resonant rotation rate  $\phi_1^{(3/2)} = 6.138506839^\circ / \text{day}$  ([Stark et al., 2015b](#)). We can identify two roots of equation (12) in the vicinity of the measured annual libration value of  $(B - A)/C_m = 2.206 \times 10^{-4}$  (Figure 4). The first root at  $2.104 \times 10^{-4}$  can be discarded, as it corresponds to a free libration frequency almost equal to the perturbation frequency by Jupiter. This value corresponds to a high amplitude for the long-period libration, which should be observable by Earth-based measurements ([Margot et al., 2012](#)). The second root of equation 12 corresponds to  $(B - A)/C_m = (2.1498 \pm 0.0045) \times 10^{-4}$ , where the error estimation is derived from the error in the spin rate  $\phi_1$ . This value is in agreement with the estimate of the annual libration amplitude and the measurements of [Margot et al. \(2012\)](#). Moreover, the existence of such a long-period libration amplitude is fully consistent with the instantaneous spin-rate measurement of [Margot et al. \(2012\)](#) within the given accuracy (Figure 5). A rotation model that includes both



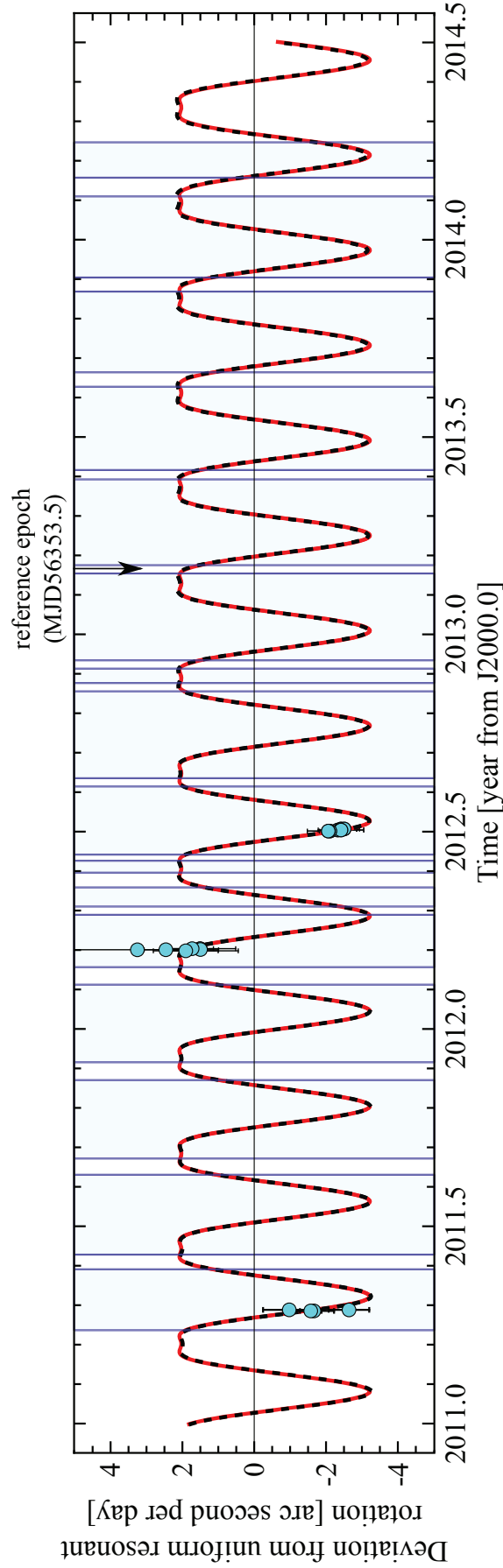


Figure 5: Libration model as given by equation (13) (red line) and libration model without long-period librations (black dashed line). The measurements by *Margot et al. (2012)* are in agreement with both models within their levels of uncertainty (cyan disks; only the measurements overlapping the three years of our study are shown). The periods of MLA observations are given by blue vertical bands, and the reference epoch used in this study is indicated by the black arrow.



short-period and long-period librations can be given as (the annual libration harmonics are truncated at the 0.5-arc-second level)

$$\begin{aligned}
 \phi(t) = & 329.6268^\circ + 6.138506839^\circ t / \text{day} \\
 & + 0.01080^\circ \sin(174.7911^\circ + 4.092334^\circ t / \text{day}) \\
 & - 0.00114^\circ \sin(349.5821^\circ + 8.184669^\circ t / \text{day}) \\
 & + 0.01697^\circ \cos(168.2910^\circ + 0.083095^\circ t / \text{day}) \\
 & + 0.00107^\circ \cos(92.6366^\circ - 0.174041^\circ t / \text{day}) \\
 & + 0.00041^\circ \cos(175.9814^\circ - 0.166163^\circ t / \text{day}) \\
 & + 0.00040^\circ \cos(35.4939^\circ + 0.066952^\circ t / \text{day}) \\
 & + 0.00017^\circ \cos(152.4469^\circ + 0.149917^\circ t / \text{day}).
 \end{aligned} \tag{13}$$

Note that the given prime meridian constant  $\phi_0 = 329.6268^\circ$  was simply adapted to the updated rotation rate value from the current value of  $329.5469^\circ$  (*Archinal et al., 2011*). The actual value will be subject to change, as it is related to the location of the impact crater Hun Kal.

## Acknowledgments

This research was funded by a grant from the German Research Foundation (OB124/11-1). J. Oberst gratefully acknowledges being hosted by MIIGAiK and supported by the Russian Science Foundation under project 14-22-00197. The MESSENGER mission is supported by the NASA Discovery Program under contract NAS5-97271 to The Johns Hopkins University Applied Physics Laboratory and NASW-00002 to the Carnegie Institution of Washington. We acknowledge the contributions of the MESSENGER spacecraft team and MLA and MDIS instrument teams in acquiring the observations used herein. MESSENGER data are available from the Planetary Data System (<https://pds.jpl.nasa.gov>). We thank Hauke Hussmann and Marie Yseboodt for helpful comments and discussions. Reviews by Mathieu Dumberry and an anonymous reviewer substantially improved this paper.

Reprinted from *First MESSENGER orbital observations of Mercury’s librations*, Stark, A., Oberst, J., Preusker, F., Peale, S.J., Margot, J.-L., Phillips, R.J., Neumann, G.A., Smith, D.E., Zuber, M.T., Solomon, S.C., *Geophysical Research Letters*, 42, 7881-7889, Copyright (2015), with permission from Wiley.

## References

- Archinal, B. A., et al. (2011), Report of the IAU Working Group on Cartographic Coordinates and Rotational Elements: 2009, *Celestial Mechanics and Dynamical Astronomy*, 109(2), 101–135.
- Cavanaugh, J. F., et al. (2007), The Mercury Laser Altimeter instrument for the MESSENGER mission, *Space Science Reviews*, 131(1-4), 451–479.
- Dumberry, M. (2011), The free librations of Mercury and the size of its inner core, *Geophysical Research Letters*, 38(16), L16,202.
- Dumberry, M., and A. Rivoldini (2015), Mercury’s inner core size and core-crystallization regime, *Icarus*, 248(0), 254–268.
- Dumberry, M., A. Rivoldini, T. Van Hoolst, and M. Yseboodt (2013), The role of Mercury’s core density structure on its longitudinal librations, *Icarus*, 225(1), 62–74.
- Goldreich, P., and S. Peale (1966), Spin-orbit coupling in the solar system, *The Astronomical Journal*, 71, 425.
- Gwinner, K., et al. (2010), Topography of Mars from global mapping by HRSC high-resolution digital terrain models and orthoimages: Characteristics and performance, *Earth and Planetary Science Letters*, 294(3-4), 506–519.
- Hauck, S. A., II, et al. (2013), The curious case of Mercury’s internal structure, *Journal of Geophysical Research: Planets*, 118(6), 1204–1220.
- Hawkins, S. E., III, et al. (2007), The Mercury Dual Imaging System on the MESSENGER spacecraft, *Space Science Reviews*, 131(1-4), 247–338.
- Kaula, W. M. (2000), *Theory of Satellite Geodesy: Applications of Satellites to Geodesy*, 36-38 pp., Dover, Mineola, N.Y., 160 p.
- Klaasen, K. P. (1976), Mercury’s rotation axis and period, *Icarus*, 28(4), 469 – 478.
- Koning, A., and M. Dumberry (2013), Internal forcing of Mercury’s long period free librations, *Icarus*, 223(1), 40–47.
- Margot, J. L. (2009), A Mercury orientation model including non-zero obliquity and librations, *Celestial Mechanics and Dynamical Astronomy*, 105(4), 329–336.
- Margot, J. L., S. J. Peale, R. F. Jurgens, M. A. Slade, and I. V. Holin (2007), Large longitude libration of Mercury reveals a molten core, *Science*, 316(5825), 710–714.
- Margot, J. L., et al. (2012), Mercury’s moment of inertia from spin and gravity data, *Journal of Geophysical Research-Planets*, 117(E12), E00L09.
- Mazarico, E., A. Genova, S. Goossens, F. G. Lemoine, G. A. Neumann, M. T. Zuber, D. E. Smith, and S. C. Solomon (2014), The gravity field, orientation, and ephemeris of Mercury from MESSENGER observations after three years in orbit, *Journal of Geophysical Research-Planets*, 119(12), 2417–2436.
- Oberst, J., K. Gwinner, and F. Preusker (2014), Exploration and analysis of planetary shape and topography using stereophotogrammetry, in *Encyclopedia of the Solar System*, edited by T. Spohn, D. Breuer, and T. V. Johnson, 3rd ed., pp. 1223–1233, Elsevier, Boston.
- Padovan, S., J. L. Margot, S. A. Hauck, W. B. Moore, and S. C. Solomon (2014), The tides of Mercury and possible implications for its interior structure, *Journal of Geophysical Research-Planets*, 119(4), 850–866.
- Peale, S. J. (1969), Generalized Cassini’s laws, *Astronomical Journal*, 74, 483.
- Peale, S. J. (1972), Determination of parameters related to the interior of Mercury, *Icarus*, 17(1), 168–173.
- Peale, S. J. (1981), Measurement accuracies required for the determination of a Mercurian liquid core, *Icarus*, 48(1), 143–145.
- Peale, S. J. (1988), The rotational dynamics of mercury and the state of its core, in *Mercury*, edited by F. Vilas, C. R. Chapman, and M. S. Matthews, pp. 461–493, University of Arizona Press, Tucson, Ariz.

- Peale, S. J. (2005), The free precession and libration of Mercury, *Icarus*, 178(1), 4–18.
- Peale, S. J., M. Yseboodt, and J. L. Margot (2007), Long-period forcing of Mercury’s libration in longitude, *Icarus*, 187(2), 365–373.
- Peale, S. J., J. L. Margot, S. A. Hauck, II, and S. C. Solomon (2014), Effect of core-mantle and tidal torques on Mercury’s spin axis orientation, *Icarus*, 231(0), 206–220.
- Peale, S. J., J.-L. Margot, S. A. Hauck, II, and S. C. Solomon (2015), Consequences of a solid inner core on Mercury’s spin configuration, *Icarus*, 264, 443–455.
- Perry, M. E., et al. (2015), The low-degree shape of Mercury, *Geophysical Research Letters*, 42(17), 6951–6958.
- Pettengill, G. H., and R. B. Dyce (1965), A radar determination of the rotation of the planet Mercury, *Nature*, 206, 1240.
- Preusker, F., J. Oberst, J. W. Head, T. R. Waters, M. S. Robinson, M. T. Zuber, and S. C. Solomon (2011), Stereo topographic models of Mercury after three MESSENGER flybys, *Planetary and Space Science*, 59(15), 1910–1917.
- Rivoldini, A., and T. Van Hoolst (2013), The interior structure of Mercury constrained by the low-degree gravity field and the rotation of Mercury, *Earth and Planetary Science Letters*, 377(0), 62–72.
- Rivoldini, A., T. Van Hoolst, and O. Verhoeven (2009), The interior structure of Mercury and its core sulfur content, *Icarus*, 201(1), 12–30.
- Smith, D. E., et al. (2012), Gravity field and internal structure of Mercury from MESSENGER, *Science*, 336(6078), 214–217.
- Stark, A., J. Oberst, F. Preusker, K. Gwinner, S. J. Peale, J.-L. Margot, R. J. Phillips, M. T. Zuber, and S. C. Solomon (2015a), Mercury’s rotational parameters from MESSENGER image and laser altimeter data: A feasibility study, *Planetary and Space Science*, 117, 64–72.
- Stark, A., J. Oberst, and H. Hussmann (2015b), Mercury’s resonant rotation from secular orbital elements, *Celestial Mechanics and Dynamical Astronomy*, 123(3), 263–277.
- Van Hoolst, T., A. Rivoldini, R.-M. Baland, and M. Yseboodt (2012), The effect of tides and an inner core on the forced longitudinal libration of Mercury, *Earth and Planetary Science Letters*, 333–334, 83 – 90.
- Veasey, M., and M. Dumberry (2011), The influence of Mercury’s inner core on its physical libration, *Icarus*, 214(1), 265–274.
- Yseboodt, M., and J. L. Margot (2006), Evolution of Mercury’s obliquity, *Icarus*, 181(2), 327–337.
- Yseboodt, M., J. L. Margot, and S. J. Peale (2010), Analytical model of the long-period forced longitude librations of Mercury, *Icarus*, 207(2), 536–544.
- Yseboodt, M., A. Rivoldini, T. Van Hoolst, and M. Dumberry (2013), Influence of an inner core on the long-period forced librations of Mercury, *Icarus*, 226(1), 41–51.

## 6 Discussion and Outlook

In this chapter the results of the research papers are discussed and further research directions are highlighted. Implications on Mercury's interior are derived based on a spherical two-layer model. The chapter ends with an outlook to future exploration of Mercury.

### 6.1 Resonant rotation model of Mercury

In the case of Mercury, with its 3:2 spin-orbit resonance, predictions about the rotational state can be made on the basis of the planet's ephemeris. The orbit of the planet is exposed to perturbations by the other planets as well as relativistic effects. Before the MESSENGER spacecraft got in orbit about the planet, the ephemeris of Mercury was the most uncertain among the terrestrial planets. In the derivation of the resonant rotation model an ephemeris based on two years of MESSENGER radio tracking was used and improvements to the orbital motion of Mercury were incorporated. However, the long-term orbital characteristics like secular variations, which were used for the derivation of the resonant rotation model, were not significantly changed by the MESSENGER data. A possible explanation for this is the fact, that the long-term behavior of the orbit is more constrained by observations over a larger temporal distribution. Moreover, the Solar System ephemerides are built through combination of different types of observations with large heterogeneity in their accuracy. Therefore it is difficult to provide an uncertainty estimation for the long-term evolution of the orbit. An additional problem arises from the available time coverage of the Mercury ephemeris. On the one hand the extrapolation error done by the forward integration of the ephemeris increases with time. While on the other hand relevant changes of the orbit happen on larger time scales than covered by documented observation in past decades. The approach chosen in Paper I was to use the fluctuations of the osculating orbital elements for a rough accuracy estimation. This approach is more conservative than a least-squares based error estimation (e.g., [Noyelles and D'Hoedt \(2012\)](#)). Nonetheless, the derived uncertainties for the secular orbital elements are much smaller than current observation accuracies for the rotational parameters.

One possible extension of the work presented in the research paper is to study in more detail the forcing terms for the longitudinal librations ([Yseboodt et al., 2010](#)). Latitudinal librations ([Dufey et al., 2009](#)) and the tidal potential ([Van Hoolst and Jacobs, 2003](#)) can be also updated using the most recent ephemeris data.

## 6.2 Method for measurement of rotational parameters

The method presented in Paper II for the measurement of rotational parameters has great potential for further improvements. The mathematical description for the global offsets of the DTM is based on a simple similarity transformation. This is motivated by the high internal geometric accuracy of the DTM, where several images control one object point and the DTM pixel is formed by several object points. However, in cases of bad stereo conditions, illumination, or coverage, the DTM may show high-order deformations, like stretching or bending. This may also be the case when the images, that control one DTM pixel, are obtained under similar conditions and that way are affected by the same systematic effect. The accuracy of the DTM may also degrade due to surface characteristics. Areas like the volcanic plains at high northern latitudes of Mercury are very smooth, with few craters and other types of relief. The cross-correlation of images of such areas provide less tight constraints on the object points and the DTM may show artifacts. To overcome these issues one can solve for additional parameters of a high-order deformation in the co-registration process. However, given the diverse peculiarity of such deformations an efficient parametrization is challenging. As the deformations of the DTM are over long-wavelengths (typically more than thousand kilometers) an other approach is to apply the similarity transformation to regional sets with a much smaller extent than the deformation. Such a solution was implemented in Paper III.

An other point for improvements of the method is the treatment of the laser profiles. The cross-over observable, i.e. the height difference at the intersection point of two crossing laser profiles, can provide additional constraints for the inversion of the rotational and DTM transformation parameters. The cross-overs establish a connection of laser profiles from several epochs and can be also used for inversion of the tidal amplitude ([Steinbrügge et al., 2015](#)). In application to MESSENGER altimeter data the cross-over observables are deteriorated by the large lateral spacing between consecutive laser footprints. The interpolation error, i.e the error one makes in the determination of the height between two laser footprints, may cause the cross-over observable to have a large uncertainty and reduces its benefit.

The laser profiles are strongly affected by the uncertainty in the knowledge of the position and attitude of the spacecraft as well as the alignment of the instrument to the spacecraft reference frame. The co-registration method provides capabilities for improvements to this knowledge. The uncertainty in the orbit and attitude reconstruction typically exceeds the uncertainty in the co-registration of an individual laser profile to the stereo DTM (see [Gläser et al., 2013](#)). Thus, orbit and attitude information of the spacecraft may be corrected by combining image and laser altimeter data.

It should be also noted that the method for measurement of rotational parameters described in Paper II is applicable to other Solar System objects, where image and laser altimeter data are available or will be available in the future. Earth's moon, for instance, was observed by several spacecraft with laser altimeters ([Ping et al., 2009](#); [Smith et al., 2010](#); [Araki et al., 2013](#)). A high-resolution topography reconstructed from stereo images is as well available ([Scholten et al., 2012](#)). This is also the case for Mars, which was observed by the Mars Orbiter Laser Altimeter (MOLA) and stereo images were obtained, e.g. by the cameras on board the MarsExpress spacecraft ([Gwinner et al., 2010, 2015](#)).

### 6.3 Rotational parameters of Mercury

In the third research paper the results for the rotational parameters of Mercury from three years of MESSENGER observations were given. The orientation of the rotation axis with respect to the inertial reference frame, the amplitude of the annual librations, and the mean rotation rate over three years could be obtained. The uncertainty estimation for these parameters was derived using forward simulation of laser altimeter data with typical uncertainties for spacecraft position and attitude as well as the alignment of the instrument to the reference frame of the spacecraft.

At the time of the analysis in Paper III not all MESSENGER data, which is now available, were used. Additional laser altimeter profiles were collected by MLA during the fourth year in orbit. This corresponds to an increase of about 33% in the data used in Paper III. A more dramatic increase in the data available for analysis, however, can be gained from additional coverage by the stereo DTMs. In Paper III only 50% of the available MLA data could be used due to large gaps in the coverage by the stereo DTMs. When all images, which are suitable for a stereo photogrammetric analysis, are processed the global coverage is expected to be almost free of gaps and only with small gaps in areas near the poles with permanent shadow. Consequently one can expect a remarkable increase in the accuracy of rotational parameter measurement by processing the full data available from MESSENGER.

The results of the paper confirmed previous Earth-based measurements of the orientation of the rotation axis and the libration amplitude of Mercury ([Margot et al., 2007, 2012](#)). However, the obtained value for the mean rotation rate of Mercury disagrees with the value adopted by the Working Group on Cartographic Coordinates and Rotational Elements of the Planets and Satellites (WGCCRE) of the International Astronomical Union (IAU, [Archinal et al., 2011](#)). It also disagrees with the updated resonant rotation value obtained from ephemeris (Paper I). While the former disagreement can be attributed to the outdated value dating

back to the 1980s ([Davies et al., 1980](#)), the latter disagreement can have an actual physical reasoning. This can be a long-period libration cycle, as discussed in Paper III, but other mechanisms are also possible, specifically when Mercury has a large solid inner core.

Further, the difference between the measured rotation rate value and the one obtained from rotation of the gravity field is of particular interest ([Mazarico et al., 2014](#)). This could hint at a differential rotation of the core and mantle. Since the core forms about 75% of the mass of the planet, the measured value from gravity field rotation could be a mixture of the rotation of core and mantle. The closeness of the gravity based rotation rate value to the resonant rotation rate becomes reasonable, as the core would not participate in the cycle of the long-period librations.

## 6.4 Implications on Mercury's interior

Based on the values for the polar moment of inertia of the crust plus mantle  $C_m$  and the polar moment of inertia of the planet  $C$  obtained in Paper III, one can construct spherical two-layer models of Mercury's interior with uniform densities. For this simple case the ratio  $\sigma_c = R_c/R$  between the radius of the core  $R_c$  and that of the planet  $R$  is given by an implicit equation

$$\frac{5}{2} \frac{C}{MR^2} \left[ 1 - \frac{C_m}{C} \left( \frac{1 - \sigma_c^2}{1 - \sigma_c^5} \right) \right] = \sigma_c^2, \quad (1)$$

where  $M$  is the mass of Mercury. The density contrast  $\eta_c = \rho_c/\rho_m$ , i.e. the ratio of the mean density of the core  $\rho_c$  to the mean density of the mantle and crust  $\rho_m$ , can be expressed by

$$\eta_c = \frac{1 - C_m/C}{C_m/C} \left( \frac{1}{\sigma_c^5} - 1 \right). \quad (2)$$

Given the recent estimate for the gravitational parameter of Mercury  $GM = 22031.870799 \pm 0.00086 \text{ km}^3/\text{s}^2$  ([Mazarico et al., 2014](#)) and the mean radius  $R = 2439.36 \pm 0.02 \text{ km}$  ([Perry et al., 2015](#)), the mean density of the planet is  $\bar{\rho} = 5425.2 \pm 6.7 \text{ kg/m}^3$ . The ratios of densities and radii for core and mantle must satisfy the relationship  $\bar{\rho} = \rho_m[1 + (\eta_c - 1)\sigma_c^3]$ , which allows the conversion of the ratios  $\eta_c$  and  $\sigma_c$  to absolute values  $\rho_m$ ,  $\rho_c$ , and  $R_c$ .

On the basis of this interior structure model one can conclude that the core-mantle boundary is at a radius of  $R_c = 2008 \pm 52 \text{ km}$ . The density of the core is  $\rho_c = 7214 \pm 488 \text{ kg/m}^3$ , and the density of the mantle and crust is  $\rho_m = 3175 \pm 245 \text{ kg/m}^3$ . A robust uncertainty estimate for these interior structure parameters can be obtained by examination of 1,000,000 Monte-Carlo simulations with values for  $C_m/C$ ,  $C/MR^2$ ,  $GM$ , and  $R$  consistent with their mean values, variances, and covariances. The one- and two-standard-deviation Bayesian confidence regions

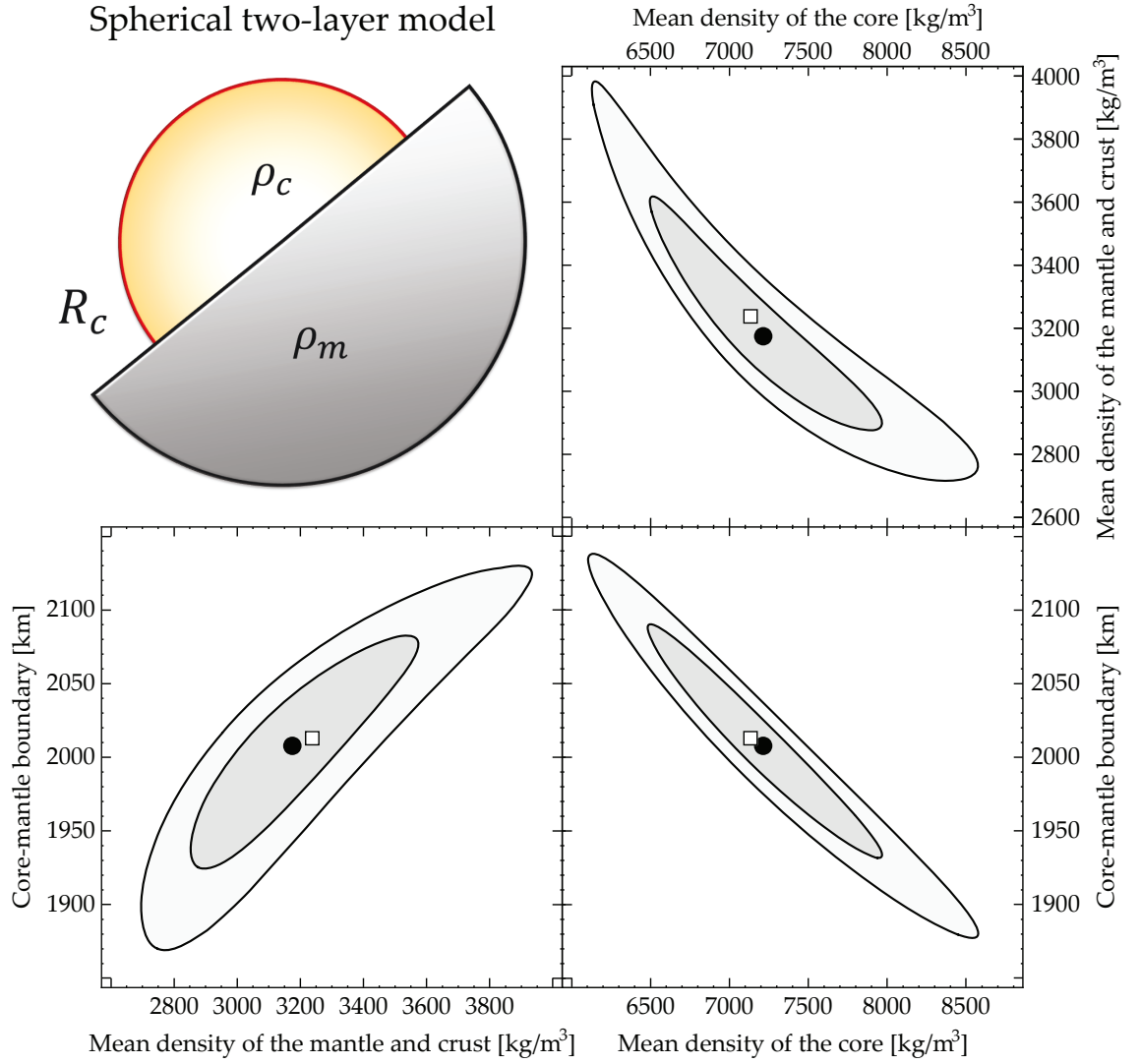


Figure 1: Interior structure parameters for a spherical two-layer model as derived from the observed rotational parameters (filled circle and one- and two-standard-deviation Bayesian confidence regions). The estimates of *Margot et al. (2012)* are denoted by a square.



(Figure 1) indicate high correlations among model parameters and delineate the parameter space.

More sophisticated models treat distinct crustal and mantle layers, the possibility of compositional layering in the mantle, the ellipticity of layer boundaries, and the effects of a possible solid inner core (*Smith et al., 2012; Hauck et al., 2013; Rivoldini and Van Hoolst, 2013; Peale et al., 2015*). Nonetheless, the values for the spherical two-layer model are in agreement with values for more complicated models (*Hauck et al., 2013; Rivoldini and Van Hoolst, 2013*), but have larger confidence regions.

Further research could discuss the reasons for the observation of the non-resonant rotation rate and the possible displacement of the rotation axis from the Cassini state. One possible explanation for the increased rotation rate with respect to the resonant rotation rate was discussed in Paper III and involves a long-period libration with a period of about 12 years. However, if other types of observations, e.g. of the magnetic field, would favor a large solid inner core, the coupling between mantle and inner core can also lead to variations of the rotation rate and explain the observed values.

## **6.5 Implications for cartography and base maps**

The rotation state of a planet is of fundamental importance for cartography and the preparation of base maps. The body-fixed reference frame is defined by the rotation state, consisting of the orientation of rotation axis, including precession and nutation effects, and the rotation about this axis. The latter includes the mean rotation rate and its oscillations, i.e. librations, and the prime meridian constant, which defines the orientation of the prime meridian at the reference epoch (see Appendix 2 of this thesis). Thus, with a correct description of the rotational state observations of Mercury can be correctly referenced. Images and topography information can be then compiled to a large map, which is suitable for geological studies and determination of coordinates for places of interest for further observations.

With the results obtained in Paper III the rotational parameters of Mercury can be updated and used for preparation of base maps. However, the impact on the location of features is on the sub-kilometer scale. For instance, the accumulated effect over four years of the difference between the measured rotation rate and the resonant rotation rate amounts to approximately 700 m. Likewise, the improvements in the orientation of the rotation axis and the libration amplitude are affecting locations on scales below 100 m. Nevertheless, these improvements are of great importance, as the imaging system on board MESSENGER obtained images up to a ground resolution of a few meters and the laser altimeter foot-

print had a diameter of less than 150 m. A cross-over analysis, which uses the differential height observation of two crossing laser profiles, would be strongly affected by such corrections, due to the displacement of the intersection point of the profiles.

## 6.6 Future exploration of Mercury: BepiColombo mission

The upcoming mission to Mercury BepiColombo will perform further investigations of the planet (*Benkhoff et al., 2010*). This joint-mission of the European Space Agency (ESA) and Japan Aerospace eXploration Agency (JAXA) includes two spacecraft, the Mercury Planetary Orbiter (MPO) and the Mercury Magnetospheric Orbiter (MMO). The MPO will revolve about Mercury on an elliptical orbit in surface distances between 480 and 1500 km. While the MMO will have an elongated elliptical orbit reaching distances up to 11,800 km. Likewise to the MESSENGER spacecraft the MPO will be equipped by an imaging system (Spectrometer and Imagers for MPO BepiColombo-Integrated Observatory System (SYMBIO-SYS), *Flamini et al., 2010*) and a laser altimeter (BepiColombo Laser Altimeter (BELA), *Thomas et al., 2007*).

Observations by BepiColombo could confirm the long-period librations and further constrain the size and the structure of Mercury's core. Data that will be obtained by the laser altimeter and imaging system can be analyzed by means of the method presented in the thesis (Paper II & III). A combined analysis of MESSENGER and BepiColombo data is also possible. The synergy of all data will finally allow a more complete description of Mercury's characteristics and that way contribute to a better understanding of its formation and evolution.

## References

- Araki, H., H. Noda, S. Tazawa, Y. Ishihara, S. Goossens, and S. Sasaki (2013), Lunar laser topography by LALT on board the KAGUYA lunar explorer - Operational history, new topographic data, peak height analysis of laser echo pulses, *Advances in Space Research*, 52(2), 262–271.
- Archinal, B. A., et al. (2011), Report of the IAU Working Group on Cartographic Coordinates and Rotational Elements: 2009, *Celestial Mechanics and Dynamical Astronomy*, 109(2), 101–135.
- Benkhoff, J., J. van Casteren, H. Hayakawa, M. Fujimoto, H. Laakso, M. Novara, P. Ferri, H. R. Middleton, and R. Ziethe (2010), Bepi-Colombo - Comprehensive exploration of Mercury: Mission overview and science goals, *Planetary and Space Science*, 58(1-2), 2–20.
- Davies, M. E., et al. (1980), Report of the IAU Working Group on Cartographic Coordinates and Rotational Elements of the Planets and Satellites, *Celestial mechanics*, 22(3), 205–230.
- Dufey, J., B. Noyelles, N. Rambaux, and A. Lemaître (2009), Latitudinal librations of Mercury with a fluid core, *Icarus*, 203(1), 1–12.
- Flamini, E., et al. (2010), SIMBIO-SYS: The spectrometer and imagers integrated observa-

- tory system for the BepiColombo planetary orbiter, *Planetary and Space Science*, 58(1-2), 125–143.
- Gläser, P., I. Haase, J. Oberst, and G. A. Neumann (2013), Co-registration of laser altimeter tracks with digital terrain models and applications in planetary science, *Planetary and Space Science*, 89(0), 111–117.
- Gwinner, K., et al. (2010), Topography of Mars from global mapping by HRSC high-resolution digital terrain models and orthoimages: Characteristics and performance, *Earth and Planetary Science Letters*, 294(3-4), 506–519.
- Gwinner, K., R. Jaumann, and the HRSC Co-Investigator Team Global Topography and Mosaic Generation Task Group Team (2015), MarsExpress High Resolution Stereo Camera (HRSC) Multi-orbit Data Products: Methodology, Mapping Concepts and Performance for the first Quadrangle (MC-11E), *EGU General Assembly Conference Abstracts*, EGU2015-13832-2.
- Hauck, S. A., II, et al. (2013), The curious case of Mercury's internal structure, *Journal of Geophysical Research: Planets*, 118(6), 1204–1220.
- Margot, J. L., S. J. Peale, R. F. Jurgens, M. A. Slade, and I. V. Holin (2007), Large longitude libration of Mercury reveals a molten core, *Science*, 316(5825), 710–714.
- Margot, J. L., et al. (2012), Mercury's moment of inertia from spin and gravity data, *Journal of Geophysical Research-Planets*, 117(E12), E00L09.
- Mazarico, E., A. Genova, S. Goossens, F. G. Lemoine, G. A. Neumann, M. T. Zuber, D. E. Smith, and S. C. Solomon (2014), The gravity field, orientation, and ephemeris of Mercury from MESSENGER observations after three years in orbit, *Journal of Geophysical Research-Planets*, 119(12), 2417–2436.
- Noyelles, B., and S. D'Hoedt (2012), Modeling the obliquity of Mercury, *Planetary and Space Science*, 60(1), 274–286.
- Peale, S. J., J.-L. Margot, S. A. Hauck, II, and S. C. Solomon (2015), Consequences of a solid inner core on Mercury's spin configuration, *Icarus*, 264, 443–455.
- Perry, M. E., et al. (2015), The low-degree shape of Mercury, *Geophysical Research Letters*, 42(17), 6951–6958.
- Ping, J. S., Q. Huang, J. G. Yan, J. F. Cao, G. S. Tang, and R. Shu (2009), Lunar topographic model CLTM-s01 from Chang'E-1 laser altimeter, *Science in China Series G: Physics, Mechanics and Astronomy*, 52(7), 1105–1114.
- Rivoldini, A., and T. Van Hoolst (2013), The interior structure of Mercury constrained by the low-degree gravity field and the rotation of Mercury, *Earth and Planetary Science Letters*, 377(0), 62–72.
- Scholten, F., J. Oberst, K. D. Matz, T. Roatsch, M. Wahlisch, E. J. Speyerer, and M. S. Robinson (2012), GLD100: The near-global lunar 100 m raster DTM from LROC WAC stereo image data, *Journal of Geophysical Research-Planets*, 117(E12), E00H17.
- Smith, D. E., et al. (2010), The Lunar Orbiter Laser Altimeter Investigation on the Lunar Reconnaissance Orbiter Mission, *Space Science Reviews*, 150(1-4), 209–241.
- Smith, D. E., et al. (2012), Gravity field and internal structure of Mercury from MESSENGER, *Science*, 336(6078), 214–217.
- Steinbrügge, G., A. Stark, H. Hussmann, F. Sohl, and J. Oberst (2015), Measuring tidal deformations by laser altimetry. A performance model for the Ganymede Laser Altimeter, *Planetary and Space Science*, 117, 184–191.
- Thomas, N., et al. (2007), The BepiColombo Laser Altimeter (BELA): Concept and baseline design, *Planetary and Space Science*, 55(10), 1398–1413.
- Van Hoolst, T., and C. Jacobs (2003), Mercury's tides and interior structure, *Journal of Geophysical Research: Planets*, 108(E11), 1–16.
- Yseboodt, M., J. L. Margot, and S. J. Peale (2010), Analytical model of the long-period forced longitude librations of Mercury, *Icarus*, 207(2), 536–544.

## 7 Synthesis

The goal of this thesis was to study the rotational state of the planet Mercury. In the first research paper the parameters of a resonant rotation model were derived from the most recent planetary ephemeris of the planet. These values form a reference for the actual rotational parameters of Mercury and are important for the interpretation of the measurements. Furthermore, the instantaneous Laplace plane of Mercury's orbit was determined and the location of possible Cassini states for Mercury was reassessed. An advantage of this work compared to values published in existing literature was the estimation of the uncertainty of the reference values. With the help of this uncertainty estimation the significance of deviations between measured and reference values could be evaluated. Therefore the results obtained in this paper formed the basis for the discussion in Paper III.

In the second research paper a method for the measurement of rotational parameters using image and laser altimeter data was developed. It is a generalization of the co-registration method and presents a novel approach in measurement of the rotation state of a celestial body. The method was evaluated with simulated data and a procedure for the estimation of the uncertainty of the rotational parameters was provided. The simulation included the computation of high-resolution topography for laser profiles, based on a low resolution stereo DTM and a power spectrum from actual laser profiles of Mercury. Uncertainties in spacecraft position and attitude were also simulated and their impact on the uncertainty of the rotational parameter measurement were assessed.

In the third research paper the method described in Paper II was applied to actual data from MESSENGER and measurements for the libration amplitude, the orientation of the rotation axis, and the mean rotation rate were provided. The implications of these measurements on the interior structure of Mercury were discussed. This included the computation of the polar moment of inertia and the difference of the equatorial moments of inertia values. The effects from a solid inner core were discussed, but not considered in the computation of the moments of inertia. A possible explanation for the increased rotation rate was provided and other mechanisms were briefly discussed.

The results obtained in this thesis had widened the understanding of the rotation and interior structure of Mercury. In particular first orbital observations of Mercury's libration were provided and previous Earth-based observations could be confirmed.

## Appendix 1 – Mercury’s libration model

The mathematical description of the longitudinal librations is given by the solution of the torque equation, which is a second-order differential equation in the orientation of Mercury

$$C_m \ddot{\theta} = T, \quad (1)$$

where  $T$  is the tidal torque,  $C$  is the polar moment of inertia of Mercury’s mantle, and  $\theta$  its orientation. In Eq. 1 the small obliquity of Mercury and variations in the orbital inclination were neglected (Peale *et al.*, 2009). The gravitational potential of Mercury in the gravitational field of the Sun up to second degree is given by

$$V = -\frac{GM_{\odot} M_M}{r} \left[ 1 + \frac{R^2}{r^2} \left( \frac{1}{2} J_2 + 3C_{22} \cos 2\psi \right) \right], \quad (2)$$

where  $GM_{\odot}$  is the gravitational parameter of the Sun,  $M_M$  is Mercury’s mass,  $R$  the mean radius of Mercury,  $r$  is the distance between Sun and Mercury, and  $\psi$  measures the orientation of the axis of minimum moment of inertia relative to the solar direction. The coefficients  $J_2$  and  $C_{22}$  are the second degree and order coefficients of the spherical harmonic expansion of Mercury’s gravity field. Consequently the tidal torque is given by

$$T = \frac{\partial V}{\partial \psi} = \frac{3}{2} \frac{GM_{\odot}}{r^3} (4C_{22} M_M R^2) \sin 2\phi. \quad (3)$$

The coefficient  $C_{22}$  represents the mass asymmetry in the equatorial plane of Mercury and is given by  $C_{22} = (B - A)/(4M_M R^2)$ , where  $A < B$  are the equatorial moment of inertia. The angle  $\phi$  is connected to the orbital motion and can be expressed as  $\phi = \theta - (f + \omega)$ , where  $f$  is the true anomaly and  $\omega$  is the argument of pericenter of Mercury’s orbit. The orientation of Mercury is a superposition of an uniform rotation and the librations

$$\theta(t) = \theta_0 + \theta_1 t + \psi_m(t), \quad (4)$$

where  $\theta_0$  is the prime meridian constant,  $\theta_1$  the mean rotation rate, and  $\psi_m$  the libration angle. Since Mercury is in a 3:2 resonance we can write  $\theta_1 = 3/2n_0 + \omega_1$ , where  $n_0$  is the mean motion and  $\omega_1$  the precession of the argument of pericenter. One can set the prime meridian constant  $\theta_0$  such that the subsolar point lies on Mercury’s long axis at the time of the perihelion passage, thus  $\theta_0 = 3/2n_0 t_0 + \omega_0$ . Consequently, one obtains  $\ddot{\theta} = \ddot{\psi}_m$  and

$$\sin 2\phi = \sin(2\psi_m + 3n_0(t + t_0) - 2(\omega - \omega_0 - \omega_1 t) - 2f). \quad (5)$$

Neglecting small oscillations of the argument of pericenter  $\omega - \omega_0 - \omega_1 t \approx 0$  and assuming that  $\psi_m \ll 1$  leads to

$$\sin 2\phi \approx \sin(3n_0(t + t_0) - 2f) = \sin(3M - 2f). \quad (6)$$

With the semi-major axis  $a_0 = (GM_{\odot}/n_0^2)^{1/3}$  and the expression for  $C_{22}$  the tidal torque in Eq. 3 is now given by

$$T = \frac{3}{2} n_0^2 (B - A) \left( \frac{a_0}{r} \right)^3 \sin(3n_0(t + t_0) - 2f). \quad (7)$$

In order to obtain an analytical solution the last two terms  $(a_0/r)^3 \sin(3n_0(t + t_0) - 2f)$  can be expanded in a series in the eccentricity  $e$ . Subsequent averaging over one orbit results in

$$\langle T \rangle = \frac{3}{2} n_0^2 (B - A) \sum_{k=1}^{\infty} G_{(201)}(k, e) \sin(kn_0(t + t_0)) \quad (8)$$

where  $G_{(201)}(k, e) = [G_{(201-k)}(e) - G_{(201+k)}(e)]/k^2$  is the difference between two Kaula's eccentricity functions ([Kaula, 2000](#)) and  $\langle T \rangle$  denote the averaging over one orbit.

Now the solution to equation 1 is straightforward and reads

$$\psi_m = \frac{3}{2} \frac{B - A}{C_m} \sum_{k=1}^{\infty} G_{(201)}(k, e) \sin(kn_0(t + t_0)) \quad (9)$$

and the libration amplitude is given by

$$g_{88/k} = \frac{3}{2} \frac{B - A}{C_m} G_{(201)}(k, e). \quad (10)$$

## Appendix 2 – Prime meridian constant of Mercury

The prime meridian of Mercury is defined by the impact crater Hun Kal (twenty in the Mayan mathematical system). The angle between the prime meridian and the intersection point of the planet's equator and the equator of the International Celestial Reference Frame (ICRF) at J2000.0 is the prime meridian constant,  $W_0$ . The value of  $W_0$  should ensure that the center of the crater Hun Kal is at planetographic longitude  $20^\circ$  W or planetocentric longitude  $340^\circ$  E.

An early value of  $W_0$  was calculated by [Davies et al. \(1980\)](#) from a control point network derived from Mariner 10 images. A value of  $W_0 = 329.71^\circ$  ( $184.74^\circ$  with respect to the equinox B1950, epoch J1950) was adopted by the International Astronomical Union Working Group on Cartographic Coordinates and Rotational Elements of the Planets and Satellites (IAU WGCCRE). The value was refined by [Davies et al. \(1995\)](#) to  $W_0 = 329.69^\circ$  on the basis of a new control network computation that included a determination of the focal lengths of the Mariner 10 cameras. More recently the prime meridian was further refined by an improved control net to  $W_0 = 329.548^\circ$  ([Robinson et al., 1999](#)). In 2007, longitudinal librations of Mercury were observed ([Margot et al., 2007](#)) and led to a redefinition of the  $W_0$

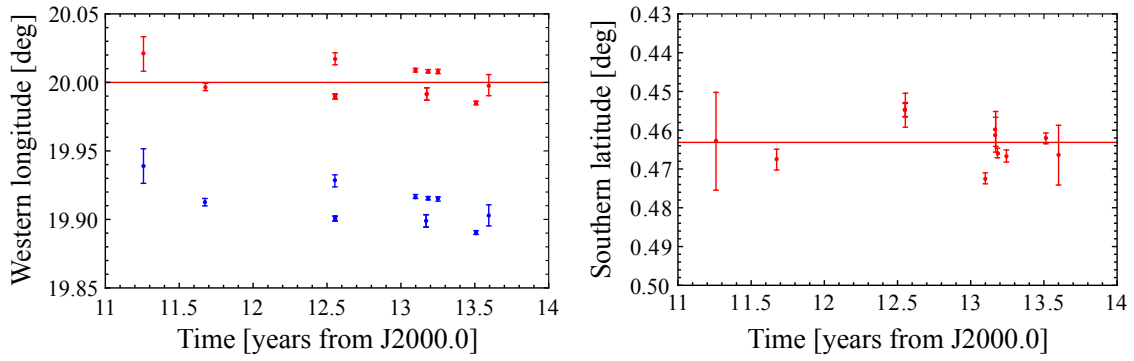


Figure 1: Measured longitude (left) and latitude (right) of the center of the crater Hun Kal in 12 MDIS images acquired from orbit about Mercury. The longitudes obtained with the current IAU rotation model ([Archinal et al., 2011](#)) are depicted in blue, and the adjusted longitudes (with the rotation rate of Paper III and updated  $W_0$  value) are shown in red.

value, as the libration angle is not 0.0 at J2000.0. The new value  $W_0 = 329.5469^\circ$  was adopted by the IAU in 2011 ([Archinal et al., 2011](#)).

Observations by the MESSENGER spacecraft during orbital operations suggest a rotation rate of Mercury somewhat higher than the resonant value ([Mazarico et al., 2014](#), Paper III), a situation that demands a correction to the prime meridian value. The resonant mean spin rate of Mercury obtained in Paper I differs from the value often quoted as the resonant mean spin rate and adopted for Mercury by the IAU since 1980. The spin rates derived from MESSENGER data ([Mazarico et al., 2014](#), Paper III) are significantly different from both the current IAU spin rate and the resonant spin rate.

Given the latest value for the spin rate, a new value for  $W_0$  is required. Such a new value in turn requires observations of the location of Hun Kal with respect to the inertial frame, i.e., the ICRF. Topography measurements have been acquired by the Mercury Laser Altimeter (MLA) and the Mercury Dual Imaging System (MDIS). As of 2014, MDIS had acquired about 12 images as resolutions less than 1 km in which the crater Hun Kal is identifiable. However, errors in the attitude of the imaging system as well as the calibration of the imaging system result in uncertainties in the coordinates of the image pixels when projected onto the spherical grid of Mercury (orthorectification). The nearest MLA observation (data up to April 2014) to Hun Kal is located at  $0.455^\circ$  S,  $338.536^\circ$  E, i.e., more than 60 km from the crater. Since no MLA profiles cross Hun Kal, an update to the  $W_0$  value is not easily obtained from MLA data alone.

MDIS images available up to April 2014 that include Hun Kal were orthorectified using the rotation rate of  $W_1 = 6.1385025^\circ/\text{day}$  ([Archinal et al., 2011](#)). The location of the center of Hun Kal was then determined visually by reading the co-



Table 1: List of MDIS images used for measurement of the prime meridian value  $W_0$ .

1 EN1005053163M	5 EN0223616660M	9 EN1004678277M
2 EN1002521325M	6 EN0251340756M	10 EN1018134317M
3 EN1015451668M	7 EN0251369558M	11 EN0251369585M
4 EN1007130467M	8 EN1004678315M	12 EN0210498522M

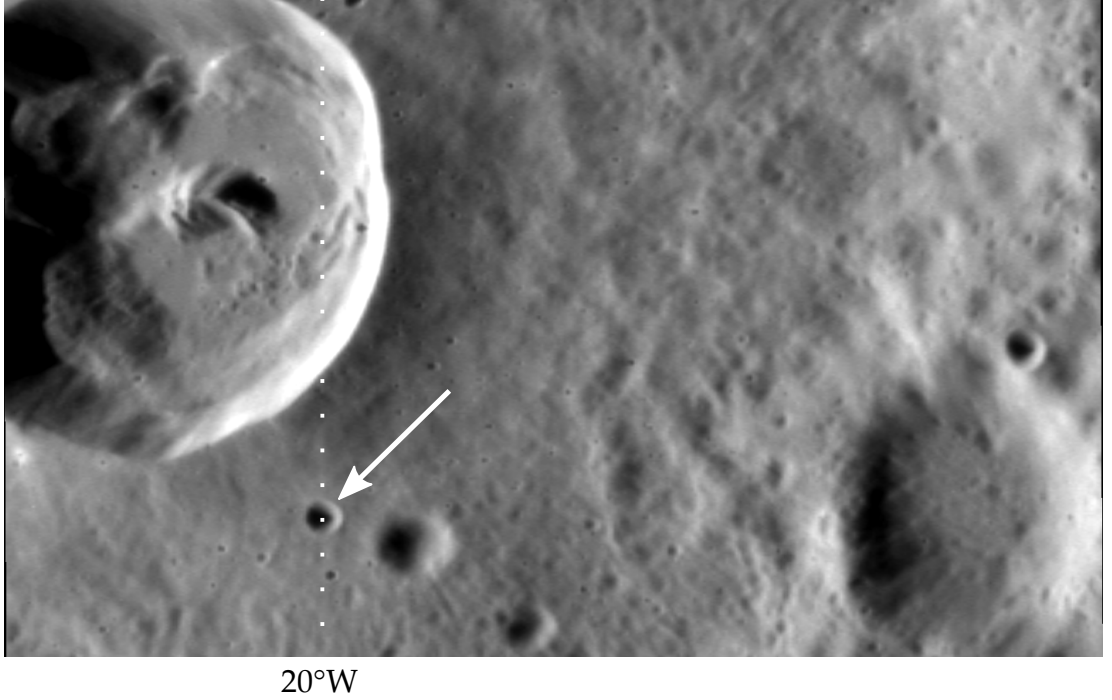


Figure 2: MDIS image showing Hun Kal (indicated by an arrow). The ground resolution of this NAC image is 73 m (EN1007130467M).

ordinates of a crosshair. From the image resolution and the visibility conditions of the crater, a positioning error was assigned. Figure 1 shows the coordinates of Hun Kal so obtained. With the IAU rotational model ([Archinal et al., 2011](#)) the crater was found to be offset by approximately  $0.09^\circ$  (3.9 km) from  $-20^\circ$  E. The latitude of Hun Kal was found to be at  $0.4631^\circ$  S. Least-squares fits to the data with updated rotation rates yield the following values for  $W_0$  with an uncertainty of  $0.0037^\circ$ .

Retaining the IAU rotation rate of  $W_1 = 6.1385025^\circ/\text{day}$  ([Archinal et al., 2011](#)) leads to an updated value of  $W_0 = 329.6369^\circ$ . When the rotation rate  $W_1 = (6.13851804 \pm 0.00000094)^\circ/\text{day}$  (Paper III) is adopted, the value for  $W_0$  should be  $329.5648^\circ$ . For the resonant rotation rate  $W_1 = 6.1385068^\circ/\text{day}$  (Paper I) and with the introduction of additional long-period librations, the prime meridian



constant is  $W_0 = 329.6268^\circ$  and long-period librations must be included in the rotation model (see supplementary online material of Paper III). [Mazarico et al. \(2014\)](#) calculated a rotation period of  $58.646146 \pm 0.000011$  days, which is equivalent to a rotation rate of  $(6.13851079 \pm 0.0000012)^\circ/\text{day}$ . The corresponding  $W_0$  value should be then  $W_0 = 329.5988^\circ$ .

## References

- Archinal, B. A., et al. (2011), Report of the IAU Working Group on Cartographic Coordinates and Rotational Elements: 2009, *Celestial Mechanics and Dynamical Astronomy*, 109(2), 101–135.
- Davies, M. E., et al. (1980), Report of the IAU Working Group on Cartographic Coordinates and Rotational Elements of the Planets and Satellites, *Celestial mechanics*, 22(3), 205–230.
- Davies, M. E., et al. (1995), Report of the IAU/IAG/COSPAR Working Group on Cartographic Coordinates and Rotational Elements of the Planets and Satellites: 1994, *Celestial Mechanics and Dynamical Astronomy*, 63(2), 127–148.
- Kaula, W. M. (2000), *Theory of Satellite Geodesy: Applications of Satellites to Geodesy*, 36–38 pp., Dover, Mineola, N.Y., 160 p.
- Margot, J. L., S. J. Peale, R. F. Jurgens, M. A. Slade, and I. V. Holin (2007), Large longitude libration of Mercury reveals a molten core, *Science*, 316(5825), 710–714.
- Mazarico, E., A. Genova, S. Goossens, F. G. Lemoine, G. A. Neumann, M. T. Zuber, D. E. Smith, and S. C. Solomon (2014), The gravity field, orientation, and ephemeris of Mercury from MESSENGER observations after three years in orbit, *Journal of Geophysical Research-Planets*, 119(12), 2417–2436.
- Peale, S. J., J. L. Margot, and M. Yseboodt (2009), Resonant forcing of Mercury’s libration in longitude, *Icarus*, 199(1), 1–8.
- Robinson, M. S., M. E. Davies, T. R. Colvin, and K. Edwards (1999), A revised control network for Mercury, *Journal of Geophysical Research: Planets*, 104(E12), 30,847–30,852.

# Eidesstattliche Erklärung

Ich erkläre an Eides Statt, dass ich meine Doktorarbeit mit dem Titel

**„Observations of Mercury’s rotational state from combined MESSENGER laser altimeter and image data“**

selbständig und ohne Benutzung anderer als der angegebenen Hilfsmittel angefertigt habe und dass ich alle Stellen, die ich wörtlich oder sinngemäß aus Veröffentlichungen entnommen habe, als solche kenntlich gemacht habe. Die Darstellungen zum Eigenanteils der drei Veröffentlichungen sind zutreffend. Die Arbeit hat bisher in gleicher oder ähnlicher Form oder auszugsweise noch keiner Prüfungsbehörde vorgelegen.

Berlin, den 12. Oktober 2015

---

Alexander Stark